AD-A278 155

The Pennsylvania State University
APPLIED RESEARCH LABORATORY
P.O. Box 30
State College, PA 16804

STATISTICAL CHARACTERISTICS OF BISTATIC
SURFACE SCATTER AND MEAN BISTATIC SURFACE
SCATTERING STRENGTHS

by

P. D. Neumann
R. L. Culver

DTIC
ELECTE
APR 1 3 1994
S G D

Technical Report No. TR 94-07
March 1994

94-11245

DTIC QUALITY INSPECTED 3

94 4 12 167

REPORT DOCUMENTATION PAGE

OMB No. 0704-0188

Public reporting burden for this collection of information is estimated to average 1 hour per response, including the time for reviewing instructions, searching existing data sources, gathering and maintaining the data needed, and completing and reviewing the collection of information. Send comments regarding this burden estimate or any other aspect of this collection of information, including suggestions for reducing this burden, to Washington Headquarters Services, Directorate for Information Operations and Reports, 1215 Jefferson Davis Highway, Suite 1204, Arlington, VA 22202-4302, and to the Office of Management and Budget, Paperwork Reduction Project (0704-0188), Washington, DC 20503.

1. AGENCY USE ONLY (Leave blank)	2. REPORT DATE	3. REPORT TYPE AND DATES COVERED
	March 1994	

4. TITLE AND SUBTITLE

Statistical Characteristics of Bistatic Surface Scatter and Mean Bistatic Surface Scattering Strengths

5. FUNDING NUMBERS

N00039-92-C-0100

6. AUTHOR(S)

P. D. Neumann , R. L. Culver

7. PERFORMING ORGANIZATION NAME(S) AND ADDRESS(ES)

Office of Naval Research
800 North Quincy Street
Arlington, VA 22217

8. PERFORMING ORGANIZATION REPORT NUMBER

TR#-94-07

9. SPONSORING / MONITORING AGENCY NAME(S) AND ADDRESS(ES)

Applied Research Laboratory
The Pennsylvania State University
P.O. Box 30
State College, PA 16804

10. SPONSORING / MONITORING AGENCY REPORT NUMBER

11. SUPPLEMENTARY NOTES

12a. DISTRIBUTION / AVAILABILITY STATEMENT

Unlimited

12b. DISTRIBUTION CODE

13. ABSTRACT (Maximum 200 words)

The characterization of reverberation, from the surface, the bottom, and/or the volume, is important in advancing the understanding of the mechanisms involved in underwater sound scattering. Numerous experiments and much theoretical work have been done in the area of monostatic reverberation, but the area of bistatic reverberation has been much less researched. This certainly is a result of the much more complex geometries involved in bistatic reverberation.

This dissertation studied the statistics of bistatic surface reverberation data from the FLIP experiment conducted in January of 1992. The data were verified as homogeneous and normally distributed using the Kolmogorov-Smirnov two-sample test with a confidence interval, α, equal to 0.1. using a technique by which ensembles from different times were combined, meaningful deviations from a normal distribution were observed at the highest wind speed of 7.2 m/s.

14. SUBJECT TERMS

bistatic, surface, scatter, surface strength, reverberation, Kolmogorov-Smirnov

15. NUMBER OF PAGES

127

16. PRICE CODE

17. SECURITY CLASSIFICATION OF REPORT	18. SECURITY CLASSIFICATION OF THIS PAGE	19. SECURITY CLASSIFICATION OF ABSTRACT	20. LIMITATION OF ABSTRACT
UNCLASSIFIED	UNCLASSIFIED	UNCLASSIFIED	UNLIMITED

NSN 7540-01-280-5500

Standard Form 298 (Rev. 2-89)
Prescribed by ANSI Std. 239-18
298-102

Abstract

The characterization of reverberation, from the surface, the bottom, and/or the volume, is important in advancing the understanding of the mechanisms involved in underwater sound scattering. Numerous experiments and much theoretical work have been done in the area of monostatic reverberation, but the area of bistatic reverberation has been much less researched. This certainly is a result of the much more complex geometries involved in bistatic reverberation.

This dissertation studied the statistics of bistatic surface reverberation data from the FLIP experiment conducted in January of 1992. The data were verified as homogeneous and normally distributed using the Kolmogorov-Smirnov two-sample test with a confidence interval, α, equal to 0.1. Using a technique by which ensembles from different times were combined, meaningful deviations from a normal distribution were observed at the highest wind speed of 7.2 m/s.

The bistatic surface scattering strengths were calculated from the data and compared with the predictions of a theory developed by S.T. McDaniel for the prediction of bistatic surface scattering strengths. The comparison showed good agreement with a rms deviation of about 3 dB.

Table of Contents

List of Figures

List of Tables

Chapter 1

Introduction

1.1 Motivation

The characterization of underwater reverberation, from the surface, the bottom, and/or the volume, is important in advancing the understanding of the mechanisms involved in underwater sound scattering. Numerous experiments have been conducted to understand the effects of the environment, e.g., wind speed, wave height, grazing angle and bottom roughness, on reverberation. Theoretical predictions or models for reverberation have been developed, some based entirely upon theoretical work and some using empirical methods. This thesis establishes the characteristics of bistatic ocean surface reverberation as a function of wind speed and compares the mean bistatic surface scattering strengths to one predictive model.

Reverberation may be classified according to its source: surface, bottom, volume, or some combination. In addition, reverberation may be classified as either monostatic (source and receiver collocated) or bistatic (source and receiver at different locations). To date, boundary reverberation research has focused on monostatic geometries with few exceptions [1, 2, 3]. The data analysis in this thesis focuses on the statistical characteristics and mean scattering strengths of bistatic

surface scatter as a function of geometry and wind speed.

From a geometric standpoint, monostatic boundary scattering strength is a function of one parameter, the grazing angle, denoted by ψ_{inc}. It may also be a function of wind direction as suggested by Zornig [1]. Bistatic boundary reverberation also depends upon the bistatic angle, denoted by ϕ, and the scattered grazing angle, denoted by ψ_{scat}. There are, of course, additional parameters necessary to describe dependence upon the environment. The additional geometrical parameters present some challenges in displaying mean bistatic scattering strength, as discussed in Section 5.4.

Characterizing reverberation usually means describing the mean scattering strength, S, as a function of the geometrical and environmental parameters. A more complete characterization is contained in the cumulative distribution function, *cdf*, or probability density function, *pdf*, of S. The mean and the variance can be calculated from the distribution, and more importantly, comparison with theoretical distributions can be made. The statistical analysis of the bistatic surface scatter data implemented in this thesis used the *cdf* or the probability of false alarm, P_{FA}, which is defined as one minus the *cdf* in the analysis of reverberation data.

This thesis presents an analysis of the statistical characteristics of bistatic surface scattering strength from ocean surface scatter data taken in January of 1992. The experiment was conducted by the Applied Physics Laboratory at the University

of Washington (APL-UW) using the RV FLIP, FLoating Instrument Platform. The main purpose of the experiment was to investigate the relationship between the ocean sub-surface bubble layer and surface forward scatter and backscatter. Forward and backscatter data were taken between 10 and 80 KHz. Out of plane scatter was also investigated over the range of frequencies, of which data at 30 and 40 KHz could be analyzed for bistatic scattering strength.

1.2 Original Contributions

The quality and uniqueness of the data produced a number of new results. The original contributions presented in this thesis are as follows. These contributions are discussed in more detail in Chapters 4, 5 and 6.

- The ocean surface scatter data were histogrammed and their cumulative distribution function compared with a Rayleigh distribution using the probability of false alarm, P_{FA}. Theory predicts that the dominant surface scattering mechanism is the slope of surface for higher grazing angles and isotropic resonant bubble scatter at lower grazing angles and higher wind speeds. The magnitude of the complex envelope of the ocean surface scatter data was found to be Rayleigh for both mechanisms and for all but the highest wind speed (7.2 m/s). This result shows that the use of the central limit theorem to describe the statistical characteristics of bistatic surface scatter is valid over the geometries and wind speeds, except 7.2 m/s, studied here. It also shows that the central limit theorem is valid for both scattering mechanisms, surface rough-

ness and the bubble layer, for the geometries and all but the highest wind speed studied here.

- Mean bistatic surface scattering strength was calculated using the sonar equation and compared to a prediction by S.T. McDaniel's theory for bistatic surface scattering strengths [15]. The portion of the theory for predicting scattering strengths dominated by bubble scattering was validated by the data for a number of geometries. This is the first validation of that portion of the theory.

- A technique was developed for combining ocean surface scatter data for different grazing angles which increased the number of data points in the ensemble. With this technique, data which were the result of the same dominant scattering mechanism, the surface itself or the sub-surface bubble layer, were combined to estimate the statistical characteristics of the scattering mechanism.

1.3   Thesis Outline

This thesis is organized as follows. Chapter 2 presents a literature review of the experimental work with regard to both monostatic and bistatic surface reverberation. Chapter 3 provides an overview of the FLIP experiment and describes the process by which the data were validated as homogeneous. Chapter 4 describes the process by which the data were tested for Rayleigh behavior. The results showed the bistatic surface scatter to be Rayleigh except at the highest wind speed of 7.2 m/s. Chapter 5 details the calculation of the bistatic surface scattering strength,

$SS(\psi_{inc}, \psi_{scat}, \phi)$, from the data using the sonar equation for bistatic surface reverberation. Chapter 6 presents an overview of S.T. McDaniel's bistatic surface scattering strength theory and shows a comparison between the theory and the data. The comparison showed good agreement with an rms deviation of about 3 dB. Chapter 7 presents recommendations for future research in this area. The original contributions of this thesis are presented in Chapters 4, 5 and 6.

Chapter 2

Historical Background of Boundary Reverberation

2.1 Experimental Work in Monostatic Reverberation

A number of papers from the middle 1950's to the early 1970's provided a great deal of the knowledge about surface reverberation. In general, they characterized surface scattering strength as a function of one or more measured environmental variables, such as wind speed or wave height. Results were presented as either a set of curves or an equation. However, variations of 5 to 10 dB between different researcher's results were common. Nevertheless, the data collected by these researchers is still valuable in identifying trends and general characteristics in monostatic surface reverberation.

2.1.1 Urick & Hoover: 1956

An experiment carried out by Urick and Hoover in 1955 [4] measured monostatic surface reverberation for grazing angles between 5° and 90°, wind speeds between 3 and 18 knots and a transmit frequency of 60 KHz. The procedure for extracting results from the data was to calculate the average scattering strength from individual pings with the same wind speed and grazing angle. A set of curves were then generated from the data, with each curve corresponding to a particular

wind speed, and plotted with the grazing angle as the independent variable and the scattering strength as the dependent variable. The general trends shown in the data were:

- at low grazing angles, scattering strength increases with wind speed,

- at low grazing angles and higher wind speeds, scattering strength becomes less dependent upon grazing angle,

- at grazing angles near normal incidence, scattering strength decreases with increasing wind speed.

These trends are seen in Figure 2.1, which shows monostatic surface scattering strength as a function of grazing angle and wind speed. Figure 2.1 was generated using the model developed by S.T. McDaniel [15]. More information on this model is included in Chapter 6.

In addition, Urick and Hoover put forward several hypotheses about the mechanisms involved in sea surface scattering. At low grazing angles, the authors suggested that a sub-surface bubble layer rather than sea surface roughness is the dominant source of scattering. That the scattering strengths were roughly independent of grazing angle is consistent with isotropic scatterer by a bubble layer.

At grazing angles near normal incidence, the dominant echanism was specular reflection from the sea surface. They theorized that the sea surface is made up of numerous facets whose orientation and distribution are dependent upon
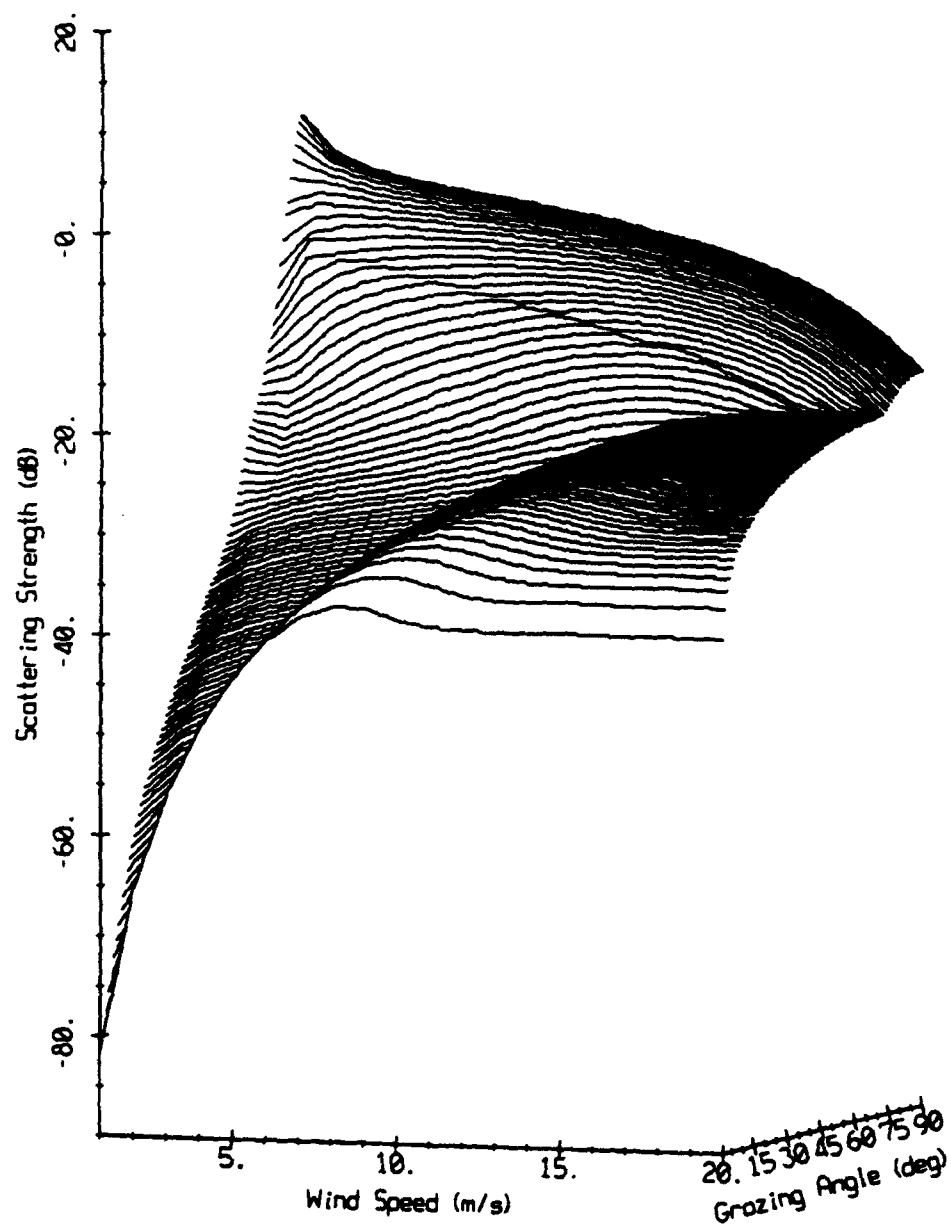
Figure 2.1: Monostatic Surface Scattering Strength -vs- Wind Speed and Grazing Angle.

wind speed. At very low wind speeds, the sea surface is mirror-like, causing high scattering strengths near normal incidence and low scattering strengths away from normal incidence. At higher wind speeds, the sea surface is disturbed and has many facets which scatter energy over a larger solid angle. The result is lower scattering strengths near normal incidence and higher scattering strengths away from normal incidence.

The major contribution of the work by Urick and Hoover was the suggestion that the dominant mechanism in surface backscatter depends upon the grazing angle in the following way:

- at low grazing angles, scattering is dominated by a sub-surface scattering layer,

- at intermediate grazing angles, scattering is dominated by rough-surface scattering,

- at high grazing angles, scattering is dominated by specular reflection.

With the postulation that these three mechanisms were dominant at different grazing angles, other experiments sought to confirm these results.

2.1.2 Garrison, Murphy & Potter: 1960

This paper utilized measurements taken by APL-UW at a transmit frequency of 60 KHz in Dabob Bay during 1956 and 1957 [5] to study the relationship between surface reverberation and measured environmental parameters. During the experiment, both wind speed and wave height were recorded in an effort to

discover which of the two was better correlated with reverberation levels. An in-teresting note about Dabob Bay is that the fetch from the southwest is roughly 10 times the length of the fetch from the north. This results in dramatically different waveheights for the same wind speed, depending upon the wind direction, and was particularly useful in isolating the effects of wind speed and wave height.

Transducers with circularly symmetric beam patterns were deployed with the axis of symmetry pointed perpendicular to the surface. With this arrangement, the transmitted pulse would reach the surface and spread out in an annular ring. Therefore, the reverberation return at any time has a corresponding grazing angle that can be calculated from the depth of the transducer and the time after trans-mission of the pulse. The procedure in the experiment was to transmit pulses at an interval long enough to allow the reverberation from the previous pulse to decrease to at or below the background noise level. The reverberation return was recorded at a fixed time after the pulse was transmitted, corresponding to the grazing angle of interest. At the same time, information on the surface conditions were recorded. The results of the experiment showed that surface scattering strength had greater correlation with wind speed than wave height at a grazing angle of 7°. The surface scattering strengths were more tightly grouped together at a particular wind speed than at a particular wave height.

Paralleling the work done by Urick and Hoover [4], a set of curves were generated, each corresponding to a particular wind speed, with the grazing angle

as the independent variable and the surface scattering strength as the dependent variable. The set of curves from the APL-UW data agree with the curves from Urick and Hoover except at low grazing angles. The APL-UW curves show the surface scattering strength falling off at grazing angles below 20° while the Urick and Hoover's curves show the surface scattering strength remaining constant below roughly 35°. This difference in results may be a consequence of the APL-UW data being screened to omit points which appeared to be contaminated by volume reverberation, most likely sub-surface bubble scatter, which were included in the Urick and Hoover results.

2.1.3 Plemmons, Shooter & Middleton: 1972

The work done by Plemmons, Shooter, and Middleton [7] at the Applied Research Laboratory, University of Texas, (ARL-UT) presents a statistical analysis of fresh water lake surface reverberation. This summary of their work focuses on the method by which they tested the surface reverberation data for homogeneity.

In all the data sets collected, 150 pulses were transmitted at the operating frequency of 110 KHz with an interval between the pulses long enough for the reverberation level to decay to at or below the background level. All of the data for a particular pulse length and type were collected over a short period of time.

Quadrature components of the reverberation signal were grouped together in ensembles, each corresponding to the same time after the transmission of the signal. Each ensemble contained 150 values from a distinct pulse type and delay

after transmit. With these ensembles, estimates of certain characteristics of the reverberation were calculated, such as the mean value of the amplitude at a particular time t_1

$$\langle x(t_1) \rangle_{ensemble\ average} = \frac{1}{N} \sum_{i=1}^{N} x_i(t_1). \tag{2.1}$$

Before such estimates of statistical quantities were made, the ensembles were validated. Validating an ensemble entails showing that the ensemble comes from a statistically proper parent distribution. This involves testing the ensemble for homogeneity.

The ensembles were tested for homogeneity using the Kolmogorov-Smirnov (K-S) two-sample test, described in detail by Siegel [9], which determines whether two independent ensembles have the same parent distribution. The rationale for this test is that if two ensembles, usually the first and second half of a large ensemble, come from the same parent distribution, then both will have the same cumulative distribution function. The procedure is to calculate the cumulative distribution functions, *cdf's*, for each ensemble and find the greatest deviation between the them. This maximum deviation is called Z_{sample} and is compared with Z_{α}, which is determined from the confidence level, α, and from the number of samples in the ensembles. If $Z_{sample} \leq Z_{\alpha}$, the two ensembles are taken to be from the same parent distribution. If $Z_{sample} > Z_{\alpha}$, the ensembles are from different parent distributions. However, in using this test, the results of the comparison of Z_{sample} with Z_{α} are incorrect $\alpha \times 100\%$ of the time. This becomes important when

large numbers of ensembles are tested, because some ensembles will fail the test for homogeneity even when the ensembles are homogeneous.

This paper presented a systematic method for checking the validity of data so that results derived from the data could also be considered valid. This is a key step forward from earlier experiments which used time averages over part of a single return or averages over multiple returns without testing the validity of the data. This type of analysis is used on the FLIP data in Section 3.6.

2.1.4   Frazer: 1978

The paper by Marshall Frazer [8], also from ARL-UT, investigated the statistical properties of surface reverberation from a lake surface. The surface reverberation data were first tested for statistical validity and then tested for normality.

The experiment utilized a transducer located at a depth of 3.7 meters with the axis of the main lobe intersecting the surface at a grazing angle of 9°. The wind speed was approximately 6.0 m/s with a fetch of 2.4 km. A 100-μsec, 80 KHz CW pulse was used resulting in an scattering patch area of less than 1 square meter. This value is important because the assumption of Gaussian characteristics in surface reverberation are based upon a large number of independently placed scatterers. If the reverberation is still Gaussian with such a small surface area being ensonified, applications in which a much larger surface area is ensonified should also be Gaussian.

The statistical validity of the data was checked using the one-sample runs

test and the K-S two-sample test as done by Plemmons, et al.[7]. With the statistical validity of the sample ensembles established, the data were tested for normality using the K-S one-sample test. The mean of the ensemble, $\hat{\mu}(t)$, was calculated using an ensemble average, which is an average over all the measurements at a particular instant in time, t, after the pulse transmission. The variance, $\hat{\sigma}^2(t)$, was calculated in a similar manner. The mathematical expressions for calculating the ensemble mean and variance are

$$\hat{\mu}(t) = \frac{1}{N}\sum_{i=1}^{N} x_i(t) \tag{2.2}$$

and

$$\hat{\sigma}^2(t) = \frac{1}{N-1}\sum_{i=1}^{N}[x_i(t) - \hat{\mu}(t)]^2 . \tag{2.3}$$

With values for $\hat{\mu}(t)$ and $\hat{\sigma}^2(t)$, a theoretical Gaussian (normal) cumulative distribution can be calculated using the usual expression for Gaussian *cdf's* with the ensemble mean and variance introduced

$$\hat{F}_{theoretical}(x(t), V) = \frac{1}{\sqrt{2\pi\hat{\sigma}^2(t)}} \int_{-\infty}^{V} \exp[-(x - \hat{\mu}(t))^2/2\hat{\sigma}^2(t)]dx. \tag{2.4}$$

This theoretical *cdf* is then compared with the *cdf* calculated from the ensemble, and the greatest deviation between the two is the sample test statistic, $Z_{sample}(t)$. The threshold value, Z_α, is determined in the same way as for the K-S two-sample test. If $Z_{sample}(t) > Z_\alpha$, the ensemble fails the test and is determined to be non-

Gaussian at the significance level α. Also, $\alpha \times 100\%$ of the tests should fail even if all of the ensembles are Gaussian, so judgement is called for in analyzing the results of the test.

The results of the experiment indicated that the surface reverberation was Gaussian for the $\alpha = 0.05$ level of significance. However, it should be noted that some data that contained both surface and bottom returns were not Gaussian. This means that additional work is needed to determine the environment in which reverberation is Gaussian and more importantly, the environment in which the reverberation is not Gaussian. This method for testing data for normality was used on the FLIP data in Section 4.2.

2.2 Experimental Work in Bistatic Reverberation

Little work has been done in bistatic scattering from the sea surface, and the work that has been done covers a wide range of frequencies. Experimental work in bistatic surface scattering began in the early 1970's and has continued to date, but unlike the work in monostatic surface, scattering the mechanisms responsible in bistatic surface scattering are less understood and the data are sparse.

2.2.1 Zornig: 1978

The experimental work done by Zornig [1] represents a systematic study of bistatic surface scatter. Working in a tank, the wind conditions over the surface were accurately controlled and repeatable so stationary surface conditions could be

maintained during measurements. Operating at very short wavelengths, about 1 mm, the Kirchhoff approximation, which is the basis of much analytical work, could be used. With such a controlled environment, the effects of a single parameter such as wind direction could be determined. However, the results of this experiment may be unique to the very high frequency, 1.3 MHz, and controlled surface conditions.

The measurements showed scattering strength to be strongly dependent on wind direction. Scattering strength was found to be much higher in the upwind direction than in either the downwind or crosswind case. Other conclusions from the results were that scattering strength was not strongly dependent on either ψ_{inc} or ψ_{scat} between 12° and 17°. This agrees with past experiments which showed scattering strength to be independent of grazing angle in the same range of values. Varying the acoustic wavelength by changing the operating frequency from 1.3 MHz to 1.1 MHz produced little change in the scattering strength, but variations in surface roughness produced large changes in the scattering strength.

Zornig hypothesized that bistatic surface scattering strength cannot be characterized by a simple parameter such as the Rayleigh roughness parameter, but may be a function of such descriptors as rms slope of the surface, probability density of slopes, or two-dimensional correlation of the surface. The work done by Zornig was a valuable step in characterizing the parameters that describe bistatic surface reverberation.

2.2.2 Culver & McDaniel: 1991

The work done by Culver and McDaniel [3] incorporated the capability to predict time-varying reverberation spectra into the Generic Sonar Model (GSM) and compared the predictions with bistatic measurements. The new routine utilizes the McDaniel theory [15] to compute surface scattering strength and keeps track of Doppler shifts due to motion of the source, receiver, and scatterers. The McDaniel theory is described in Chapter 6. Briefly, it uses the Kirchhoff approximation near specular and the Rayleigh-Rice approximation away from specular. Also, a sub-surface bubble layer incorporated into the model provides a noticeable effect at low grazing angles and when the number of bubbles per unit volume is large. The effect of the bubble layer is to put a minimum value on the surface scattering strength away from the specular direction since scattering from a bubble layer is isotropic.

The bistatic data used for comparison were taken in Puget Sound with a transmit frequency range of 10 to 30 KHz and a pulse length of 0.3 msec. The results showed multi-ping averages in a 2.8 KHz band around the transmit frequency. Overlaid on the experimental results were the predictions from GSM. The results showed good agreement in the portion of the return dominated by the main lobe, but are up to 30 dB below the measured values in the portions of the return dominated by sidelobes. A possible cause given for this disagreement is that the transmit center frequency beam pattern was used for the simulation, yet over the bandwidth of the pulse, the beam pattern may vary considerably. Aside from this

disagreement, the results show that the surface return is composed of two distinct regions. The first region is dominated by coherent reflection, and is well modeled by the Kirchhoff approximation. The second region, commencing roughly 8 to 10 msec after the pulse has arrived, is dominated by scattering from the rough surface, and can be modeled by the Rayleigh-Rice approximation. There were no visible effects of a sub-surface bubble layer because the data were taken at large grazing angles and low wind speeds.

Chapter 3

FLIP Experiment

3.1 Introduction

This chapter describes bistatic surface scattering measurements made during January of 1992 from the FLIP, FLoating Instrument Platform, freely floating about 400 nmi off the coast of California. The experiment was planned and conducted by Peter Dahl and Andrew Jessup of APL-UW, and was primarily directed toward investigating the relationship between ocean surface conditions, the near-surface bubble layer, and high frequency acoustic forward and backscatter. In this chapter, the means by which data were tested and validated as homogeneous is described. The data's statistical characteristics and bistatic surface scattering strengths will be investigated in Chapters 4 and 5 respectively.

3.2 Geometry

The geometry for the FLIP experiment is shown in Figure 3.1, which is taken from [18]. A detailed description of FLIP can be found in [19].
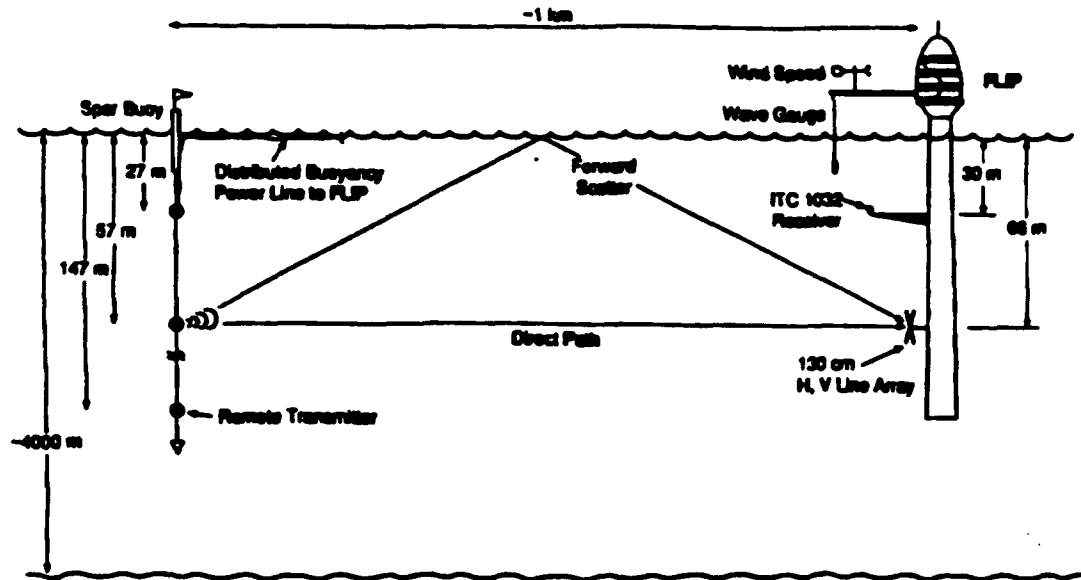
Figure 3.1: Experimental Set-up for FLIP Data.

3.3 Transmitter and Receiving Array

Three spherical sources were suspended below a spar buoy allowed to drift approximately 1000 meters from FLIP. The sources were at depths of 27, 57 and 147 m. Any one of the three sources could be selected to transmit. The transmitted pulse was received by horizontal and vertical line arrays mounted on FLIP's hull at a depth of 66.3 m. Each line array was composed of 84 omnidirectional elements with 0.0153 m spacing. The 84 omnidirectional elements were grouped into 4 staves, each with 21 elements. The signals from each stave, eight in all, were shifted down to a center frequency of 5 KHz and sampled at 20 KHz.

The water depth at the experiment site was approximately 4000 meters.

The depth of the water kept the returns at the line arrays limited to just the direct path, the specular reflection from the surface and the surface scatter.

3.3.1 Processing the Line Array Data

The objective in processing or combining line array stave data was to resolve a single, small scattering patch on the surface so that the bistatic surface scattering strengths derived from the data could be related to particular geometrical parameters. This section discusses four possible methods of processing the line array data and shows that using the horizontal array alone proved to be best choice for resolving the scattering patch.

The four possible methods of processing the line array data were to form a Mills Cross array of the horizontal and vertical arrays, form a sum array of the horizontal and vertical arrays, use the vertical array alone or use the horizontal array alone. The four resulting beam pattern plots are shown in Figures 3.2 through 3.5.

Summing the returns from the four vertical staves and multiplying by the sum of the four horizontal staves outputs produces a Mills Cross array [17]. Processing the output of the line arrays in this manner produces a beam pattern that is the product of the beam patterns of the horizontal and vertical line arrays. A plot of the Mills Cross array beam pattern is included in Figure 3.2. There is a 0 dB peak at 0° bearing and 0° elevation and high sidelobes in the horizontal and vertical planes.
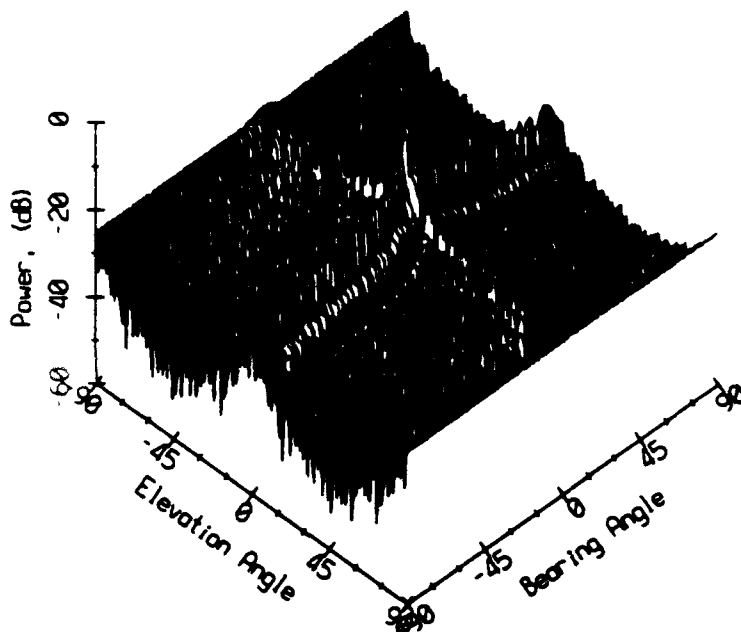
Figure 3.2: Mills Cross Array Beam Pattern.

Adding all eight staves produces a sum array with a beam pattern containing very high sidelobes in the horizontal and vertical planes. The sum array improves the signal-to-noise ratio when compared to either of the line arrays treated separately, in contrast to the Mills Cross array, which was found to suffer from a lower signal-to-noise ratio when compared to either of the line arrays treated separately. A plot of the sum array beam pattern is included in Figure 3.3 and shows the same general shape as the Mills Cross array but with higher sidelobes.

Summing the staves separately for each line array produces the expected beam pattern. In Figure 3.4, the vertical line array beam pattern is shown. Note that there is a plane of ambiguity at 0° elevation. In Figure 3.5 the horizontal line array beam pattern is shown with the ambiguity plane at 0° bearing. The ridges at
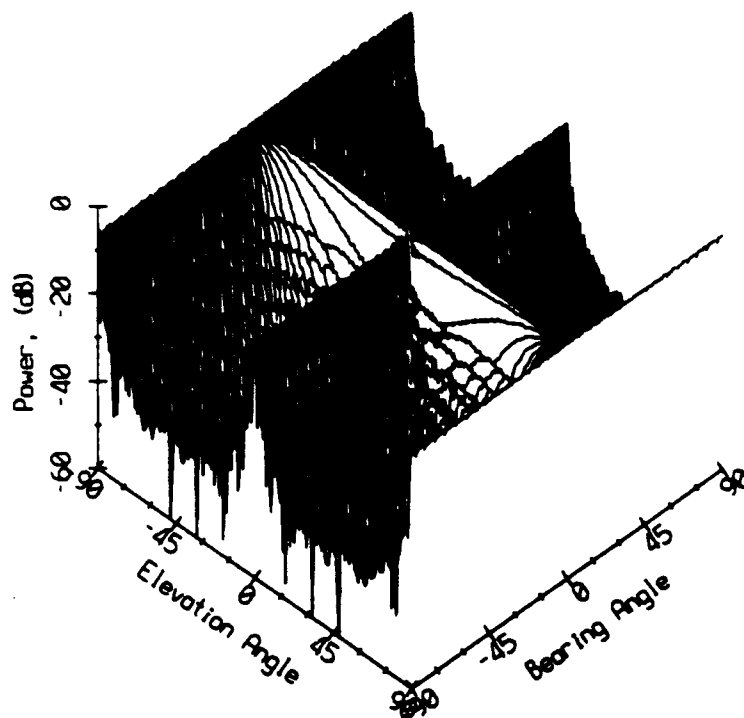
Figure 3.3: Sum Array Beam Pattern.

±90° elevation are actually points, in that bearing angle has no meaning at these elevation angles.

The detrimental effect of the ambiguity plane at 0° elevation in all the beam patterns except that of the horizontal array alone proved to be the reason for using the horizontal array alone.

A graphical representation of this problem is given next. In Figure 3.6, the scattering patches are shown at 675, 700, 725, 750, 775 and 800 msec after transmit for the horizontal array alone. Here the scattering patch is defined as all those points within 3 dB of the maximum of the beam pattern gains minus the transmission and attenuation losses. In Figure 3.6, the source is located at (-500.0, 0.0) and the receiver at (500.0, 0.0). The scattering patch for time 675
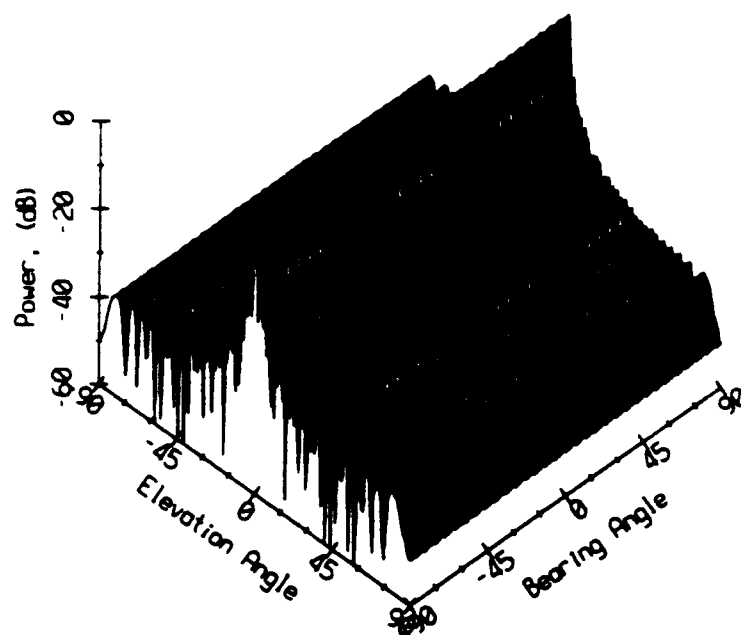
Figure 3.4: Vertical Line Array Beam Pattern.
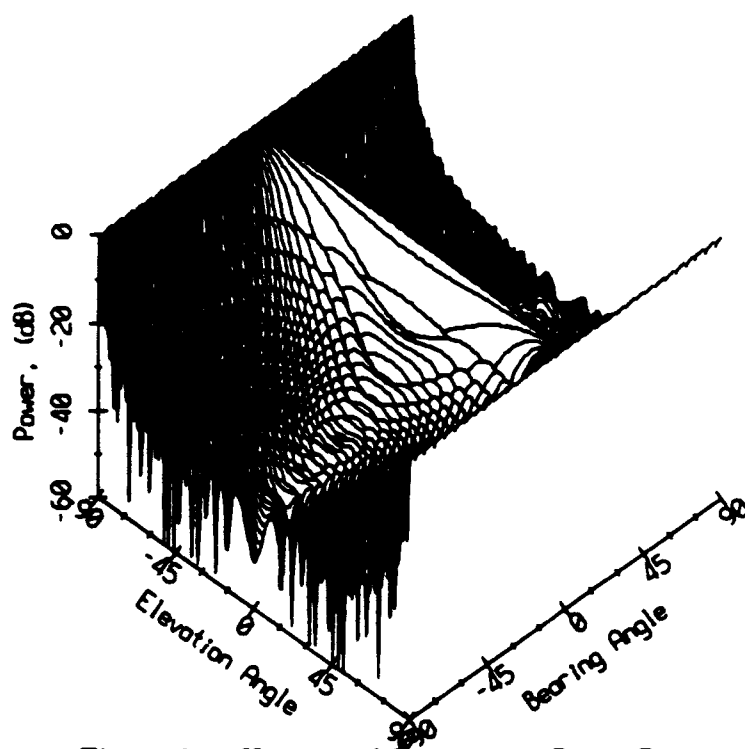
Figure 3.5: Horizontal Line Array Beam Pattern.
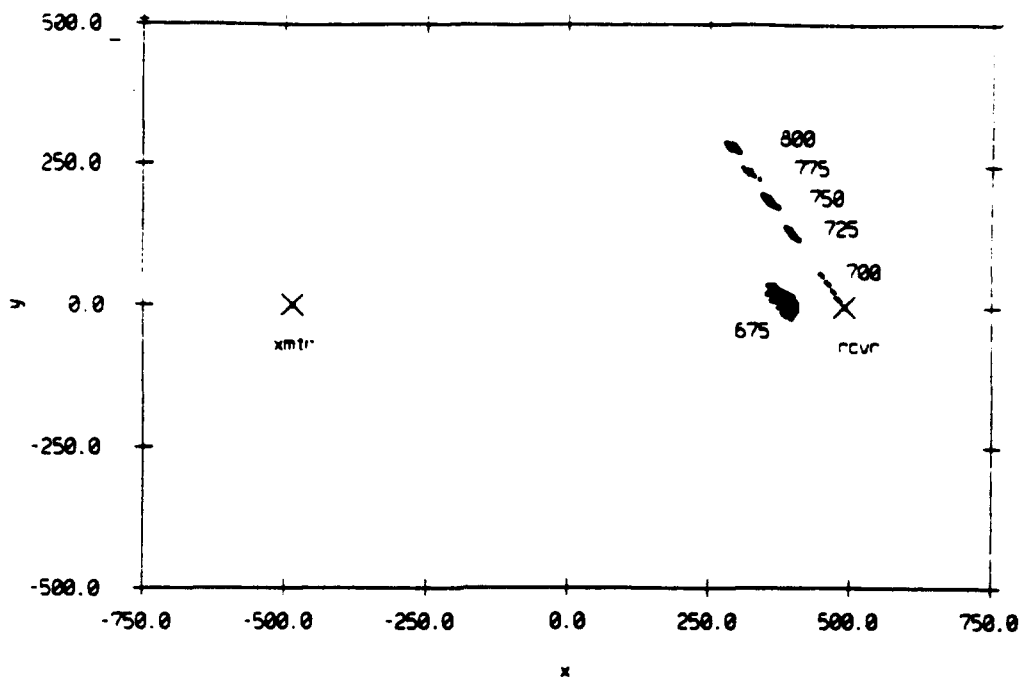
Figure 3.6: Scattering Patches (within 3 dB) for Horizontal Array at Times 675 to 800 msec in 25 msec intervals.

msec is located at approximately (350.0, 0.0). The scattering patches for times 700 to 800 msec start close to the receiver and move away from the receiver for longer times. Figure 3.7 is analogous to Figure 3.6 except that the scattering patches are defined as all those points within 15 dB of the maximum value. The increase in the scattering patch area between Figure 3.7 and Figure 3.6 is confined to the area around the same physical location on the surface at each time and is up to a factor of three times larger except at time 675 msec.

In contrast, Figure 3.8 shows the scattering patch defined as those points within 3 dB of the maximum for the same times as before but for the sum beam pattern. The scattering patch at three of the six times is not contiguous. In Figure 3.9, the sum beam 15 dB scattering patches are shown. For all times, the scattering patches are not contiguous and it is impossible to relate a single geometry
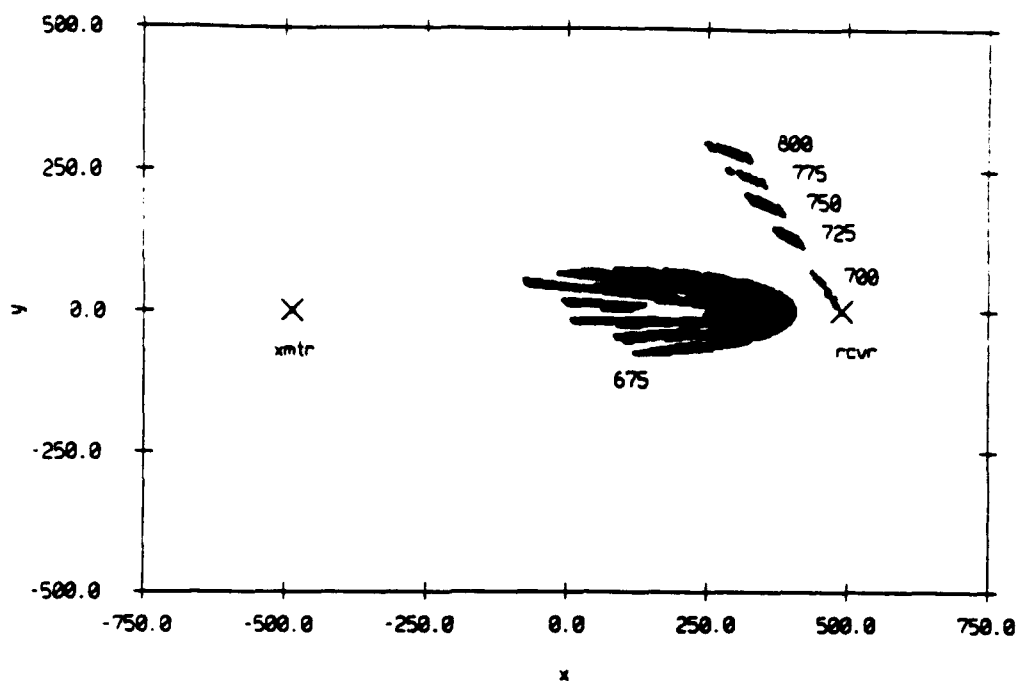
Figure 3.7: Scattering Patches (within 15 dB) for Horizontal Array at Times 675 to 800 msec in 25 msec intervals.
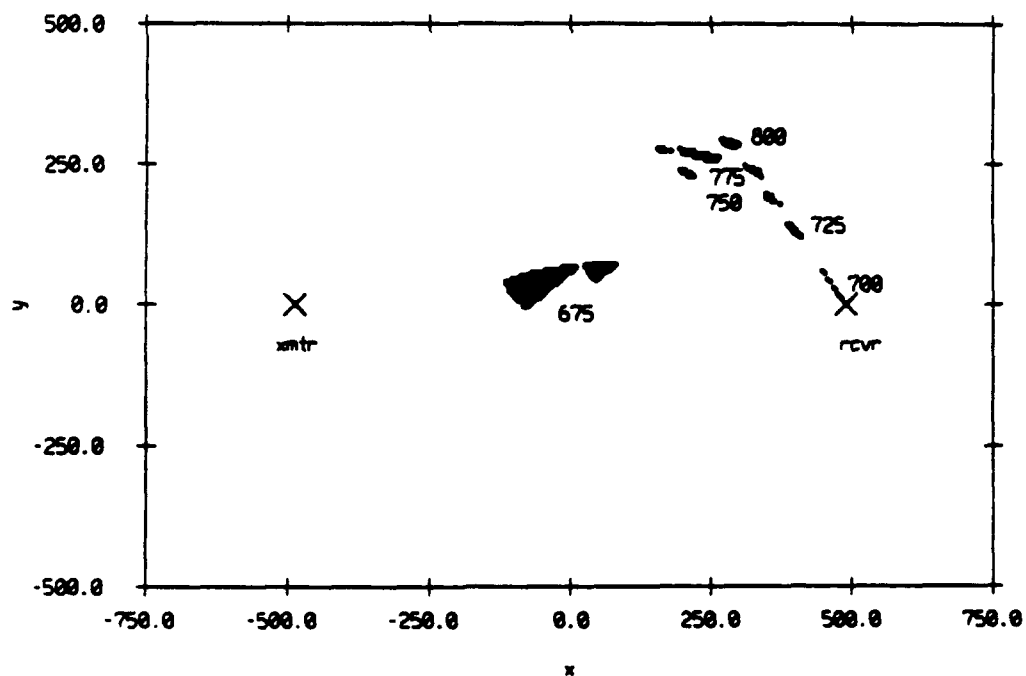
Figure 3.8: Scattering Patches (within 3 dB) for Sum Array at Times 675 to 800 msec in 25 msec intervals.
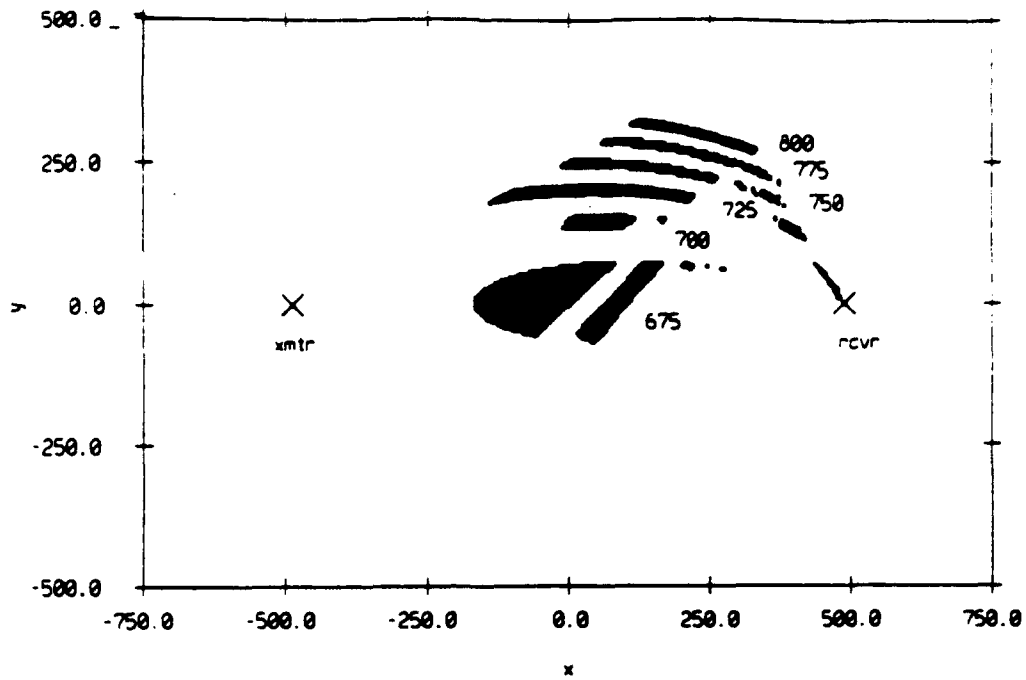
Figure 3.9: Scattering Patches (within 15 dB) for Sum Array at Times 675 to 800 msec in 25 msec intervals.

to a bistatic surface scattering strength measurement. This is also true with all array configurations which include the vertical array because of its ambiguity plane at 0° elevation.

3.4 Environmental Parameters Measured

Environmental parameters measured during the FLIP experiment include wind speed, wind direction, and air temperature. The sound speed profile was measured twice daily during the entire experiment. The environmental data is used to investigate the effects of the environment on bistatic scattering strengths.

Table 3.1: Transmitter Information for Bistatic Surface Scattering Portion of the FLIP Experiment.

Run	Freq (KHz)	Pulse (ms)	SL (dB)	# of Pings
fwd-las.102	30	8	188.2	50
fwd-las.103	30	8	188.2	50
fwd-las.104	30	4	189	25
fwd-las.105	30	4	189	25
fwd-las.106	30	4	189	25
fwd-las.107	30	4	189	25
fwd-las.108	40	10	193	25
fwd-las.112	30	1	198	20
fwd-las.112	40	1	197	20
fwd-las.116	30	1	195	25
fwd-las.117	30	1	195	25

3.5 Acoustic Data

The bistatic surface scattering measurements made during the FLIP experiment are described in the Tables 3.1, 3.2 and 3.3. Run refers to the type of data, where fwd-las means forward line array sonar, and the number indicates a particular data set. The elevation and bearing of the line arrays is given in Table 3.3 and is expressed in degrees. A bearing angle of $0°$ corresponds to the direction of the source and a elevation angle of $0°$ corresponds to horizontal. The time delay T_d, is the record start time referenced to the transmission of the pulse, and the time sample T_s is the length of the record time. Both are expressed in msec. The wind speed during each run is given in Table 3.4. At the experiment site, the received signals were shifted down to a center frequency of 5 KHz with a bandwidth of 10

Table 3.2: Transmitter Location during Bistatic Surface Scattering Runs.

Run	Source Depth (m)	Source Range (m)
fwd-las.102	147	977
fwd-las.103	147	977
fwd-las.104	57	999
fwd-las.105	57	1002
fwd-las.108	147	714
fwd-las.112	147	980
fwd-las.116	147	715
fwd-las.117	147	712

Table 3.3: Receiver Information for Bistatic Surface Scattering Portion of FLIP Experiment.

Run	Rec. Elev.	Rec. Brng.	T_d	T_s	Gain (dB)
fwd-las.102	10	55	600	200	50
fwd-las.103	20	55	600	200	50
fwd-las.104	15	83	600	200	50
fwd-las.105	5	83	600	200	50
fwd-las.108	15	8	450	100	38
fwd-las.112 (30KHz)	2.5	55	650	100	50
fwd-las.112 (40KHz)	2.5	55	650	100	50
fwd-las.116	2.5	30	475	100	56
fwd-las.117	2.5	60	475	100	56

Table 3.4: Measured Wind Speeds for Bistatic Surface Scattering Measurements.

Runs	Date	Time	Wind Speed (m/s)
fwd-las.102	1/17/92	1535	7.2
fwd-las.103	1/17/92	1536	7.2
fwd-las.104	1/18/92	1930	5.5
fwd-las.105	1/18/92	2036	5.8
fwd-las.108	1/21/92	1208	1.4
fwd-las.112	1/22/92	2005	5.3
fwd-las.116	1/24/92	1140	5.3
fwd-las.117	1/24/92	1154	4.9

KHz and then sampled at 20 KHz. The data were stored in two byte binary format, time multiplexed for the 8 staves.

3.6   Testing for Homogeneity

Before investigating the statistics of the time series, the stationarity of the data was verified using the two-sample Kolmogorov-Smirnov test. The procedure used was the same as detailed in Section 2.1.3. Again, the purpose of this test is to determine whether the statistical characteristics of the reverberation changed between the first half and second half of the transmitted pulses. This is an important step because the test for normality is only valid if the statistics of the entire ensemble are homogeneous.

The procedure for checking the data for homogeneity was to divide the data into a first half and a second half and then calculate a cumulative distribution

Table 3.5: Test Thresholds for K-S Test for Homogeneity.

Run	Z_α	n_1	n_2
fwd-las.102	.345	25	25
fwd-las.103	.345	25	25
fwd-las.104	.488	12	13
fwd-las.105	.488	12	13
fwd-las.108	.488	12	13
fwd-las.112	.545	10	10
fwd-las.116	.488	12	13
fwd-las.117	.488	12	13

function, *cdf*, at each time for each half. Then, one finds the maximum deviation between the two *cdf*'s at each time and uses this value, Z_{sample}, as the test sample statistic. This value, Z_{sample}, is compared with the test threshold, Z_α. The test threshold was calculated using the formula

$$Z_\alpha = 1.22\sqrt{\frac{n_1 + n_2}{n_1 n_2}} \tag{3.1}$$

where n_1 and n_2 are number of data points in the two ensembles being compared [9]. In this application of the K-S test, n_1 is equal to the number of pulses in the first half of the ensemble, n_2 is equal to the number of pulses in the second half of the ensemble and the confidence level, α, is equal to 0.1. The values of Z_α used in the test for homogeneity as well as the values of n_1 and n_2 are shown in Table 3.5. Test results are displayed in Figures 3.10 through 3.12. It should be noted that

when testing large numbers of ensembles it is acceptable for up to $(100 \times \alpha)\%$ of the test statistics to exceed the threshold before the data set fails the test. Figures 3.10 through 3.12 show that all of the runs pass the test for homogeneity using the Kolmogorov-Smirnov test with a confidence level of $\alpha = 0.10$ in that no more than 10% of the test statistics exceed the threshold for any run.

3.7 Conclusion

By testing data for homogeneity, one can avoid the mistake of averaging over a period of time during which the underlying statistics change significantly. This is an important consideration because derived values such as the bistatic surface scattering strength are inherently connected to statistical parameters such as the variance of the reverberant time series. If the variance changes during the sequence of transmitted pulses, then an estimate of the bistatic surface scattering strength averaged over the sequence will be inherently flawed.

With all the bistatic runs validated as homogeneous at a confidence level of $\alpha = 0.10$, they could then be tested for Rayleigh behavior and the bistatic surface scattering strength calculated as discussed in Chapters 4 and 5.
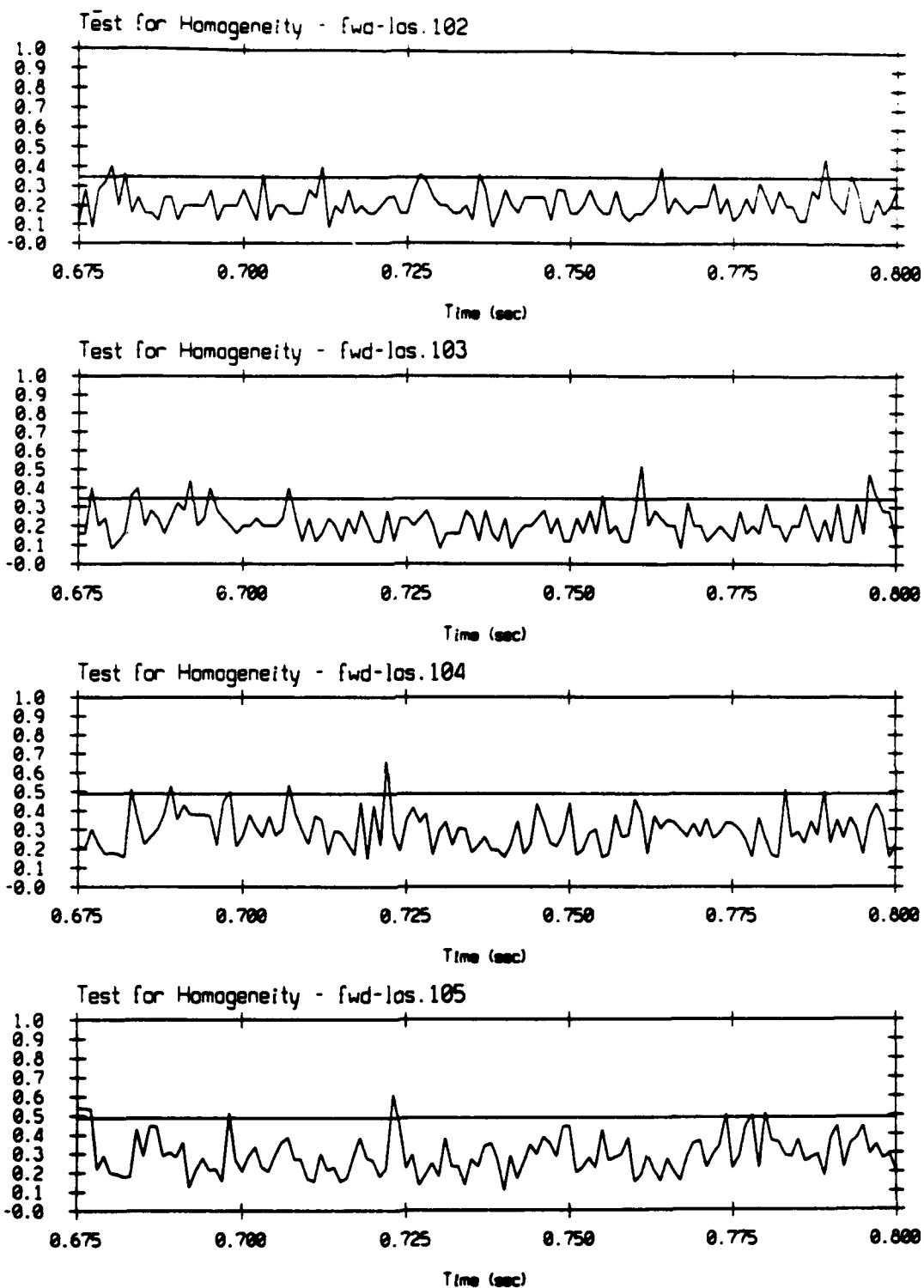
Figure 3.10: Testing for Homogeneity - fwd-las.102, 103, 104 and 105. Z_{sample} versus time (msec) is plotted. The horizontal line is Z_α.
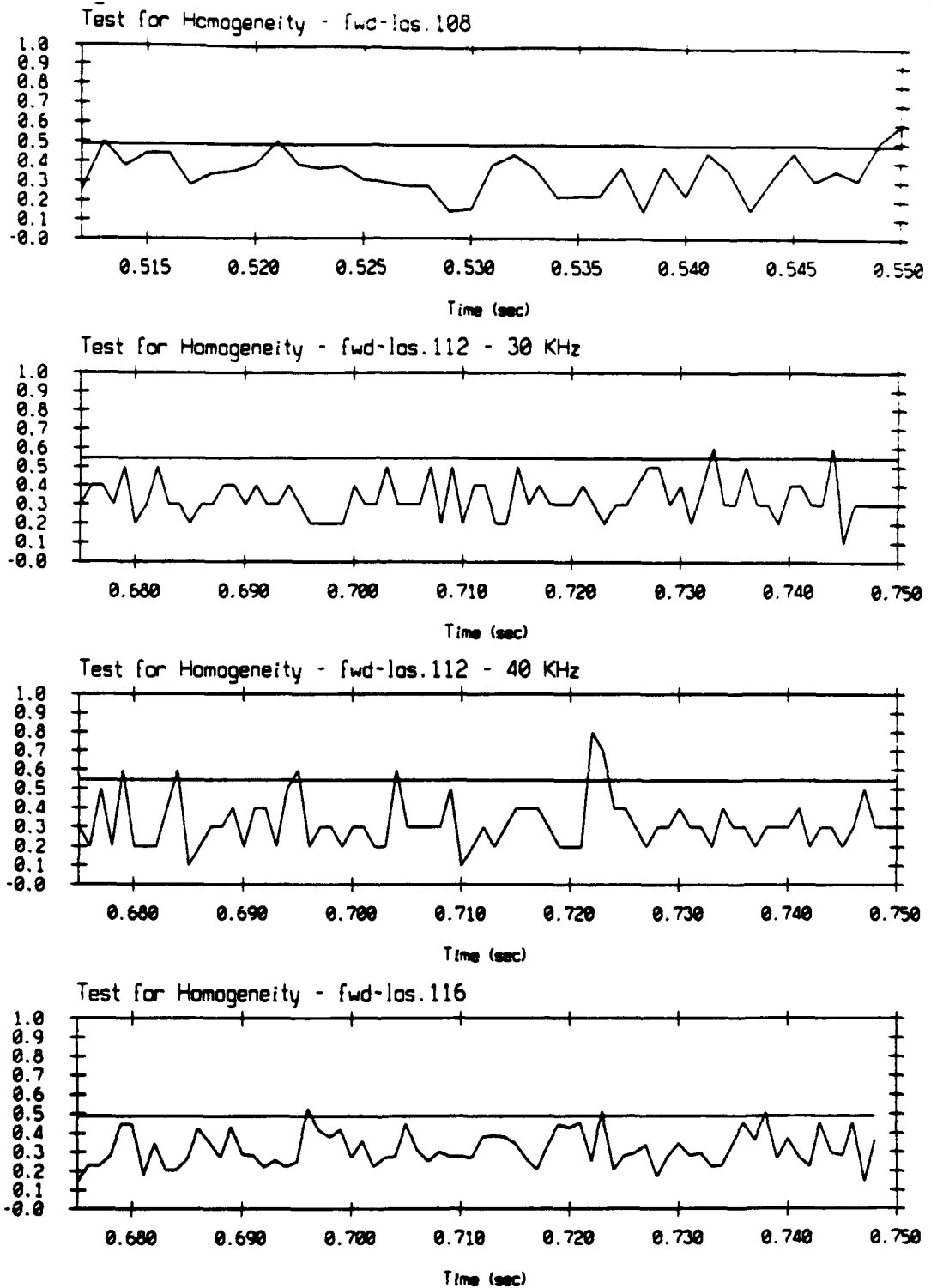
Figure 3.11: Testing for Homogeneity - fwd-las.108, 112 and 116. Z_{sample} versus time (msec) is plotted. The horizontal line is Z_α.
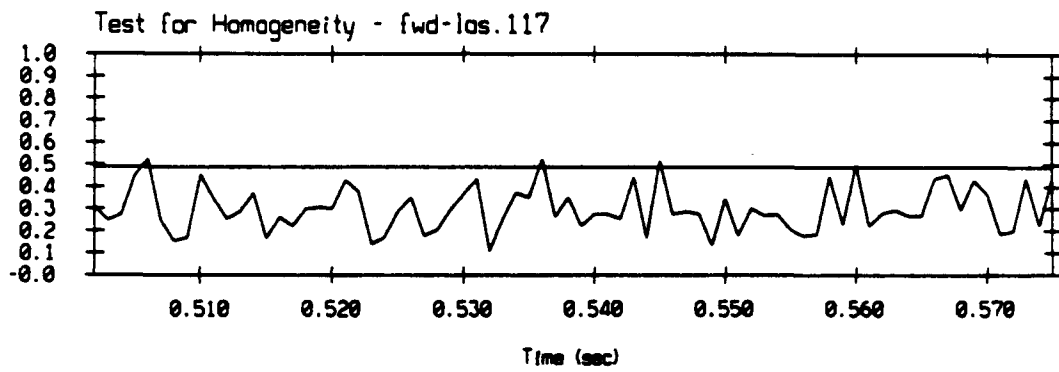
Figure 3.12: Testing for Homogeneity - fwd-las.117. Z_{sample} versus time (msec) is plotted. The horizontal line is Z_α.

Chapter 4

FLIP Data - Statistics

4.1 Introduction

In this chapter, the results of tests for Rayleigh behavior using both the Kolmogorov-Smirnov (K-S) two sample test and a combinational technique designed to increase the number of points in the ensembles are described. The combinational technique resolved detail in the tail of the distribution and revealed deviations from Rayleigh behavior at the 7.2 m/s wind speed which were not seen using the Kolmogorov-Smirnov test for Gaussian behavior.

4.2 K-S Test for Normality

The two-sample K-S test can be applied in a somewhat different manner to that described in Chapter 3 to determine whether the data exhibit Gaussian statistical characteristics. For this application, the *cdf* of all of the pulses at a particular time is compared with the *cdf* of a Gaussian random sequence of 1000 points having the same mean and variance as that of the pulses. The test statistic is taken to be the maximum deviation between the two *cdf's*, and is compared to a test threshold as before. Table 4.1 shows the values of the test threshold (with $\alpha = 0.1$) and the values of n_1 and n_2 used in the test for normality.

Table 4.1: Test Thresholds for K-S Test for Normality.

Run	Z_α	n_1	n_2
fwd-las.102	.176	50	1000
fwd-las.103	.176	50	1000
fwd-las.104	.247	25	1000
fwd-las.105	.247	25	1000
fwd-las.108	.247	25	1000
fwd-las.112	.275	20	1000
fwd-las.116	.247	25	1000
fwd-las.117	.247	25	1000

The results of the test for normality are shown in Figures 4.1, 4.2 and 4.3. All runs passed the test in that few points exceed the threshold. However, there are two deficiencies of this result. First, each value of Z_{sample} is based upon at most 50 reverberation data samples. This is too few samples to observe deviations in the tails of the distribution, where events occur only once in, say 10^3 samples. Second, the K-S test looks at the entire distribution, whereas we are most interested in the shape of the distribution tails. In the next section, the data statistics are investigated in a manner which remedies both deficiencies.

4.3 Testing the Envelope for Rayleigh Behavior

In order to increase the number of samples in the test for normality, data from different times were normalized and combined into a single ensemble. Portions of the time series in which a single mechanism was dominant, either surface
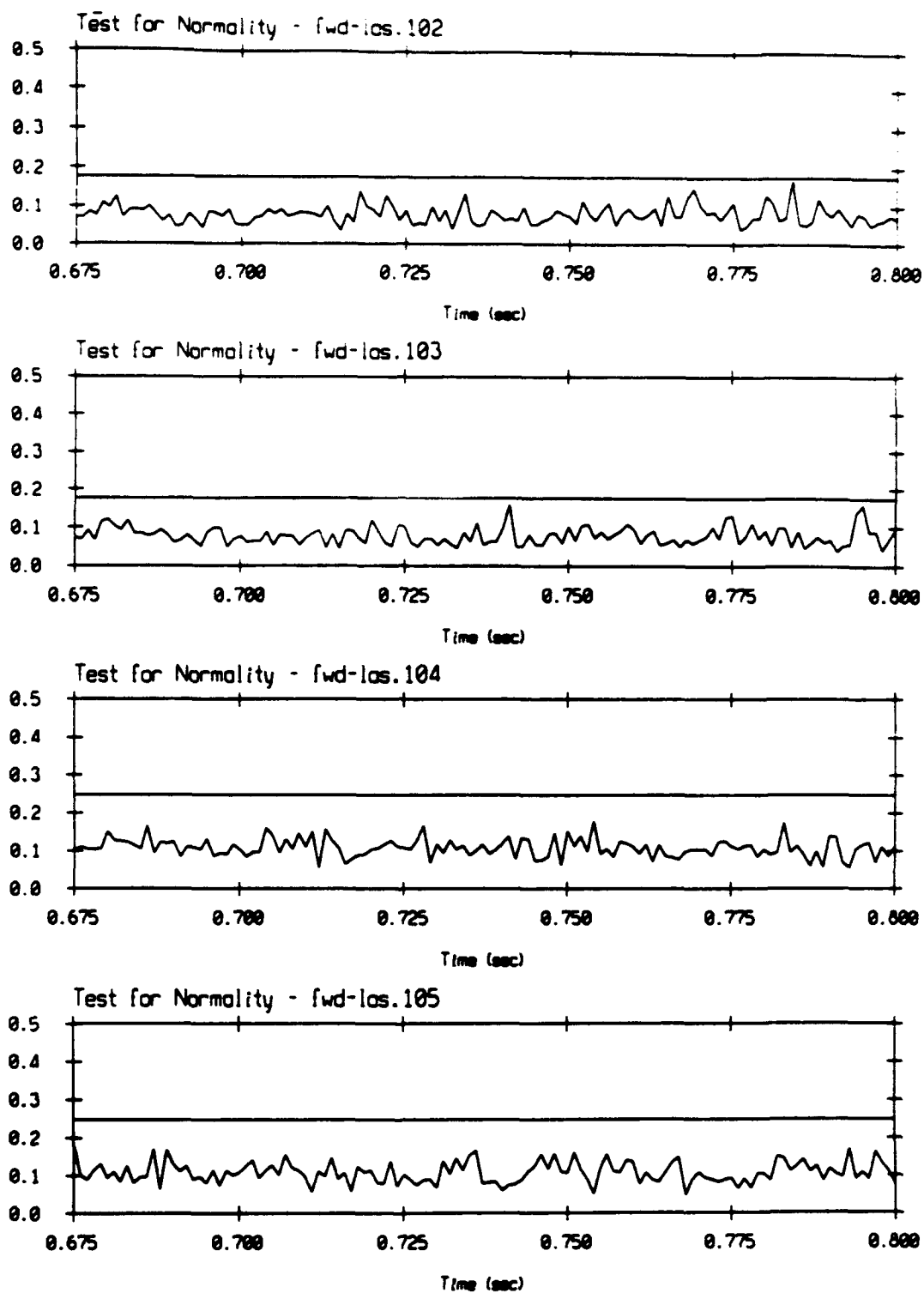
Figure 4.1: Testing for Normality - fwd-las.102, 103, 104 and 105. Z_{sample} versus time (msec) is plotted. The horizontal line is Z_α.
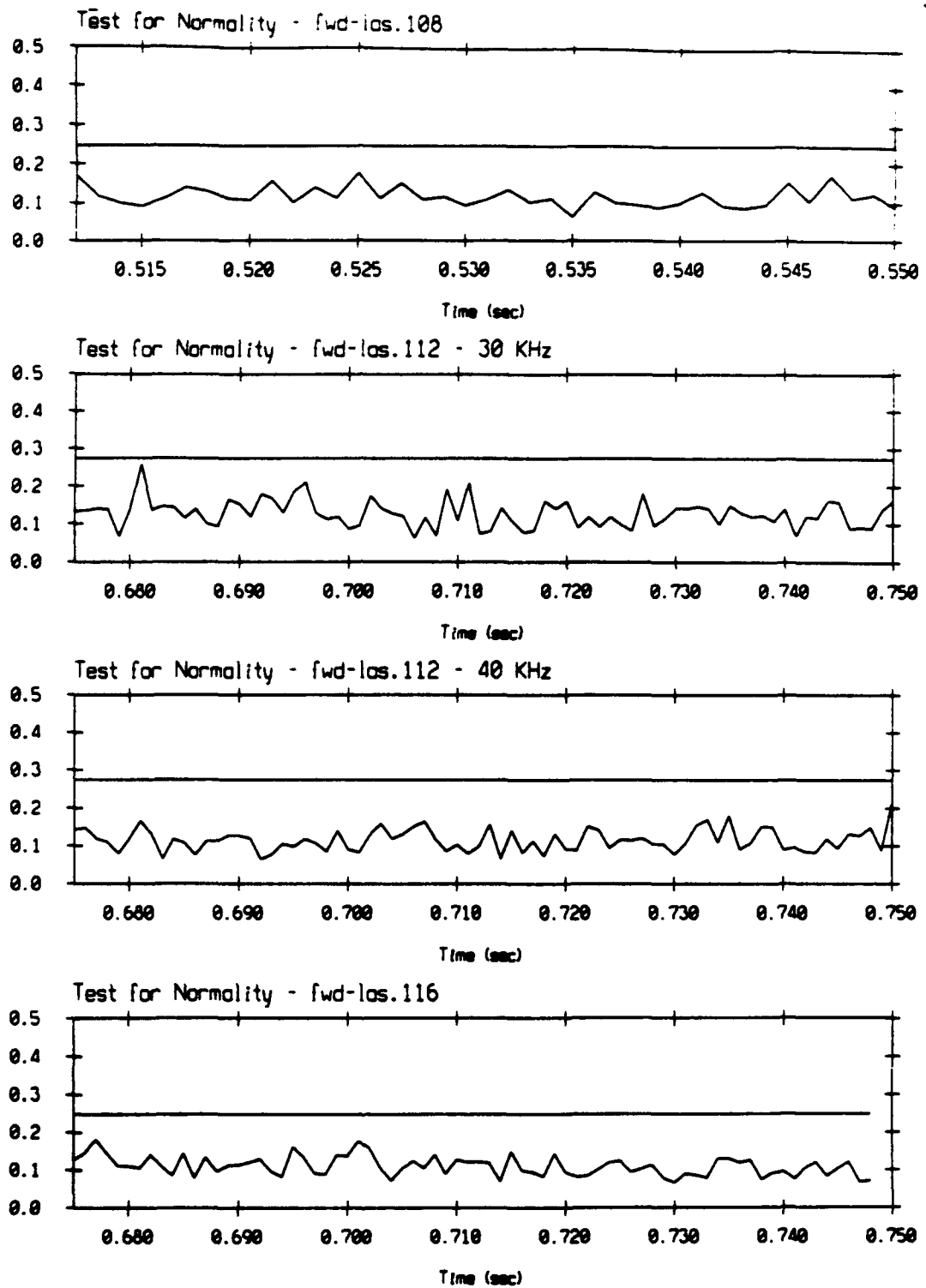
Figure 4.2: Testing for Normality - fwd-las.108, 112, and 116. Z_{sample} versus time (msec) is plotted. The horizontal line is Z_α.

Test for Normality - fwd-las.117
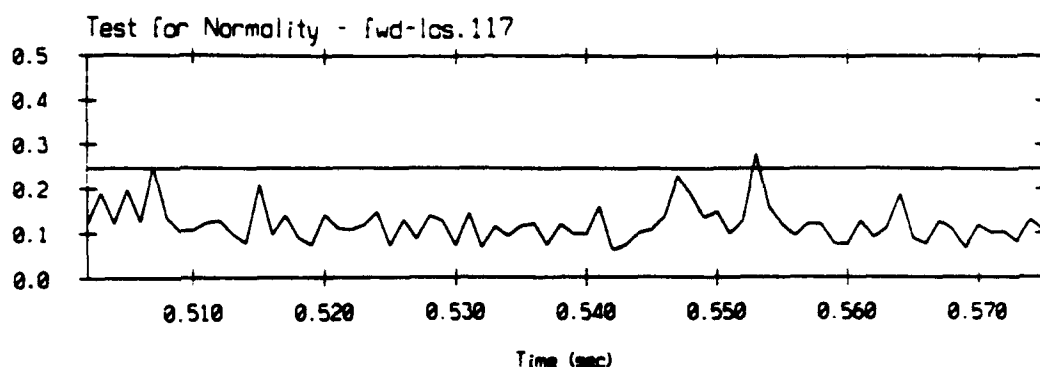
Figure 4.3: Testing for Normality - fwd-las.117. Z_{sample} versus time (msec) is plotted. The horizontal line is Z_α.

scattering or bubble scattering, were combined. Based upon work by Urick and Hoover [4] and Culver and McDaniel [3], the initial reverberation return is due to high angle scattering and is governed by surface scattering. At later times, bubble scattering is dominant. The time at which the crossover occurs was determined using the McDaniel theory for predicting bistatic surface scattering strength, which separately predicts the effects of surface roughness and the bubble layer. Table 4.2 shows the time period and available data points during which each mechanism was dominant. A portion of each run is dominated by surface scattering and a portion is dominated by bubble scattering, except for run fwd-las.108 which is entirely dominated by surface scattering.

The equivalency of testing for Rayleigh behavior in the magnitude of the complex envelope and testing for normal behavior in the time series is discussed in [10]. Basically, if the real and imaginary parts of a complex time series are normally distributed random variables, the magnitude of the complex envelope will have a

Table 4.2: Receiver Information for FLIP Data.

Run	Begin Time	End Time	# points	Mechanism
fwd-las.102	.675	.715	250	Surface
fwd-las.102	.715	.800	550	Bubbles
fwd-las.103	.675	.724	350	Surface
fwd-las.103	.725	.800	500	Bubbles
fwd-las.104	.675	.724	325	Surface
fwd-las.104	.725	.800	475	Bubbles
fwd-las.105	.680	.722	275	Surface
fwd-las.105	.723	.800	500	Bubbles
fwd-las.108	.510	.550	100	Surface
fwd-las.112 (30KHz)	.675	.721	920	Surface
fwd-las.112 (30KHz)	.722	.750	560	Bubbles
fwd-las.112 (40KHz)	.675	.721	920	Surface
fwd-las.112 (40KHz)	.722	.750	560	Bubbles
fwd-las.116	.502	.531	725	Surface
fwd-las.116	.532	.575	1075	Bubbles
fwd-las.117	.502	.537	875	Surface
fwd-las.117	.538	.575	925	Bubbles

Rayleigh distribution.

Once a basebanded, filtered complex time series was calculated, the linear magnitude was taken and subsampled by the length of the pulse to provide independent sample of the magnitude of the complex envelope. The data for each time were normalized to a mean of 10 and a variance of 1. Setting the mean to 10 ensured all the samples were positive. The normalized data for each time were then combined with data from other times with the same dominant scattering mechanism. The P_{FA} was generated by histogramming the ensemble and taking one minus the *cdf*.

The results are plotted on a log-log scale with normalized envelope level on the horizontal axis and the probability of false alarm, P_{FA}, on the vertical axis. The P_{FA} highlights deviations from Rayleigh behavior in the tails of the distribution. An example of this type of analysis used on bottom backscatter is given in an article by Boehme and Chotiros [20].

4.3.1   Surface Roughness Scattering

The P_{FA} results are presented in order of decreasing wind speed since the wind speed is the driving force behind surface disturbance. The order of the runs is given in Table 4.3, which shows the run, the wind speed and the transmit frequency. Note that all of the data presented are at 30KHz, except for fwd-las.112, which is at 30 and 40 KHz, and fwd-las.108, which is at 40 KHz. Only the surface scattering statistics for run fwd-las.102 showed meaningful deviations from the Rayleigh distribution based on a visual inspection of the plots. Fwd-las.102 shows

Table 4.3: Runs Ordered by Wind Speed.

Run	Wind Speed (m/s)	Freq.(KHz)
fwd-las.102	7.2	30
fwd-las.103	7.2	30
fwd-las.105	5.8	30
fwd-las.104	5.5	30
fwd-las.116	5.3	30
fwd-las.112	5.3	30 and 40
fwd-las.117	4.9	30
fwd-las.108	1.4	40
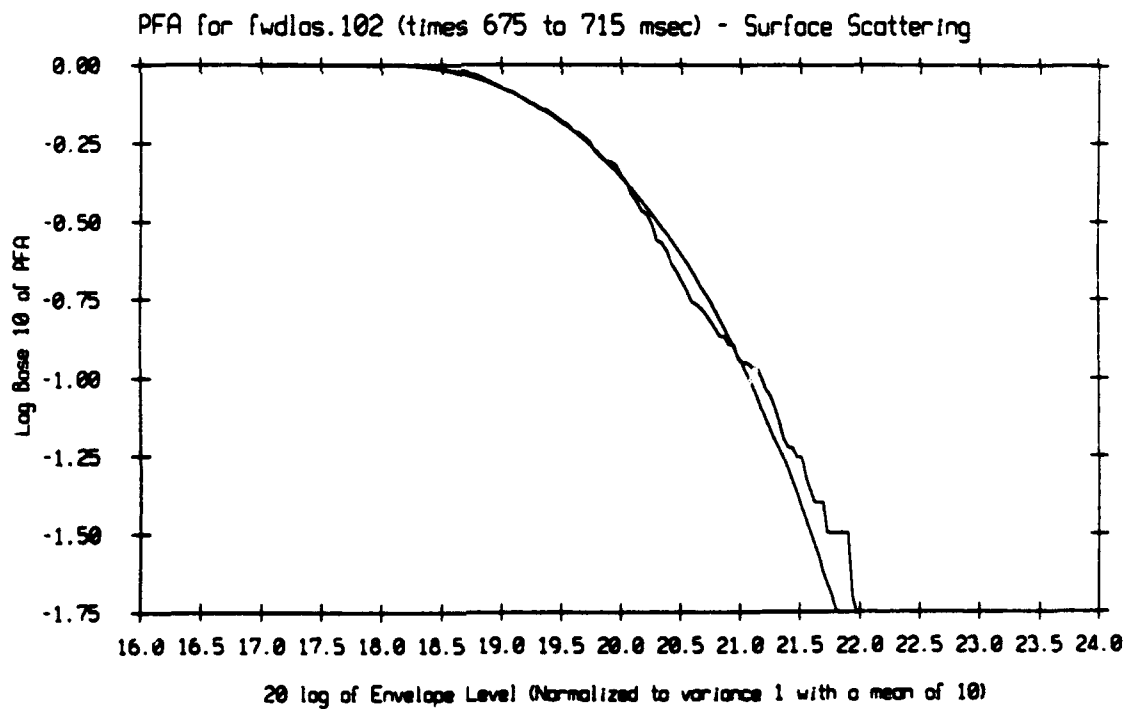
Figure 4.4: Surface Scattering Statistics fwd-las.102.

PFA for fwdlas.103 (times 675 to 724 msec) - Surface Scattering
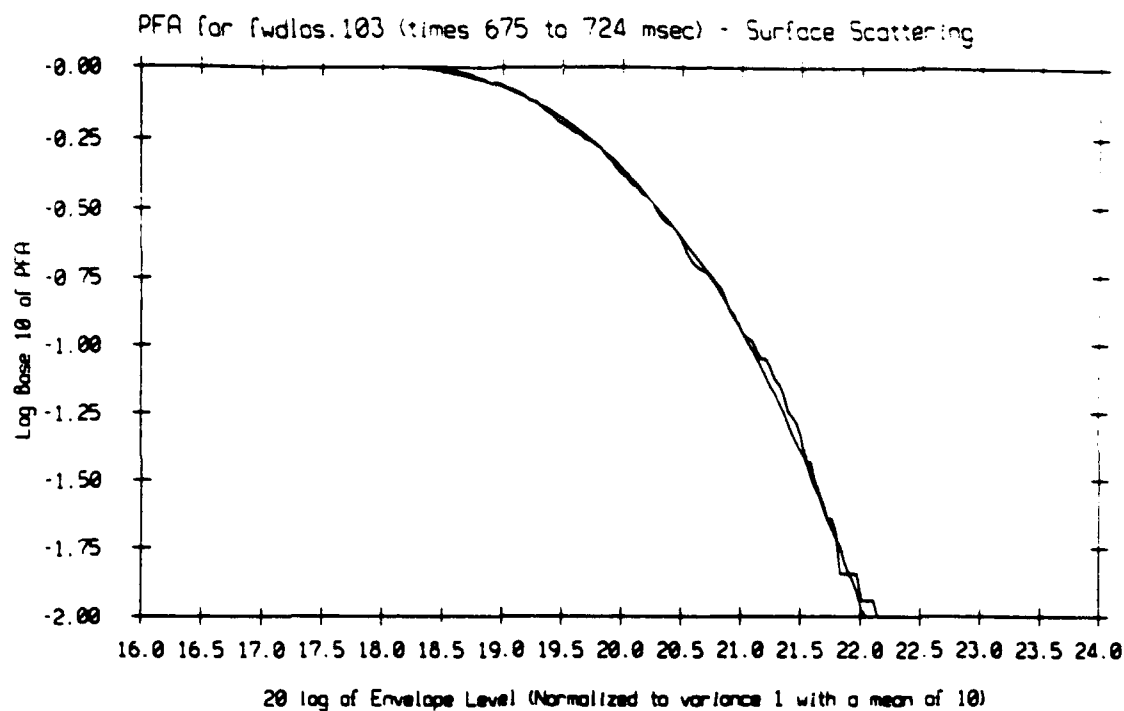
Figure 4.5: Surface Scattering Statistics fwd-las.103.

a somewhat higher probability of false alarm than Rayleigh in the tails of the distribution. This is not an unexpected result for a relatively high wind speed. This run occurred at the highest wind speed of all the runs, 7.2 m/s. It is interesting to note that run fwd-las.103, taken only minutes later with the same wind speed and an elevation of 20° instead of 10°, showed no significant deviation from the Rayleigh distribution.

4.3.2   Bubble Layer Scattering

As in Section 4.3.1, the P_{FA} results for scattering from the bubble layer are presented in order of decreasing wind speed. Significant deviation from the Rayleigh distribution occur only for runs fwd-las.102 and 103, the runs that occurred at the

PFA for fwdlas.105 (times 680 to 722 msec) - Surface Scattering
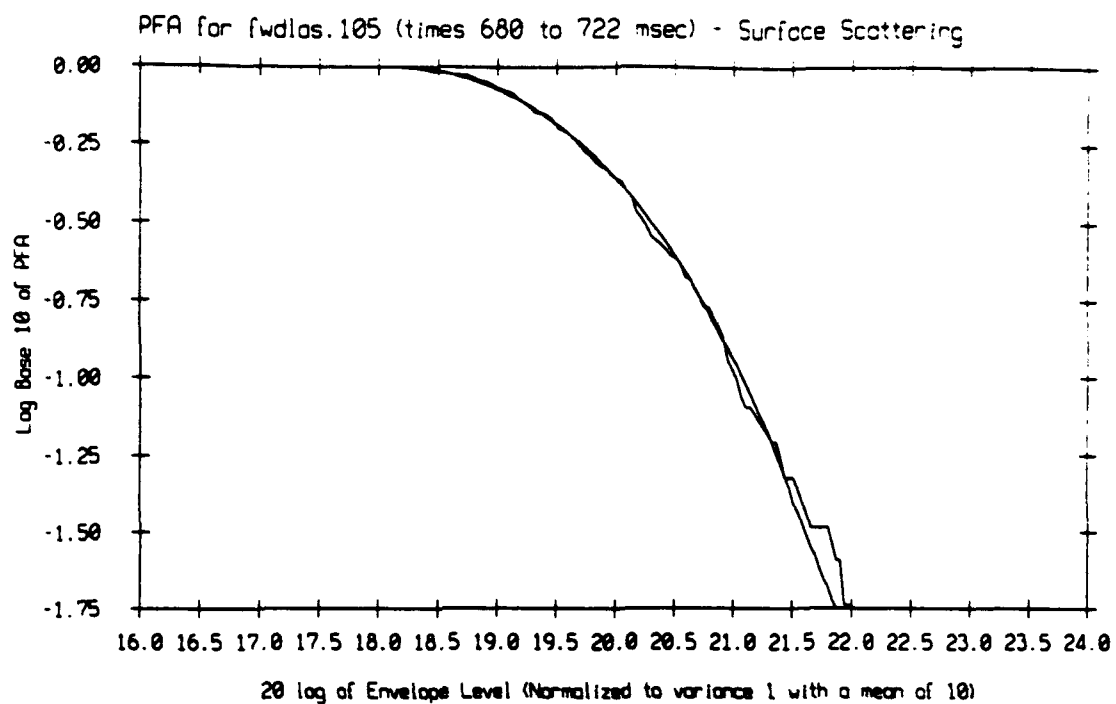
Figure 4.6: Surface Scattering Statistics fwd-las.105.

PFA for fwdlas.104 (times 675 to 724 msec) - Surface Scattering
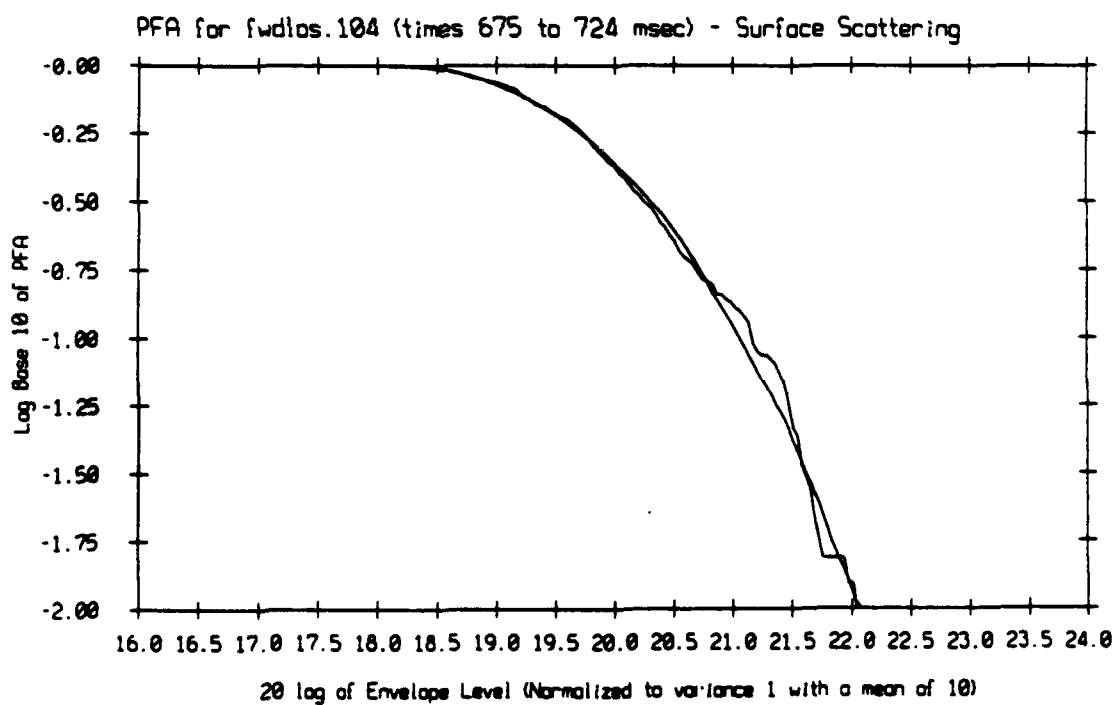
Figure 4.7: Surface Scattering Statistics fwd-las.104.

PFA for fwdlas.116 (times 502 to 531 msec) - Surface Scattering
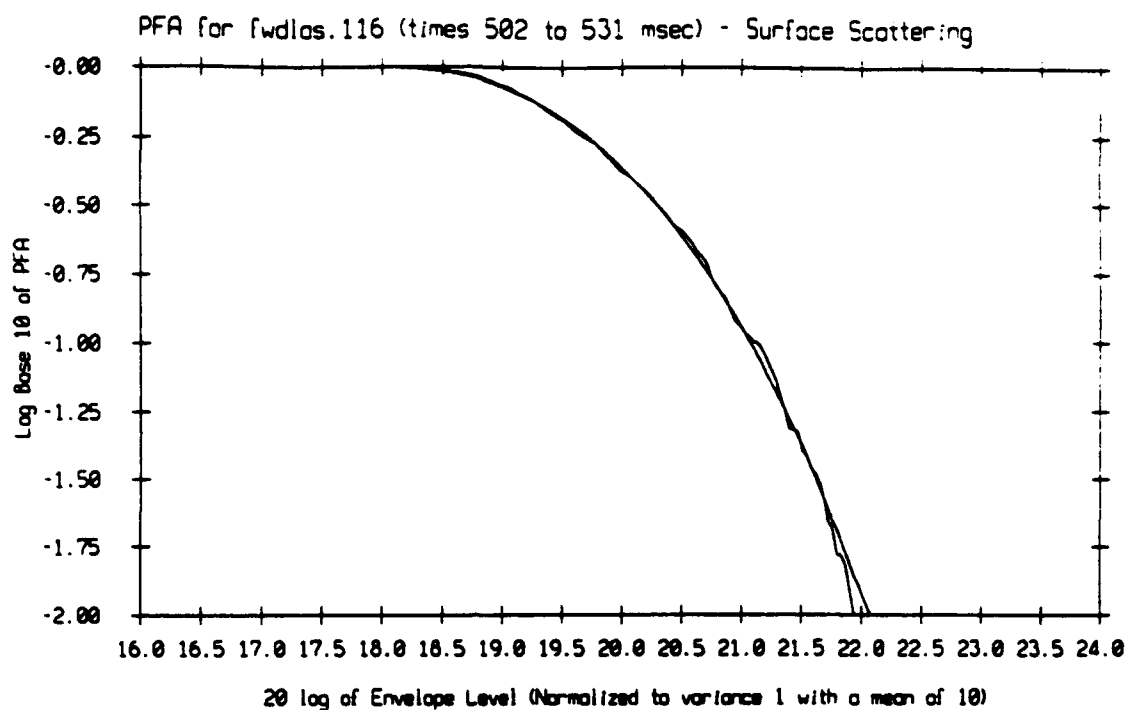
Figure 4.8: Surface Scattering Statistics fwd-las.116.

PFA for fwdlas.112 - 30KHz (times 675 to 721 msec) - Surface Scattering
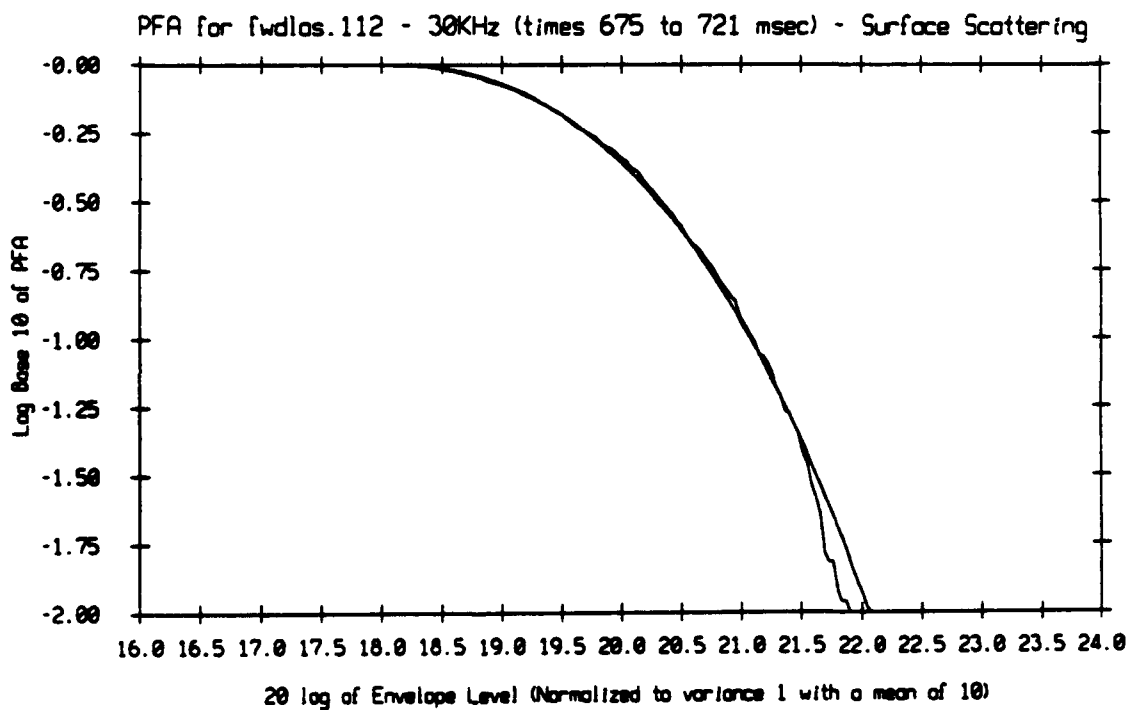
Figure 4.9: Surface Scattering Statistics fwd-las.112-30KHz.

PFA for fwdlas.112 - 40KHz (times 675 to 721 msec) - Surface Scattering
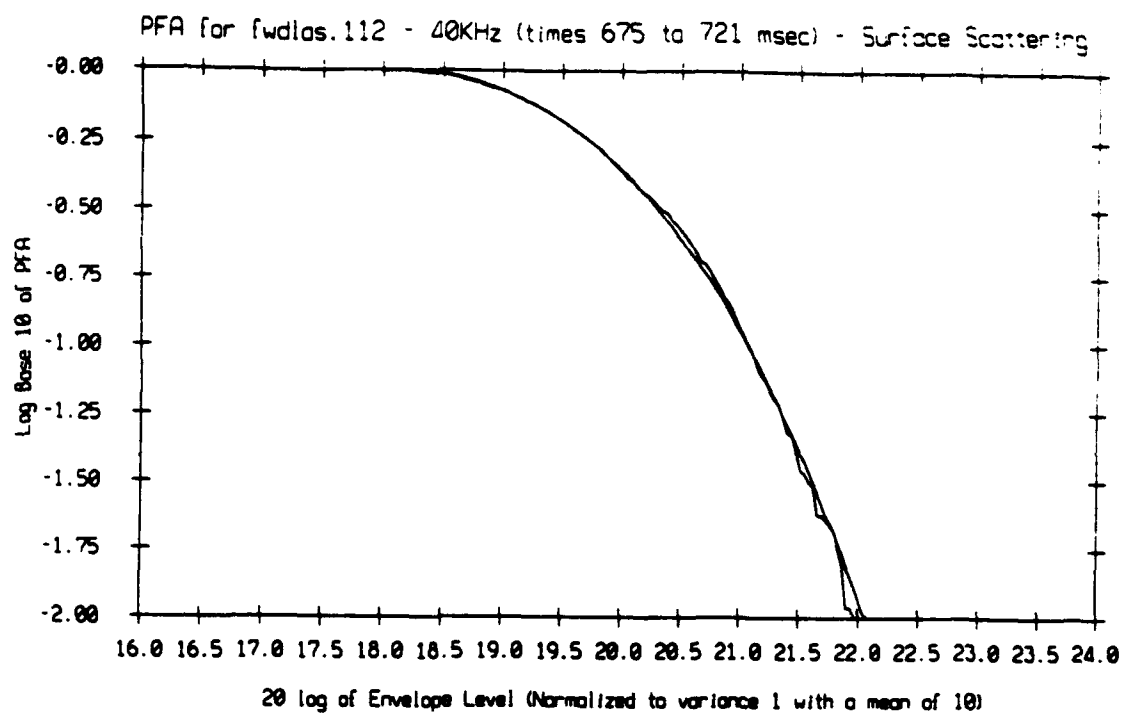
Figure 4.10: Surface Scattering Statistics fwd-las.112-40KHz.

PFA for fwdlas.117 (times 502 to 537 msec) - Surface Scattering
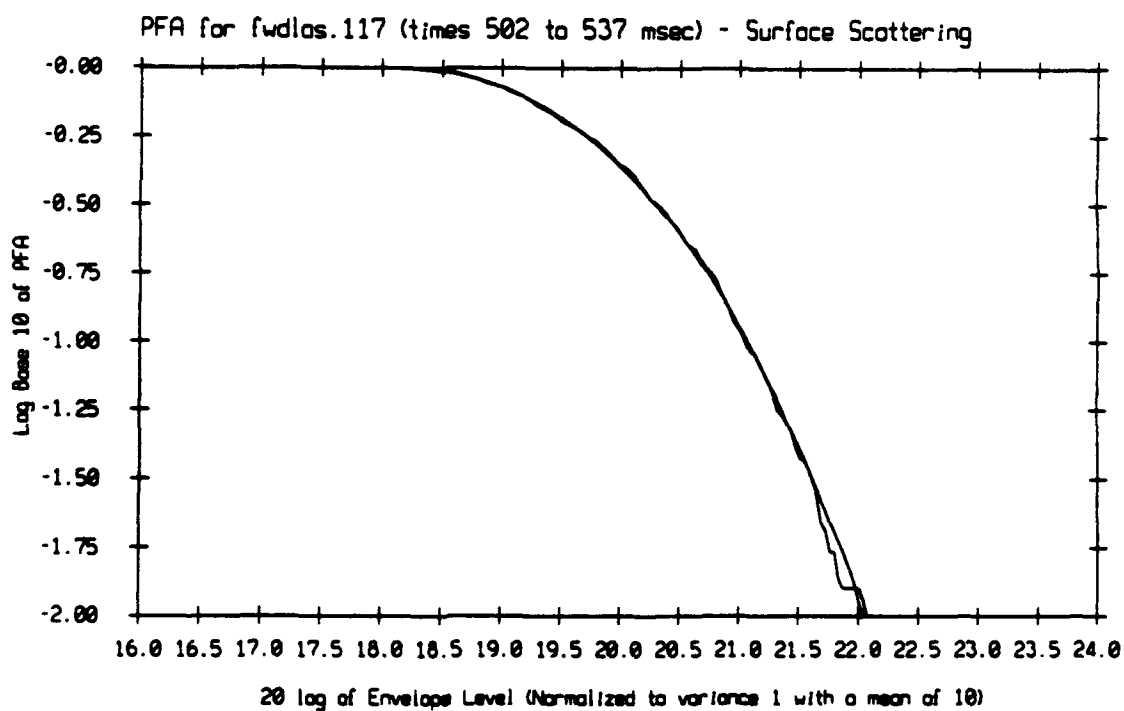
Figure 4.11: Surface Scattering Statistics fwd-las.117.

PFA for fwdlas.108 (times 510 to 550 msec) - Surface Scattering
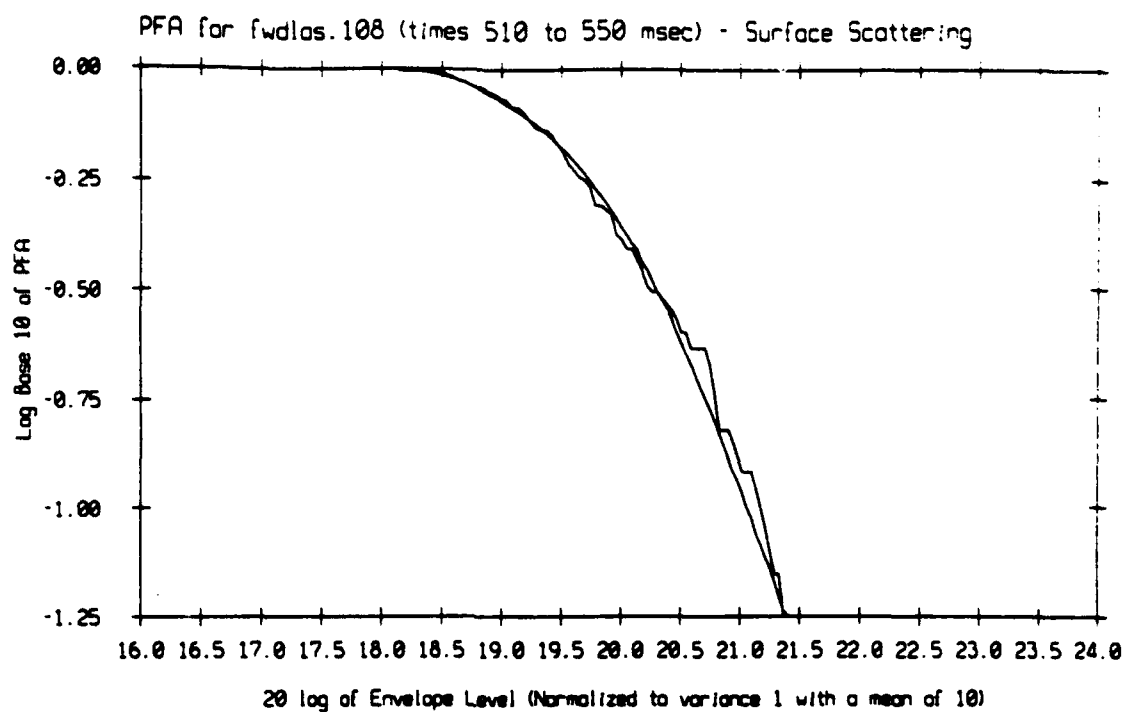
Figure 4.12: Surface Scattering Statistics fwd-las.108.

PFA for fwdlas.102 (times 715 to 800 msec) - Bubble Scattering
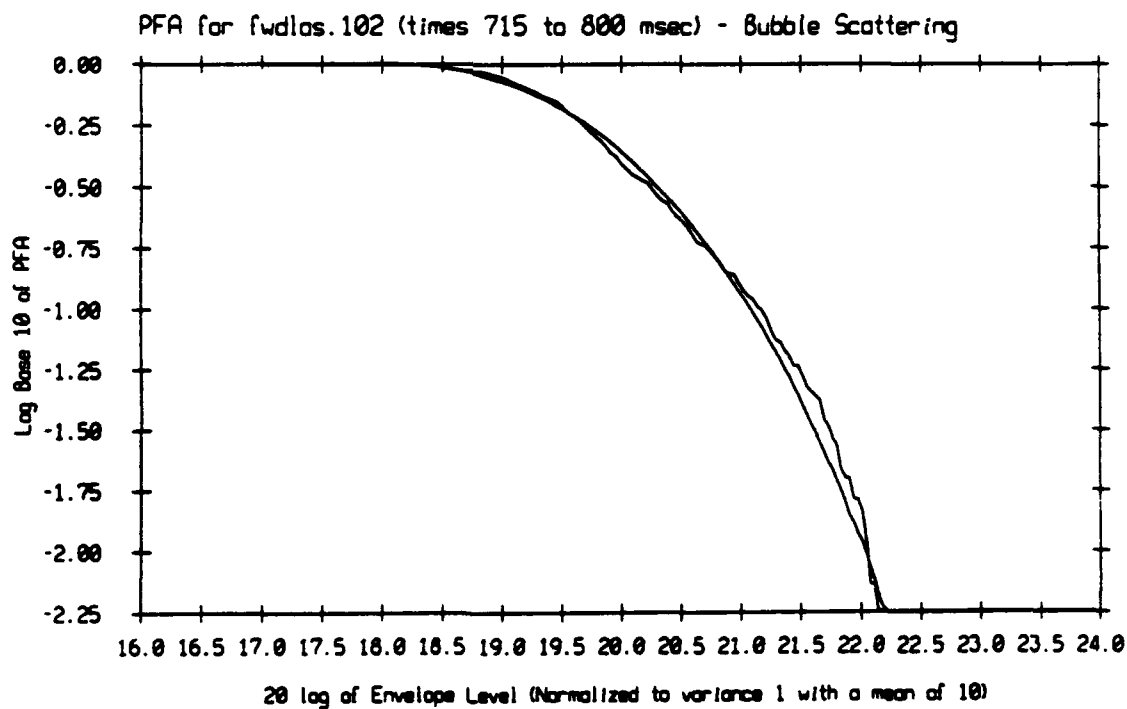
Figure 4.13: Bubble Scattering Statistics fwd-las.102.

PFA for fwdlas.103 (times 725 to 800 msec) - Bubble Scattering
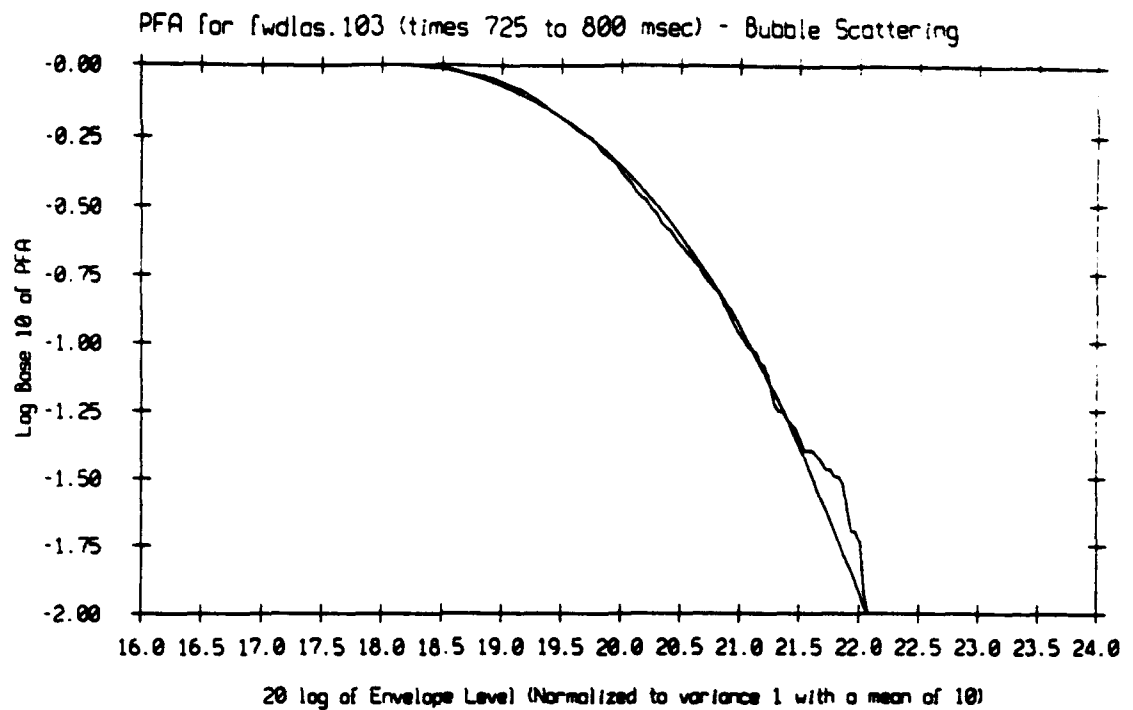
Figure 4.14: Bubble Scattering Statistics fwd-las.103.

highest wind speed, 7.2 m/s. The shape of the probability of false alarm curves for both runs fwd-las.102 and fwd-las.103 show the same trend. They are slightl: under and then slightly over the Rayleigh distribution further into the tail of the distribution. The rest of the plots for lower wind speeds show little deviation from the Rayleigh distribution.

4.4 Summary and Conclusions

While all of the data sets passed the K-S test for normality, this is not considered conclusive because only 25 to 50 points were available for an ensemble and because the K-S test does not focus on the tails of the distributions where non-Gaussian behavior is of most interest. In order to increase ensemble size, data

PFA for fwdlas.105 (times 723 to 800 msec) - Bubble Scattering
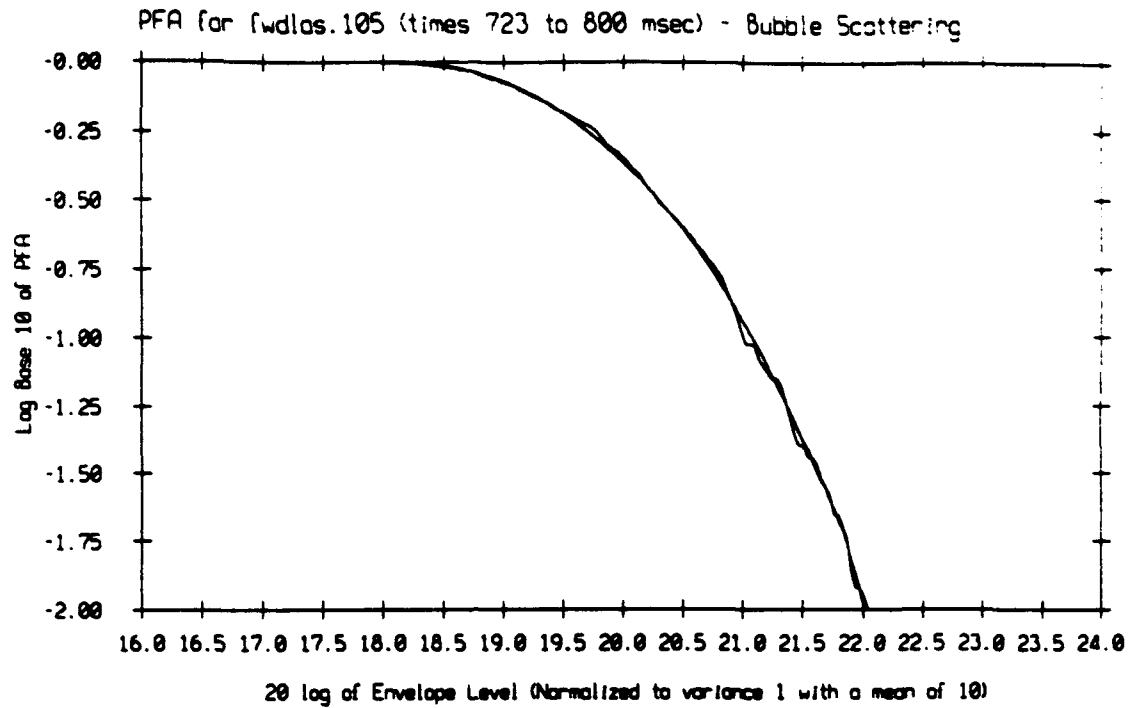
Figure 4.15: Bubble Scattering Statistics fwd-las.105.

PFA for fwdlas.104 (times 725 to 800 msec) - Bubble Scattering
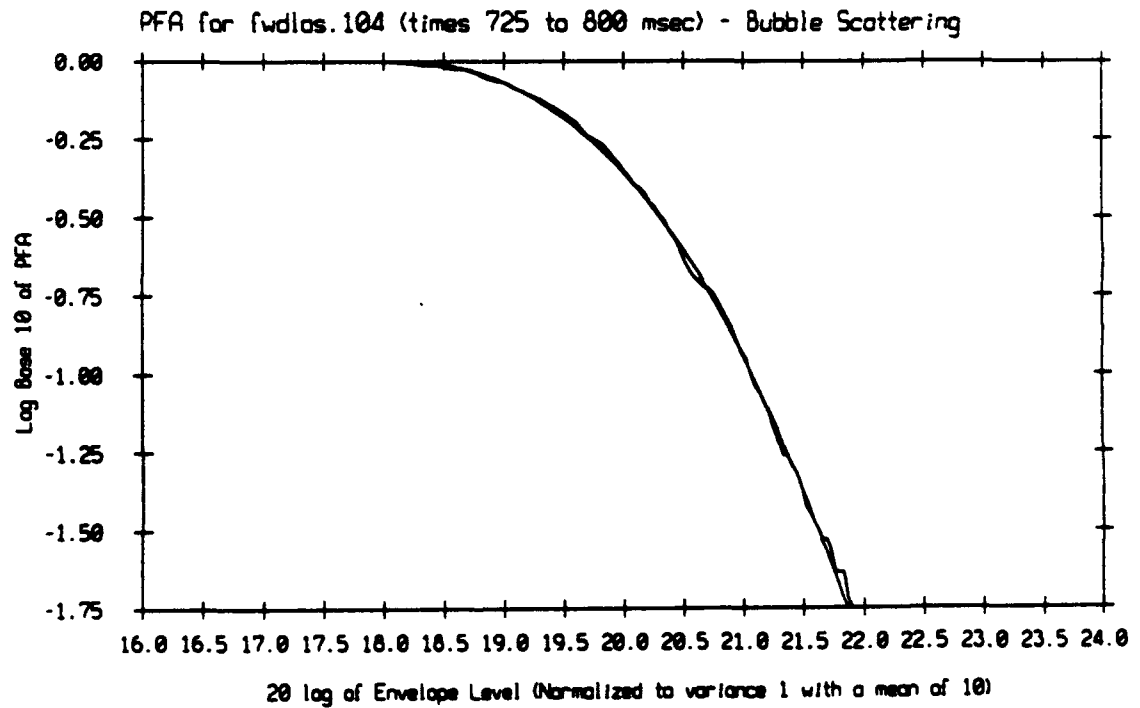
Figure 4.16: Bubble Scattering Statistics fwd-las.104.

PFA for fwdlas.116 (times 532 to 575 msec) - Bubble Scattering

20 log of Envelope Level (Normalized to variance 1 with a mean of 10)
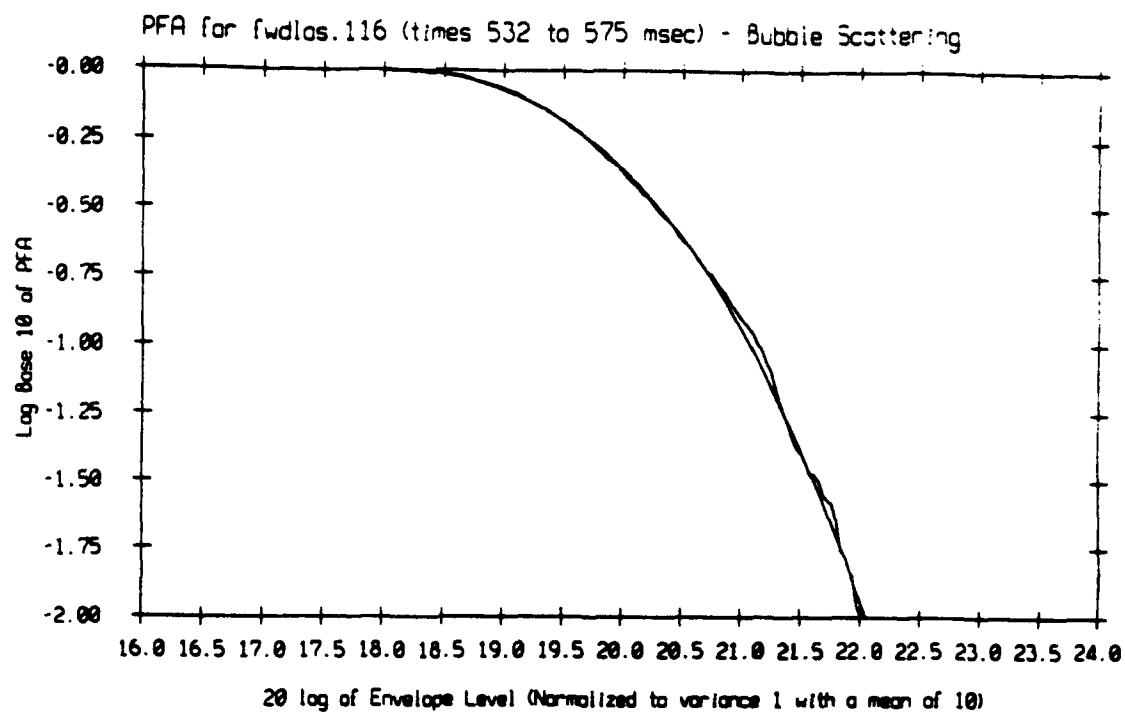
Figure 4.17: Bubble Scattering Statistics fwd-las.116.

PFA for fwdlas.112 - 30KHz (times 722 to 750 msec) - Bubble Scattering

20 log of Envelope Level (Normalized to variance 1 with a mean of 10)
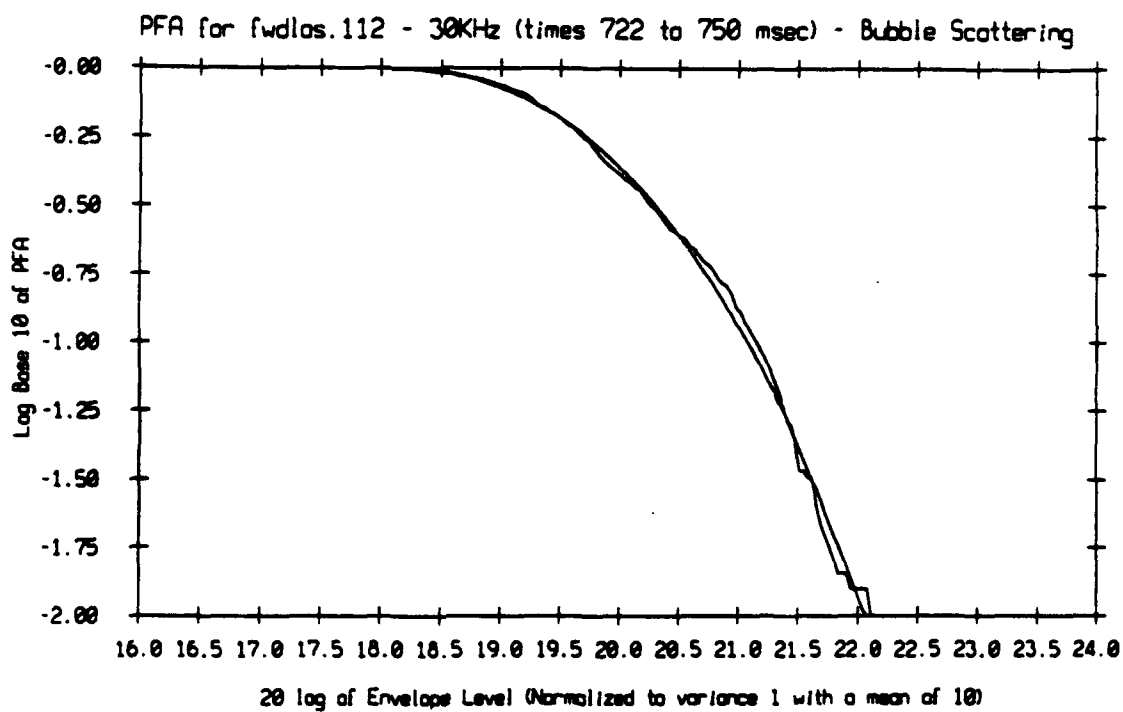
Figure 4.18: Bubble Scattering Statistics fwd-las.112-30KHz.

PFA for fwdlas.112 - 40KHz (times 722 to 750 msec) - Bubble Scattering
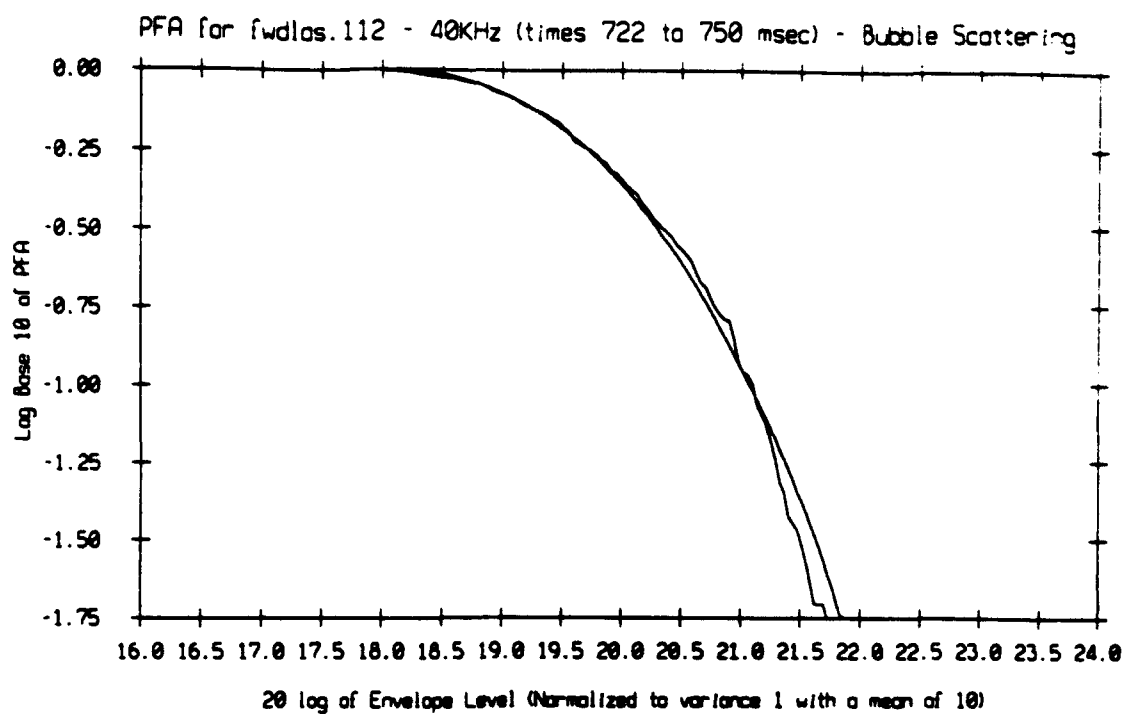
Figure 4.19: Bubble Scattering Statistics fwd-las.112-40KHz.

PFA for fwdlas.117 (times 538 to 575 msec) - Bubble Scattering
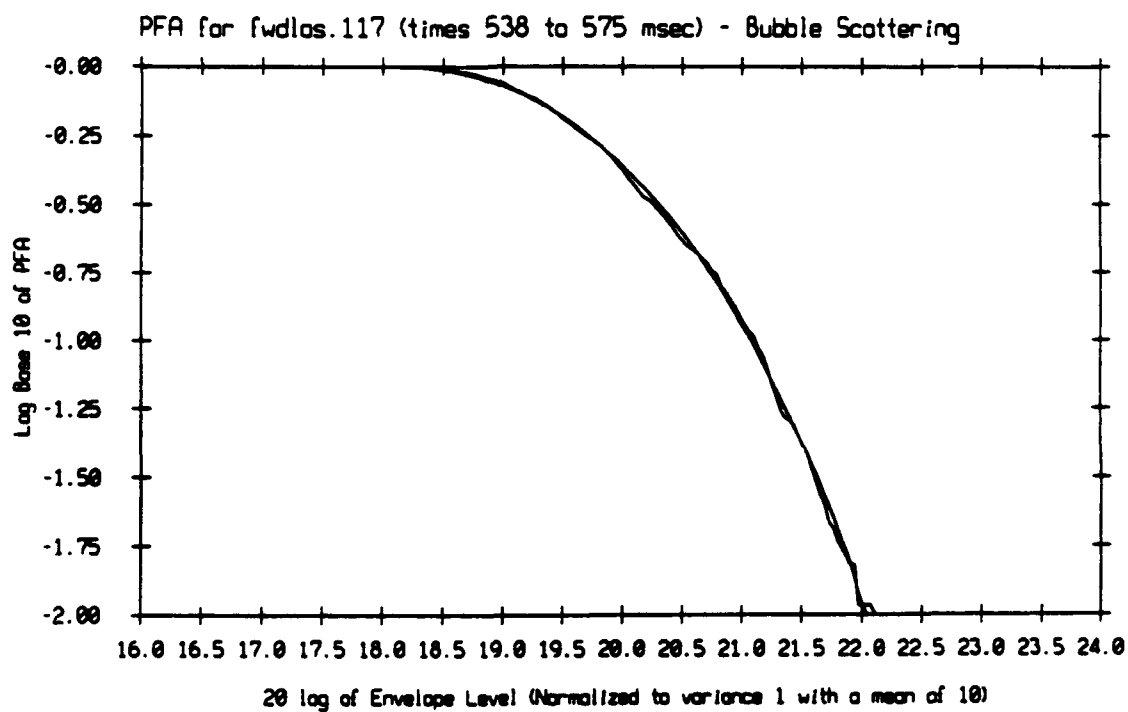
Figure 4.20: Bubble Scattering Statistics fwd-las.117.

from different times were normalized and combined for periods with a common dominant mechanism, either rough surface or bubble layer scattering, for each data run. A complex Gaussian distributed process will have a Rayleigh envelope, and the probability of false alarm, P_{FA}, was used to investigate non-Gaussian behavior in the distribution tails. It was found that for both mechanisms, surface roughness and bubble scatter, at the highest wind speed of 7.2 m/s, there were meaningful deviations from Rayleigh behavior. The deviations are well below the threshold of the K-S test with a confidence level of $\alpha = 0.1$, which shows the limitations of the K-S test in detecting deviations in the tails of distributions.

Chapter 5

FLIP Data - Bistatic Scattering Strengths

5.1 Introduction

This chapter discusses how the FLIP experiment data listed in Table 3.1 were processed to yield estimates of bistatic surface scattering strength for various geometries. Only data during the portion of the time series in which the scattering patch area was a single, relatively small area on the surface could be processed. In Chapter 6, the scattering strength estimates are compared to the McDaniel model.

5.2 Finding the Scattering Patch Area

A crucial first step in calculating bistatic surface scattering strength from the FLIP data is to estimate the scattering patch size and location. Appendix A provides the basics of bistatic scattering patch geometry. A computationally intensive grid search method was chosen to find the scattering patch. The alternative method required solving a system of non-linear equations to arrive at analytic expressions for the equi-time ellipses on the surface, at which point one would still have to incorporate the effects of beam gains, transmission losses and attenuation losses to arrive at an estimate of the scattering patch area. The method used in this thesis required calculating the ensonified area at each instant of time, then normal-

izing by the transmission losses, attenuation due to absorption, and beam patterns. The FORTRAN code used to estimate the bistatic surface scattering strength is included in Appendix B. The program places the source and receiver on the x axis symmetrically about the origin and then searches a grid of equally spaced points on the surface to find all the points which are within the equi-time ellipses delimited by the time of interest and the pulse length. For each point within the equi-time ellipse, the transmission losses, the beam pattern gains and the attenuation losses are calculated and summed into the variable *test*. The program finds the point which has the highest value of *test*, which corresponds to the point with the lowest losses. All the points whose value of *test* are within 3 dB of the maximum value of *test* are counted as part of the scattering patch, and the area of the scattering patch is taken to be the number of points times the grid spacing squared. The size of the grid spacing is then reduced by a factor of two and the process repeated to arrive at another estimate of the scattering patch area. If the second estimate satisfies the inequality

$$1.25 \times A_{spacing/2} > A_{spacing} > 0.8 \times A_{spacing/2} \qquad (5.1)$$

then the area calculated using the smaller spacing is used. If this inequality is not satisfied, the spacing is again reduced by a factor of two and the area recalculated. The process stops when Equation 5.1 is satisfied.

With this estimate of the scattering patch area, A, bistatic surface scatter-

ing strength was calculated using the sonar equation solved for the bistatic surface scattering strength.

$$SS = RL + TL_{1A} + TL_{2A} - SL - 10\log A - BG + \alpha R_{1A} + \alpha R_{2A} \qquad (5.2)$$

The terminology used in the sonar equation above is as follows.

- SS is the bistatic surface scattering strength (dB).

- RL is the received level at the hydrophone (dB//μPa).

- TL_{1A} is the transmission loss from the source to the scattering patch (dB).

- TL_{2A} is the transmission loss from the scattering patch to the receiver (dB).

- SL is the source level (dB//μPa @ 1m).

- A is the ensonified area (m^2).

- BG is the beam gain (dB).

- α is the attenuation coefficient (dB/m).

- R_{1A} is the distance from the source to the scattering patch (m).

- R_{2A} is the distance from the scattering patch to the receiver (m).

However, before this process can be implemented, a value for the received level, RL, must be calculated.

There is one possible cause of error that should be mentioned for completeness. The assumption was made that an iso-velocity sound profile was a reasonable approximation to the medium even though there were available sound velocity profiles taken at the experiment site. To check the effect of the measured sound velocity profiles on propagation over the range from the source to the receiver, ray traces were run on the sound velocity profiles to look for any large deviations from a iso-velocity profile approximation. In all of these comparisons, the amount of refraction in the ray traces was minimal over the range of propagation in the experiment, less than 1 km. This was quantified by looking at the arrival angles of the ray traces compared to those using an iso-velocity approximation. These arrival angles differed by at most several degrees which is comparable to the accuracy of the measured elevation angle and bearing angle for the received line arrays.

5.3 Calculating the Received Level

With the stationarity of the data verified in Section 3.6, the data were processed to arrive at the received level. The average spectrum of a single time series is shown in Figure 5.1. In Figures 5.1 through 5.4, the normalized frequency 0.5 corresponds to 10 KHz because the sampling rate, f_s, was 20 KHz. The time series were multiplied by a complex exponential of the form

$$e^{-j\pi f_0/f_s} \qquad (5.3)$$
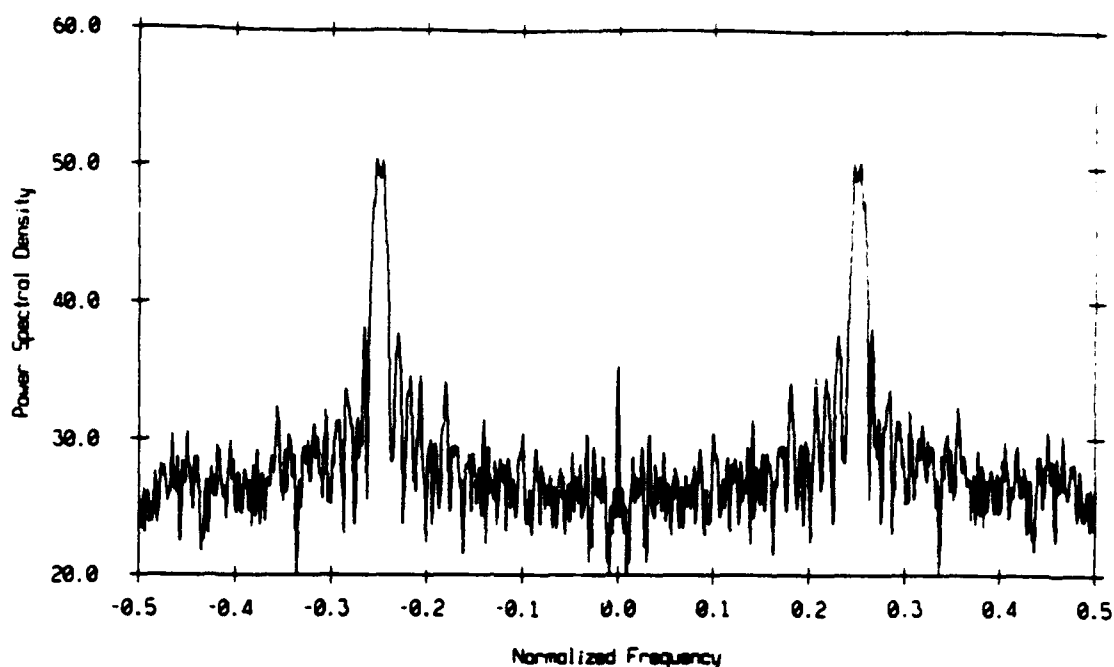
Figure 5.1: Time Series Power Spectra.

so as to shift either the positive or the negative frequency components down to DC, depending upon the sign of the complex exponential. In Equation 5.3, f_o is equal to the intermediate frequency of 5 KHz as discussed in Section 3.5. The spectrum of the basebanded time series is shown in Figure 5.2. Only the energy at DC is desired, so an FIR filter was used to remove the double frequency component. The frequency response of the FIR filter is shown in Figure 5.3 and the filtered spectra is shown in Figure 5.4. The envelope is obtained by taking the magnitude of the complex time series. Since the low pass filter removes approximately half of the power by filtering out the double frequency term, a factor of 3 dB must be added. The factor to convert from digital units to volts is $(409.6)^{-1}$. The gain shown in Table 3.3 is subtracted, and the stave sensitivity applied to convert from voltage
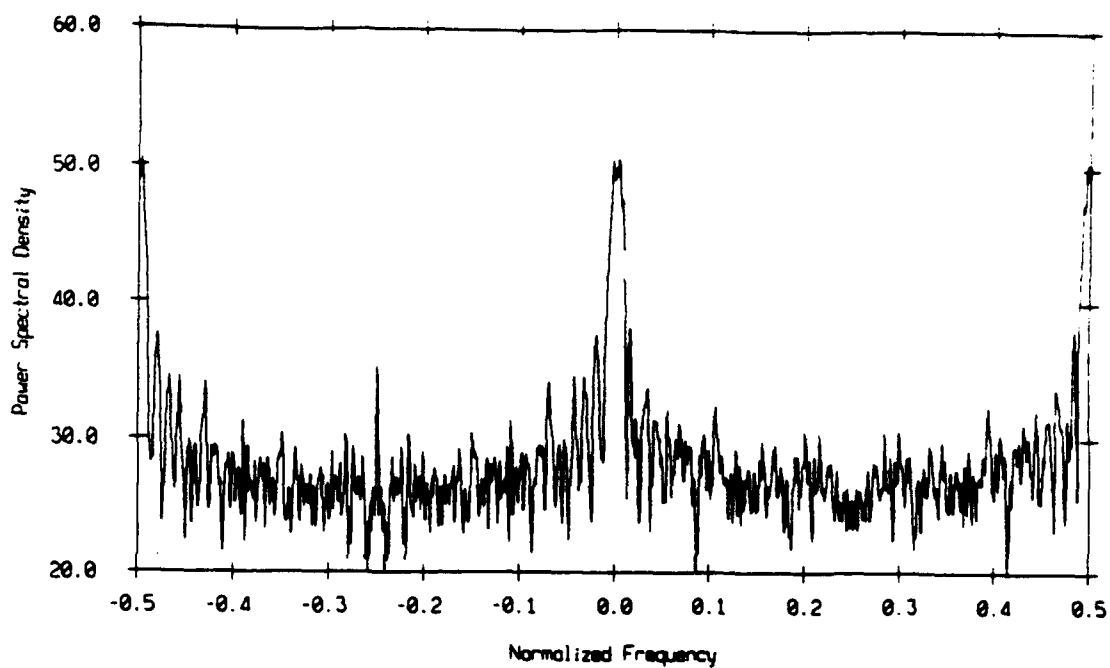
Figure 5.2: Basebanded Time Series Power Spectra.
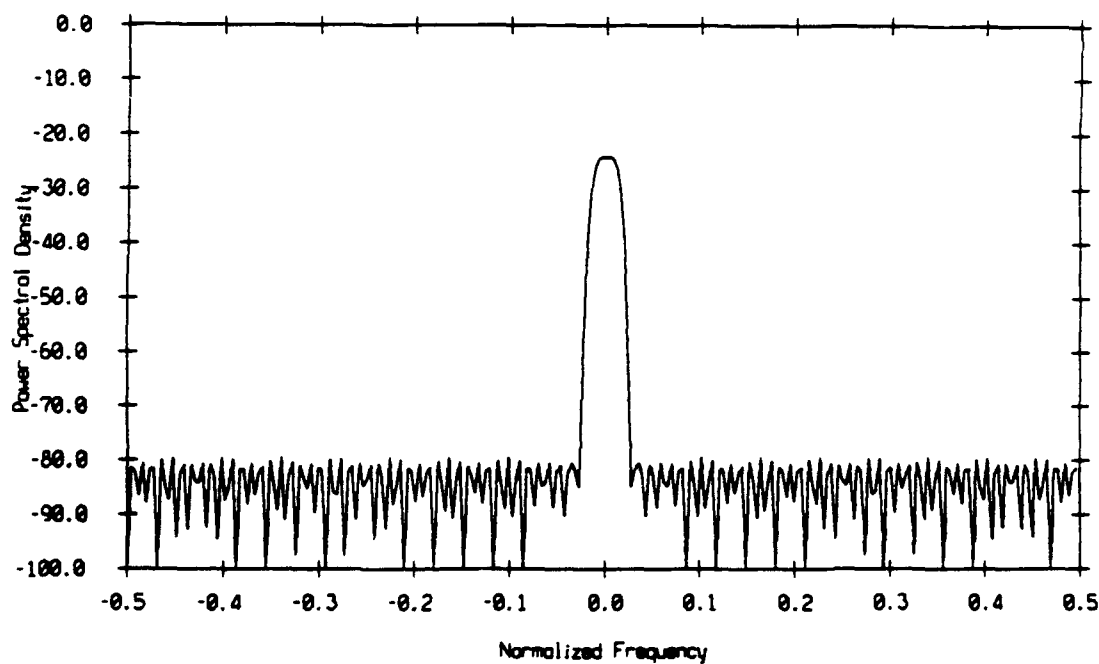
Figure 5.3: Low Pass Filter Transfer Function.
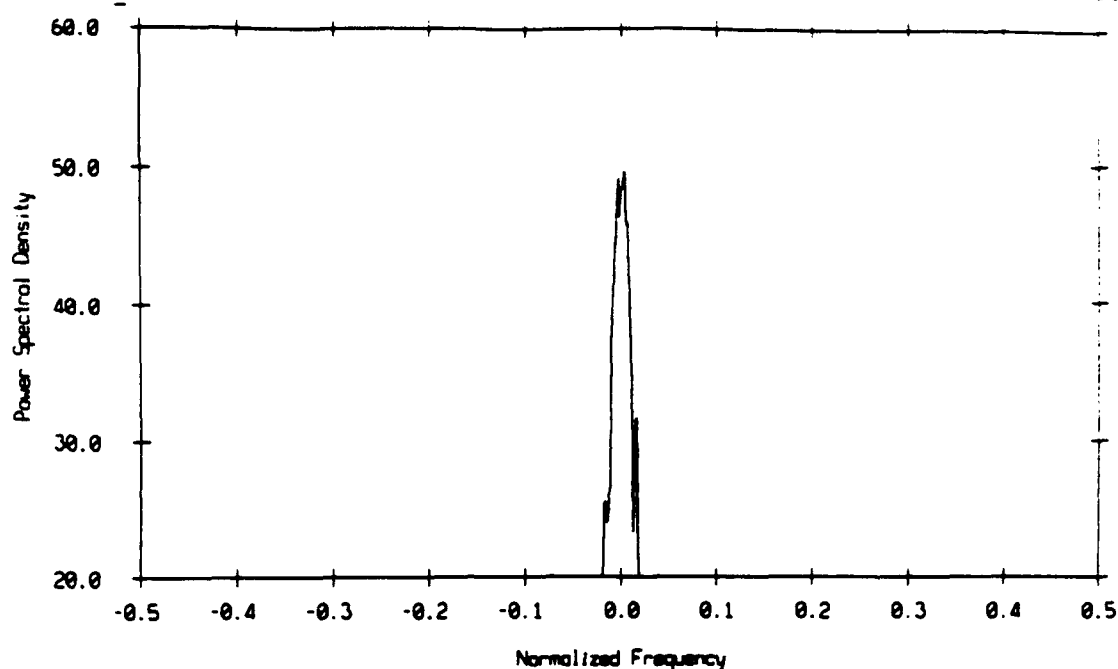
Figure 5.4: Basebanded Low Passed Time Series Power Spectra.

to pressure.

5.4 Estimates of Bistatic Surface Scattering Strengths

Estimates of bistatic surface scattering strengths were calculated for each run. Only time periods during which a single, well-defined scattering patch was found were used. These time periods are shown in Table 5.1.

Scattering strength estimates are shown in Figures 5.5 through 5.13. The incident grazing angle is approximately constant during a run, varying by at most 3°. Individual panels in each figure pertain to a different scattered grazing angle. The bistatic angle is the horizontal axis of each panel, and the scattering strength is the vertical axis. Table 5.2 shows the incident scattering angle, ψ_{inc}, and the range of scattered grazing angles for each figure. Note that for fwd-las.108 and

Table 5.1: Bistatic Surface Scattering Strength Time Periods.

Run	Begin Time (msec)	End Time (msec)
fwd-las.102	715	800
fwd-las.103	724	800
fwd-las.104	719	800
fwd-las.105	718	800
fwd-las.108	539	550
fwd-las.112 (30KHz)	707	750
fwd-las.112 (40KHz)	707	750
fwd-las.116	532	575
fwd-las.117	531	575

Table 5.2: Range of Angles Shown in Bistatic Surface Scattering Strengths.

Run	ψ_{inc}	min ψ_{scat}	max ψ_{scat}
fwd-las.102	9.5	10	30
fwd-las.103	9.5	10	30
fwd-las.104	3.3	20	60
fwd-las.105	3.3	20	70
fwd-las.108	48.5	6	6
fwd-las.112 (30KHz)	9.3	15	35
fwd-las.112 (40KHz)	9.3	15	35
fwd-las.116	18	11.5	11.5
fwd-las.117	12.5	20	40

fwd-las.116 there is only one scattered grazing angle and therefore only one panel in these figures. While the display of this information in panel form for each run may appear to be less than compact, recall that bistatic surface scattering strength depends upon three geometrical parameters, ψ_{inc}, ψ_{scat} and ϕ, as well as wind speed which describes the surface conditions. Any attempt to combine the results into a single, three-dimensional display invariably hides information which must be displayed. In Chapter 6 these plots are again shown with theoretical predictions overlaid, and the efficacy of this display format will be evident.

The most evident trend shown in the estimates of the bistatic surface scattering strength is that, over the narrow range of bistatic and scattered grazing angles for which data are available, the scattering strengths are fairly constant. All but two of the runs, fwd-las.108 and fwd-las.116, have a bearing angle greater than or equal to 55°, which causes most of the usable time periods to have bistatic angles less than −45°. Also, the wind speed is at least 4 m/s for most of the runs, which causes much of the usable data to be dominated by scattering from the sub-surface bubble layer. Derived scattering strengths are roughly independent of bistatic angle because scatter from a sub-surface bubble layer is roughly isotropic.

In the plots of runs fwd-las.104, 105, 112-30KHz and 117, at the largest scattered grazing angle and the smallest bistatic angles, corresponding to the region close to forward scatter, a slight increase in the scattering strength can be seen. Here the effect of surface roughness is becoming dominant over the effect of bubble
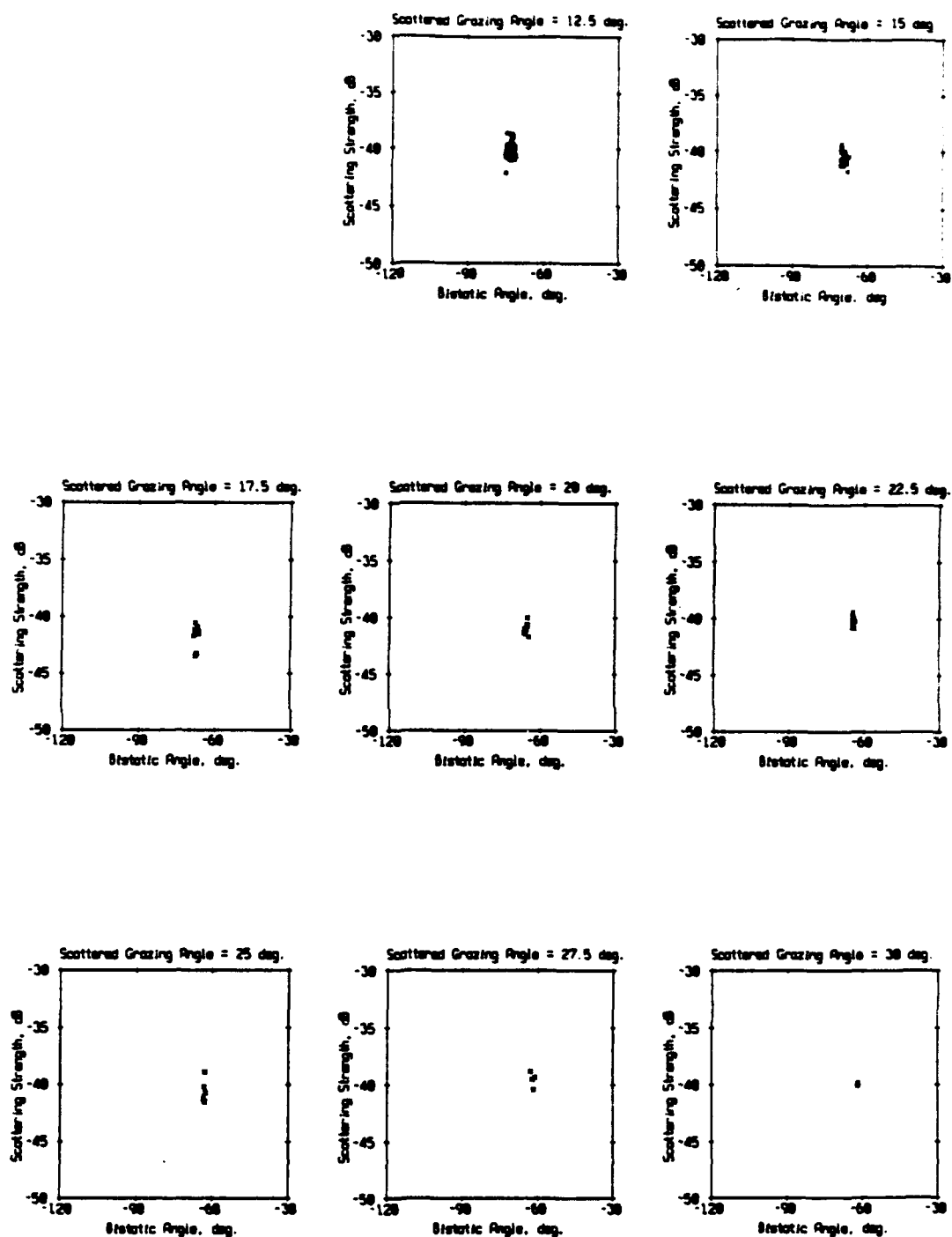
Figure 5.5: Bistatic Surface Scattering Strengths fwd-las.102 (wind speed = 7.2 m/s and $\psi_{inc} = 9.5°$).

Scattered Grazing Angle = 12.5 deg.

Scattered Grazing Angle = 15 deg

Scattering Strength, dB

Bistatic Angle, deg.

Bistatic Angle, deg

Scattered Grazing Angle = 17.5 deg.

Scattered Grazing Angle = 20 deg.

Scattered Grazing Angle = 22.5 deg.

Scattering Strength, dB

Bistatic Angle, deg.

Bistatic Angle, deg.

Bistatic Angle, deg.

Scattered Grazing Angle = 25 deg.

Scattering Strength, dB

Bistatic Angle, deg.
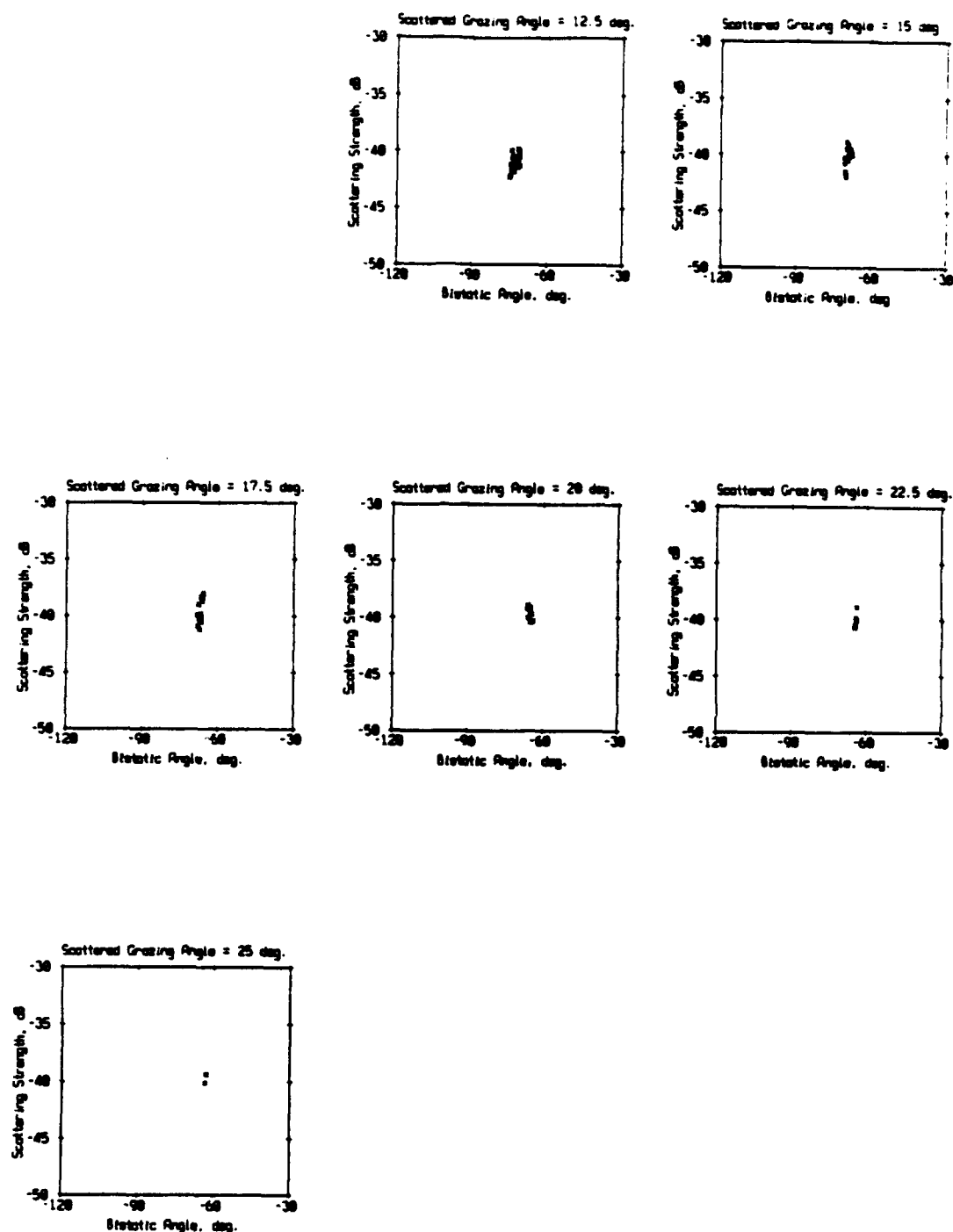
Figure 5.6: Bistatic Surface Scattering Strengths fwd-las.103 (wind speed = 7.2 m/s and $\psi_{inc} = 9.5°$).
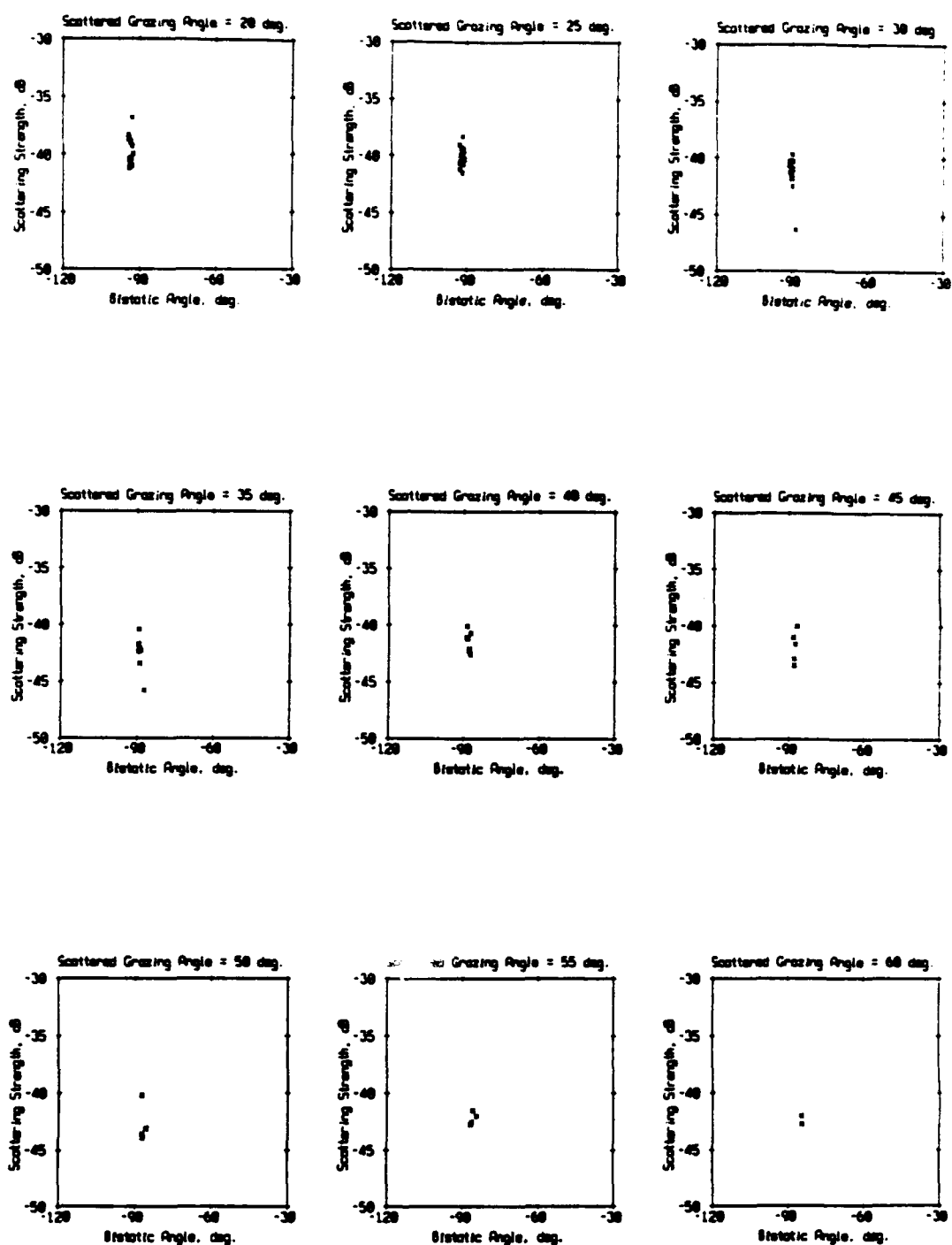
Figure 5.7: Bistatic Surface Scattering Strengths fwd-las.104 (wind speed = 5.5 m/s and $\psi_{inc} = 3.3°$).
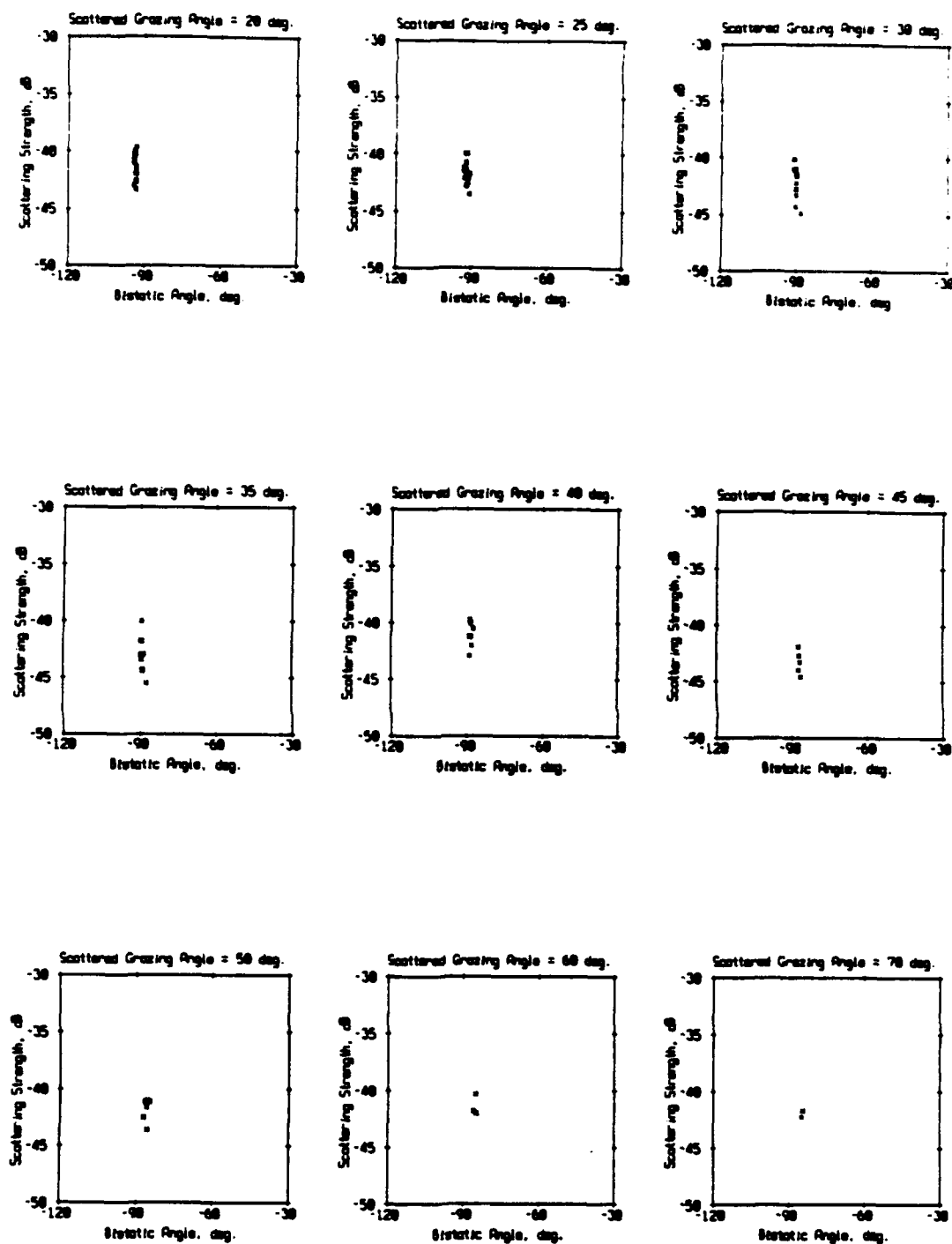
Figure 5.8: Bistatic Surface Scattering Strengths fwd-las.105 (wind speed = 5.8 m/s and $\psi_{inc} = 3.3°$).
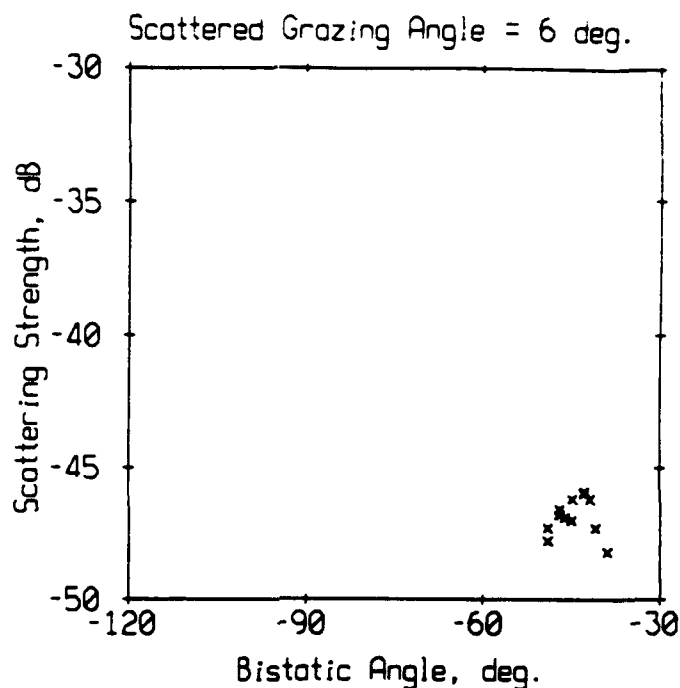
Figure 5.9: Bistatic Surface Scattering Strengths fwd-las.108 (wind speed = 1.4 m/s and ψ_{inc} = 48.5°).

scattering, as will be seen in Chapter 6 when the theoretical predictions are overlaid on the plots shown in this section.

5.5 Summary and Conclusions

The process of estimating bistatic surface scattering strengths began with a test for homogeneity to avoid processing data that was non-stationary. With the data verified as stationary, the magnitude of the complex envelope was calculated using the method described in Section 5.3. The calculation of the bistatic surface scattering strength was done using the sonar equation written in Equation 5.2. The procedure by which the scattering patch area and location was determined is
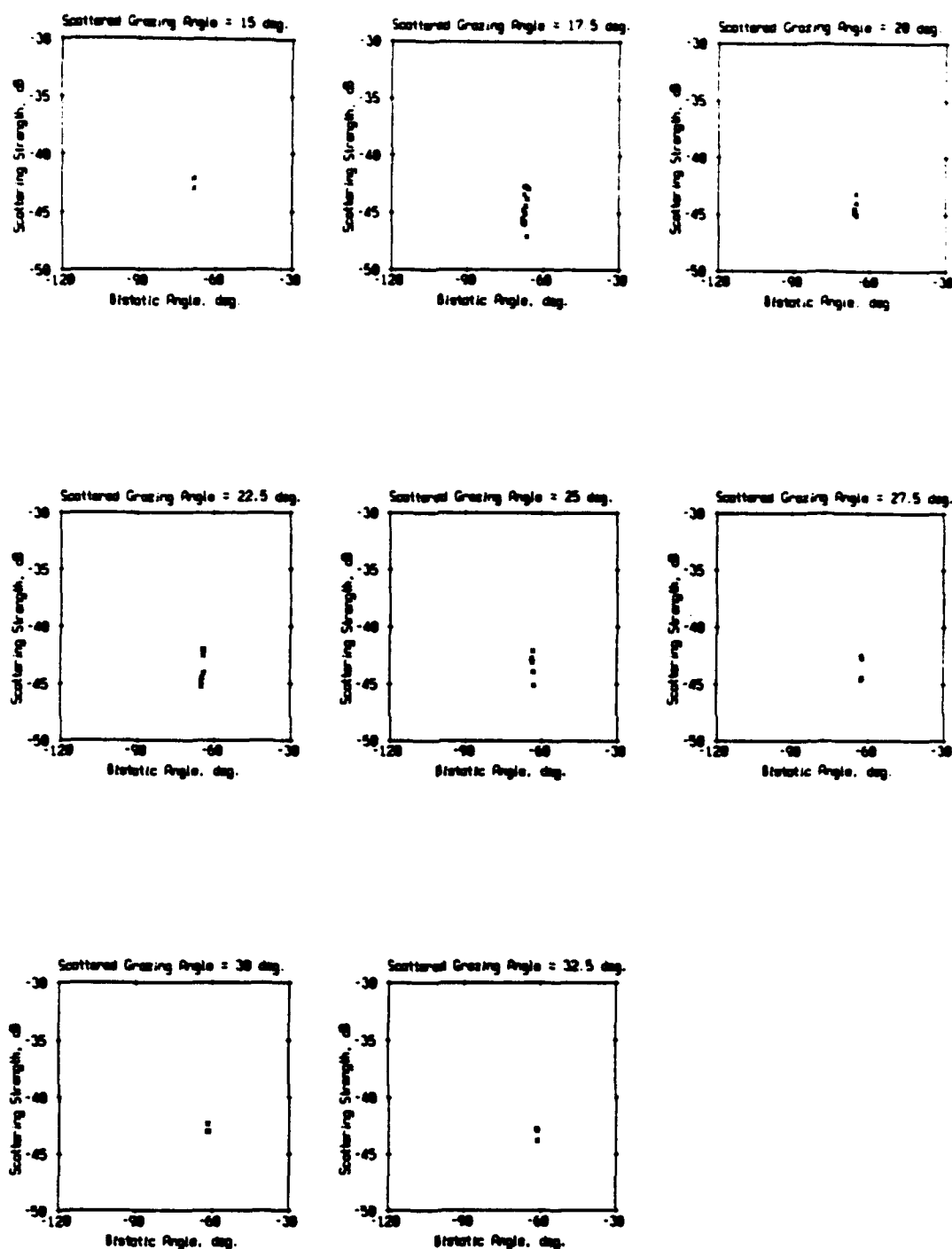
Figure 5.10: Bistatic Surface Scattering Strengths fwd-las.112 (30 KHz) (wind speed = 5.3 m/s and $\psi_{inc} = 9.3°$).
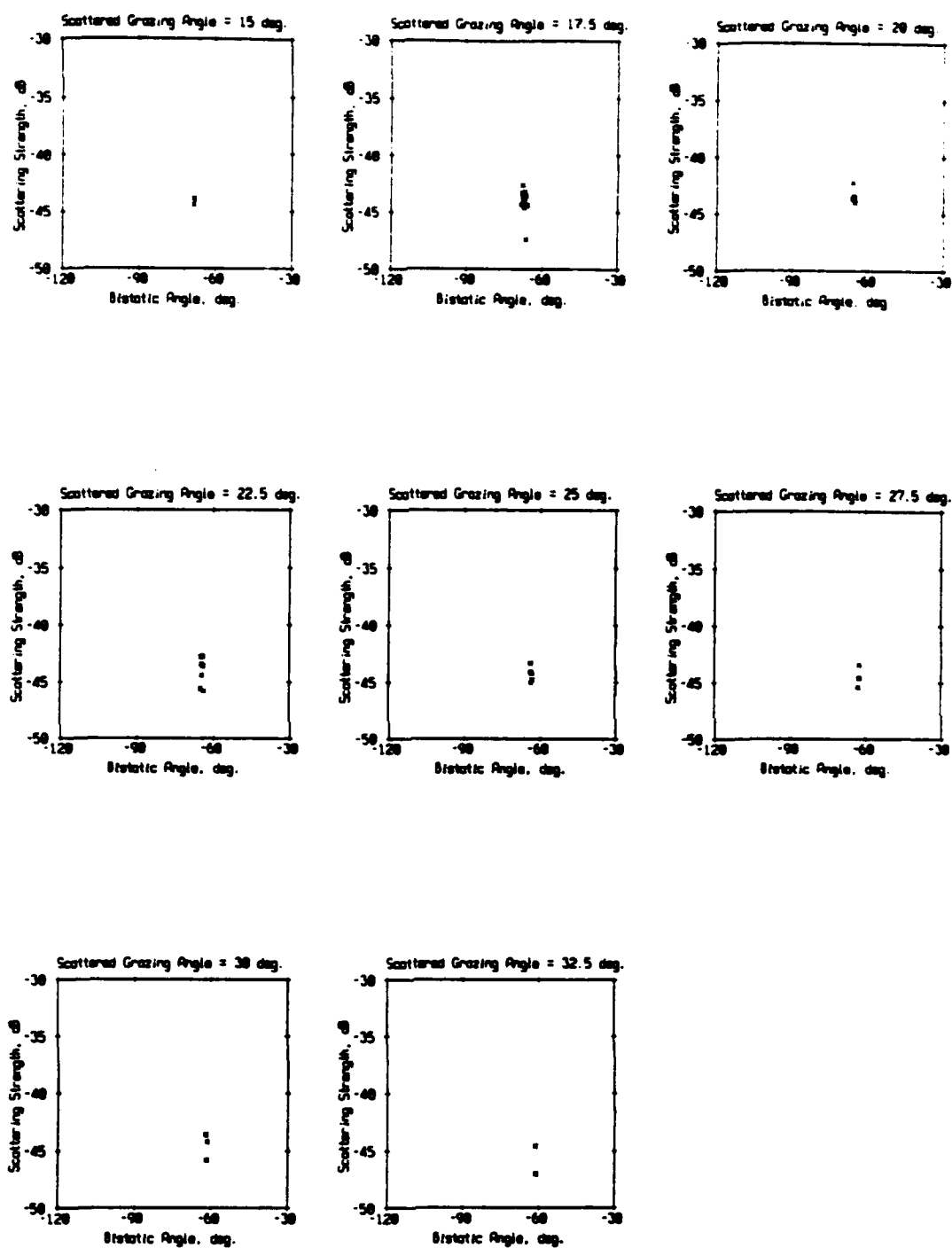
Figure 5.11: Bistatic Surface Scattering Strengths fwd-las.112 (40 KHz) (wind speed = 5.3 m/s and ψ_{inc} = 9.3°).

Scattered Grazing Angle = 11.5 deg.
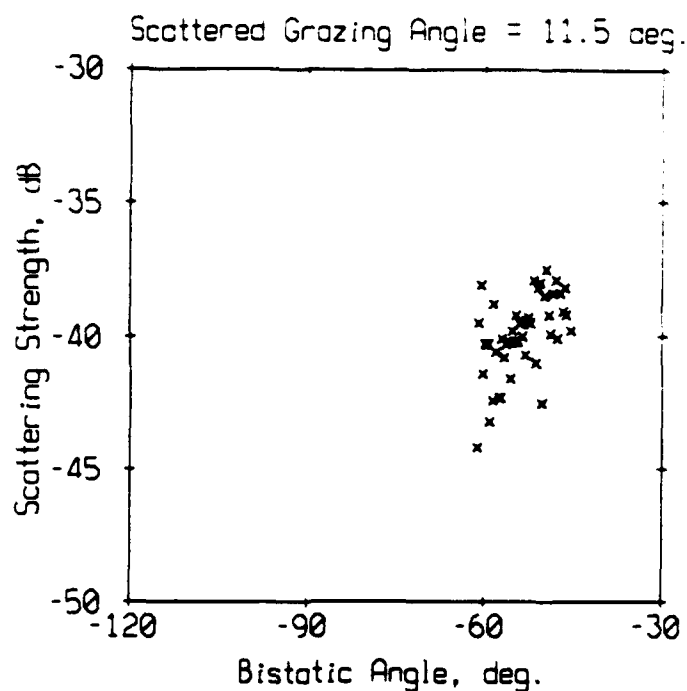
Figure 5.12: Bistatic Surface Scattering Strengths fwd-las.116 (wind speed = 5.3 m/s and $\psi_{inc} = 18.0°$).

explained in Section 5.2, and the computer code is listed in Appendix B. While the code and the method by which it locates the scattering patch may not be elegant, there are a number of checks included to avoid choosing an erroneous location or size for the scattering patch. The horizontal array alone only is used in order to reduce the scattering patch area ambiguity as detailed in Section 3.3.1.

The results show that for the narrow range of values of geometries for which data are available, bistatic scattering strength appears to be roughly independent of all three geometrical parameters. This results from most of the data being dominated by sub-surface bubble scatter, which itself is roughly isotropic.
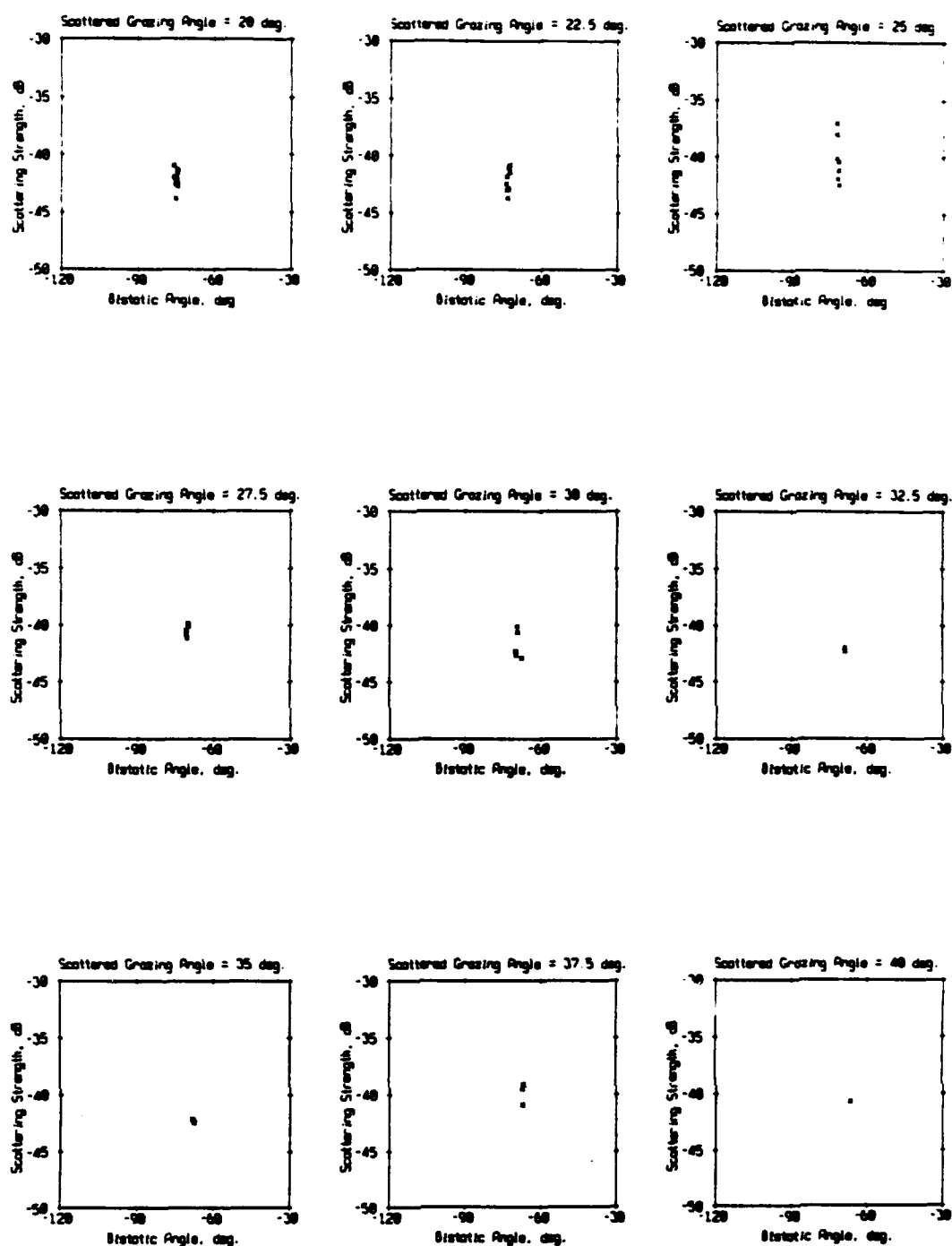
Figure 5.13: Bistatic Surface Scattering Strengths fwd-las.117 (wind speed = 4.9 m/s and $\psi_{inc} = 12.5°$).

Chapter 6

Comparison of Bistatic Surface Scattering Strength Estimates with the McDaniel Model

6.1 Introduction

Bistatic surface scattering strength estimates from the FLIP data are compared with bistatic surface scattering strength predictions made using a theory developed by S.T. McDaniel [15]. The means of comparison with McDaniel's expression was a direct comparison of the bistatic surface scattering strengths shown in Chapter 5 with those predicted by the theory.

6.2 S.T. McDaniel's Expression

The expression for bistatic surface scattering strength developed by S.T. McDaniel [15] models the several effects that may be present in scattering from the ocean surface. They are scattering from the surface itself, which is modeled by the Kirchhoff approximation near specular and by the Rayleigh-Rice approximation far from specular; isotropic scattering from the sub-surface bubble layer; and the attenuation of sound traveling to and from the surface through a sub-surface bubble layer. Section 6.2 is taken wholly from [15] and is discussed here in detail because

[15] may not be easy to obtain.

Scattering from the surface itself is divided into three angular regions:

- near the specular direction (Kirchhoff approximation),

- far from the specular direction (Rayleigh-Rice model),

- a crossover region between the two prior regions (weighted sum of the above).

One can delineate the different geometrical regions by looking at the normalized magnitude of the sum of the horizontal components of the incident and scattered wave number vectors. It is bounded by the relation

$$0 \leq \frac{|\vec{k}_\perp + \vec{k}_\perp{'}|}{|\vec{k}|} \leq \cos \psi_{inc} + \cos \psi_{scat} \qquad (6.1)$$

where $\vec{k}_\perp$ is the horizontal component of the incident wave number vector and $\vec{k}_\perp{'}$ is the horizontal component of the scattered wave number vector. The wave number vectors of the incident and scattered wave are

$$\vec{k} = [-\vec{x}\cos\psi_{inc} + \vec{z}\sin\psi_{inc}]k \qquad (6.2)$$

and

$$\vec{k}' = [\vec{x}\cos\psi_{scat}\cos\phi + \vec{y}\cos\psi_{scat}\sin\phi + \vec{z}\sin\psi_{scat}]k \qquad (6.3)$$

where $k = \omega/c$. The horizontal components are the coefficients of $\vec{x}$ and $\vec{y}$. The normalized magnitude of the sum of the horizontal components can then be expressed

in terms of the angles as

$$\frac{|\vec{k_\perp} + \vec{k_\perp}'|}{|\vec{k}|} = (\cos^2 \psi_{inc} + \cos^2 \psi_{scat} - 2\cos \psi_{inc} \cos \psi_{scat} \cos \phi)^{1/2}. \qquad (6.4)$$

In the specular direction, Equation 6.4 is equal to 0 because $\psi_{inc} = \psi_{scat}$ and ϕ is equal to 0°. In the backscattered direction, Equation 6.4 is equal to $2\cos \psi_{inc}$ because $\psi_{inc} = \psi_{scat}$ and ϕ is equal to 180°.

6.2.1 Near-Specular Scattering

The near specular region can be defined mathematically as

$$0 \le (\cos^2 \psi_{inc} + \cos^2 \psi_{scat} - 2\cos \psi_{inc} \cos \psi_{scat} \cos \phi)^{1/2} \le \psi_1. \qquad (6.5)$$

where ψ_1 must be obtained empirically. In this region, scattering is modeled using the Kirchhoff approximation [13]. The scattering strength can then be expressed as

$$S_A = 10 \log_{10} \left[\frac{< (\vec{n} \cdot \vec{k})^2 >}{4\pi \mu_x \mu_y} \exp \left(\frac{-\alpha^2}{2\mu_x^2} + \frac{-\beta^2}{2\mu_y^2} \right) \right] \qquad (6.6)$$

where α is the x-component of the sum of the incident and scattered wave number vectors

$$\alpha = k(\cos \psi_{scat} \cos \phi - \cos \psi_{inc}), \qquad (6.7)$$

β is the y-component of the sum of the incident and scattered wave number vectors

$$\beta = k \cos \psi_{scat} \sin \phi, \tag{6.8}$$

μ_x is the product of the z-component of the sum of the incident and scattered wave number vectors and the x-component of the large scale rms surface slope, σ_x',

$$\mu_x = k(\sin \psi_{scat} + \sin \psi_{inc})\sigma_x', \tag{6.9}$$

μ_y is the product of the z-component of the sum of the incident and scattered wave number vectors and the y-component of the large scale rms surface slope, σ_y',

$$\mu_y = k(\sin \psi_{scat} + \sin \psi_{inc})\sigma_y', \tag{6.10}$$

and $\vec{n}$ is the outward normal to the surface. The normal to the surface can be approximated in terms of the local surface slopes as

$$\vec{n} \doteq -\vec{z} - \vec{x}\frac{\partial \zeta}{\partial x} - \vec{y}\frac{\partial \zeta}{\partial y} \tag{6.11}$$

where $\partial \zeta/\partial x$ and $\partial \zeta/\partial y$ are the local surface slopes and $\zeta(x,y)$ is the vertical surface displacement. A more physical explanation for the terms in the exponential in Equation 6.6 is that each term is a ratio of the slope at the point (x, y, z) ensonified by the incident wave to the rms surface slope. The exponential in Equation 6.6

can then be thought of as the probability that the surface will be correctly tilted to provide a specular path between the source and the receiver given that the slopes are Gaussian distributed.

At sufficiently high frequency, the large scale surface slope is independent of direction [15] and the slope components can be expressed in terms of the total large scale rms slope σ', i.e.

$$\sigma_x' = \sigma_y' = \sigma'/\sqrt{2}. \tag{6.12}$$

Using the incident wave number vector shown in Equation 6.2 and the normal vector approximation shown in Equation 6.11, the expectation in Equation 6.6 can be evaluated. The mean slopes are 0 and, from Equation 6.12, the second moments are $\sigma'^2/2$. Mathematically, this is

$$< (\frac{\partial \zeta}{\partial x}) > = 0, \tag{6.13}$$

$$< (\frac{\partial \zeta}{\partial y}) > = 0, \tag{6.14}$$

$$< (\frac{\partial \zeta}{\partial x})^2 > = \sigma'^2/2, \tag{6.15}$$

$$< (\frac{\partial \zeta}{\partial y})^2 > = \sigma'^2/2. \tag{6.16}$$

Therefore, the expectation in Equation 6.6 can be written as

$$< (\vec{n} \cdot \vec{k})^2 >= k^2 (\sin^2 \psi_{inc} + \frac{\sigma'^2}{2} \cos^2 \psi_{inc}) \tag{6.17}$$

Defining the angle term in Equation 6.5 to be ψ^2, the scattering strength, S_A, can be expressed as

$$S_A = 10 \log_{10} \left[\frac{2 \sin^2 \psi_{inc} + \sigma'^2 \cos^2 \psi_{inc}}{4\pi (\sin \psi_{inc} + \sin \psi_{scat})^2 \sigma'^2} \exp \left(\frac{-\psi^2}{(\sin \psi_{inc} + \sin \psi_{scat})^2 \sigma'^2} \right) \right] \tag{6.18}$$

in dB/m^2. The method by which σ'^2 is found is described in Section 6.2.6.

6.2.2   Far From Specular Scattering

Now define ψ_2 as the lower bound on the region which is far from specular, which can be modeled using the Rayleigh-Rice approximation [12].

$$\psi_2 \leq (\cos^2 \psi_{inc} + \cos^2 \psi_{scat} - 2 \cos \psi_{inc} \cos \psi_{scat} \cos \phi)^{1/2} \leq 2 \tag{6.19}$$

The value of ψ_2 also must be determined empirically. The scattering strength, S_B, can be expressed as

$$S_B = 10 \log_{10} \left[\frac{< (\vec{n} \cdot \vec{k})^2 (\vec{n} \cdot \vec{k}')^2 > W(\vec{k}_\perp + \vec{k}_\perp')}{\pi} \right] \tag{6.20}$$

in dB/m^2 where W denotes the ocean surface wave number spectrum. The wave number spectrum is omnidirectional for large arguments, so that using Equation 6.4, it can be written as

$$W(\vec{k}_\perp + \vec{k}_\perp\,') = W[k(\cos^2 \psi_{inc} + \cos^2 \psi_{scat} - 2\cos \psi_{inc} \cos \psi_{scat} \cos \phi)^{1/2}]. \quad (6.21)$$

The expectation in Equation 6.20 can be evaluated as in Section 6.2.1 with the additional knowledge that for a Gaussian slope distribution

$$< (\frac{\partial \zeta}{\partial x})^4 > = \frac{3\sigma'^4}{4} \quad (6.22)$$

and the assumption that the slope components are uncorrelated

$$< (\frac{\partial \zeta}{\partial x})(\frac{\partial \zeta}{\partial y}) > = 0. \quad (6.23)$$

The expectation becomes

$$
\begin{aligned}
< (\vec{n} \cdot \vec{k})^2 (\vec{n} \cdot \vec{k}')^2 > \; = \; & k^4 \Big[sin^2 \psi_{inc} \sin^2 \psi_{scat} + \\
& \frac{\sigma'^2 (cos^2 \psi_{scat} \sin^2 \psi_{inc} + \cos^2 \psi_{inc} \sin^2 \psi_{scat})}{2} - \\
& \frac{4\sigma'^2 (\sin \psi_{inc} \cos \psi_{inc} \sin \psi_{scat} \cos \psi_{scat} \cos \phi)}{2} + \\
& \frac{\sigma'^4 \cos^2 \psi_{inc} \cos^2 \psi_{scat} (3\cos^2 \phi + \sin^2 \phi)}{4} \Big].
\end{aligned}
\quad (6.24)
$$

With Equation 6.21 and Equation 6.24, values for S_B can be calculated using Equation 6.20. The method for calculating the surface wave number spectrum is discussed in Section 6.2.6.

6.2.3 Crossover Region Scattering

For the region between ψ_1 and ψ_2, in which neither the Kirchhoff approximation nor the Rayleigh-Rice approximation can be exclusively applied, a weighted sum of the two is used to predict the scattering strength. This crossover region is defined mathematically as

$$\psi_1 \leq (\cos^2 \psi_{inc} + \cos^2 \psi_{scat} - 2\cos \psi_{inc} \cos \psi_{scat} \cos \phi)^{1/2} \leq \psi_2 \qquad (6.25)$$

with $\psi_1 < \psi_2$. Defining the crossover scattering strength as S_C, the weighted sum is written

$$S_C = 10\log_{10}[.4\max(10^{(S_A/10)}, 10^{(S_B/10)}) + .6(10^{(S_A/10)} + 10^{(S_B/10)})] \qquad (6.26)$$

in dB/m^2 where S_A and S_B are defined in Sections 6.2.1 and 6.2.2. These three terms, S_A, S_B, and S_C pertain to the scattering strength of the surface itself. The effect of the near-surface bubble layer is now discussed.

6.2.4 Attenuation Due to the Bubble Layer

Two effects of a sub-surface bubble layer are modeled in S.T. McDaniel's expression, those being attenuation of the incident and scattered rays and scattering of sound by the bubbles.

Attenuation of the incident and scattered ray paths discussed thus far by the bubble layer is modeled as $10 \log(A)$, where A is

$$A = \exp\left[-\left(\frac{Q}{\sin \psi_{inc}} + \frac{Q}{\sin \psi_{scat}}\right)\right] \qquad (6.27)$$

and

$$Q = \frac{2\pi^2 a_r^3 N}{\delta_r}. \qquad (6.28)$$

A_r, expressed, in meters is the resonant bubble radius and is related to frequency by

$$a_r = 3.2/f \qquad (6.29)$$

where f is the transmit frequency in Hz. N is the depth integrated bubble density,

$$N = \int_0^\infty N(z) dz \qquad (6.30)$$

where $N(z)$ is the number of resonant bubbles per unit volume at a depth z. Expressions for N as a function of wind speed and the resonant bubble radius have been developed [14]. The expression for N is also different depending upon whether

the location is in the open ocean or in saline bays/inlets. Significantly higher bubble densities have been found in saline bays and inlets [15]. The reradiation damping constant is $\delta_r = 0.0136$.

The expression in Equation 6.27 is the attenuation at a particular frequency, f, and integrated bubble density, N, which is imparted to the rays which travel to and from the surface. As either the incident or the scattered grazing angle goes to $0°$, implying propagation parallel to the surface, the quantity $10\log(A)$ goes to minus infinity. The scattering strength calculated in Sections 6.2.1, 6.2.2 and 6.2.3 are reduced by a factor of $10\log(A)$ to account for attenuation due to the sub-surface bubble layer.

6.2.5   Scattering Due to Bubble Layer

In addition to the attenuation mechanism due to bubbles described in Section 6.2.4, the sub-surface bubble layer also scatters sound directly. The derivation of the scattering strength due to the bubble layer is simplified by the fact that bubbles scatter isotropically. The scattering strength, in dB, due to the bubble layer is defined to be

$$S_{BUB} = 10\log_{10}(\tilde{A}S^2) \tag{6.31}$$

where $\tilde{A}$ is the attenuation factor and S^2 is the scattering cross section of a resonant bubble of radius a_r.

The attenuation factor is the sum of the attenuations for the four possible

paths from the source to the bubble scatterer and to the receiver:

- path a: direct path from the source to bubble scatterer to the receiver,

- path b: one bounce path from the source to bubble scatterer to the surface and to the receiver,

- path c: one bounce path from the source to the surface to bubble scatterer and to the receiver,

- path d: two bounce path from the source to the surface to bubble scatterer to the surface to the receiver.

Note that the four paths reduce to two paths when the geometry is monostatic. To calculate the bistatic scattering strength due to a bubble scatterer, the contribution and attenuation due to all four paths must be included.

The attenuation losses are expressed in the same form as in Equation 6.27 for each of the four paths. The attenuation for the four paths are denoted by $a_n{}^2 a_m{}^2$ where n and m indicate the path [14]. The attenuation components are:

path a:

$$a_1{}^2 a_3{}^2 = \exp\left[-\left(\frac{Q}{\sin\psi_{inc}} + \frac{Q}{\sin\psi_{scat}}\right)F(z)\right], \qquad (6.32)$$

path b:

$$a_1{}^2 a_4{}^2 = \exp\left[-\left(\frac{Q}{\sin\psi_{inc}} - \frac{Q}{\sin\psi_{scat}}\right)F(z) - \frac{2Q}{\sin\psi_{scat}}\right], \qquad (6.33)$$

path c:

$$a_2{}^2 a_3{}^2 = \exp\left[-\left(\frac{Q}{\sin\psi_{scat}} - \frac{Q}{\sin\psi_{inc}}\right) F(z) - \frac{2Q}{\sin\psi_{inc}}\right], \qquad (6.34)$$

path d:

$$a_2{}^2 a_4{}^2 = \exp\left[\left(\frac{Q}{\sin\psi_{inc}} + \frac{Q}{\sin\psi_{scat}}\right) F(z) - \frac{2Q}{\sin\psi_{scat}} - \frac{2Q}{\sin\psi_{inc}}\right]. \qquad (6.35)$$

Here $F(z)$ is the fraction of bubbles below the depth z, which can be expressed in terms of $N(z)$ by

$$\frac{dF(z)}{dz} = \frac{N(z)}{N} \qquad (6.36)$$

or

$$F(z) = \frac{1}{N} \int_z^\infty N(z')dz'. \qquad (6.37)$$

Using Equations 6.32 through 6.35, the attenuation factor is equal to

$$\tilde{A} = \sum_{n=1}^{2} \sum_{m=3}^{4} \int_0^\infty N(z) a_n{}^2 a_m{}^2 dz. \qquad (6.38)$$

Equation 6.38 can be solved for each term in the summation by substituting $NdF(z)$ for $N(z)dz$. The resulting expression is

$$\tilde{A} = \frac{N}{q + q'}[1 - e^{-2(q+q')}] + \frac{N}{q' - q}[e^{-2q} - e^{-2q'}] \qquad (6.39)$$

where

$$q = \frac{Q}{\sin \psi_{inc}} \tag{6.40}$$

and

$$q' = \frac{Q}{\sin \psi_{scat}} \tag{6.41}$$

and Q is defined in Equation 6.28.

The scattering cross section area of a bubble of radius a_r in the layer is equal to

$$S^2 = \frac{\pi a_r^3}{2\delta} \tag{6.42}$$

where δ is the damping factor, which is related to the reradiation damping constant δ_r by the relation

$$\delta = \delta_r + 3.8 \times 10^{-4} f^{1/2} / Hz^{1/2}. \tag{6.43}$$

Note that the expression shown in Equation 6.42 is for a single scatterer of radius a_r since the expression for the attenuation factor, $\tilde{A}$, was integrated over the entire water column. With the results shown in Equations 6.39 and 6.42, the scattering strength due to the bubble layer, S_{BUB} can be calculated using Equations 6.31, 6.39, and 6.42.

6.2.6 Calculation of Large Scale Surface Slope (σ')

The quantities σ' and $W(K)$ are required in order to calculate the surface scattering strength. The two-dimensional ocean wave height spectra $\tilde{W}(K)$ is

related to the one-dimensional wave height spectra $W(K)$ via the relationship

$$\tilde{W}(K) = K W(K) \qquad (6.44)$$

since the ocean wave height spectrum is assumed to be omnidirectional at high wavenumbers as was discussed in Section 6.2.2. References [21], [22], and [23] contain appropriate models for computing $\tilde{W}(K)$ as a function of wind speed. The large scale rms surface slope σ' can then be calculated using

$$\sigma'^2 \approx \int_0^{K_L} K^2 \tilde{W}(K) dK \qquad (6.45)$$

where a cutoff value of $K_L = 0.4k$ has been found to be satisfactory [15].

6.3 Comparison with Bistatic Surface Scattering Strengths

Comparison of the McDaniel theory predictions with the results presented in Section 5.4 will be done using the same presentation style. The results shown in Figures 5.5 through 5.13 will now be shown with the theory predictions overlaid. An overview of the data presented in this section was given in Table 5.1 and 5.2. The data were described in more detail in Section 5.4.

One preliminary comment is made. The theory prediction is largely dependent on the surface wave height spectrum to describe the surface. The surface wave height spectrum is based upon wind speed. However, the surface must be fully
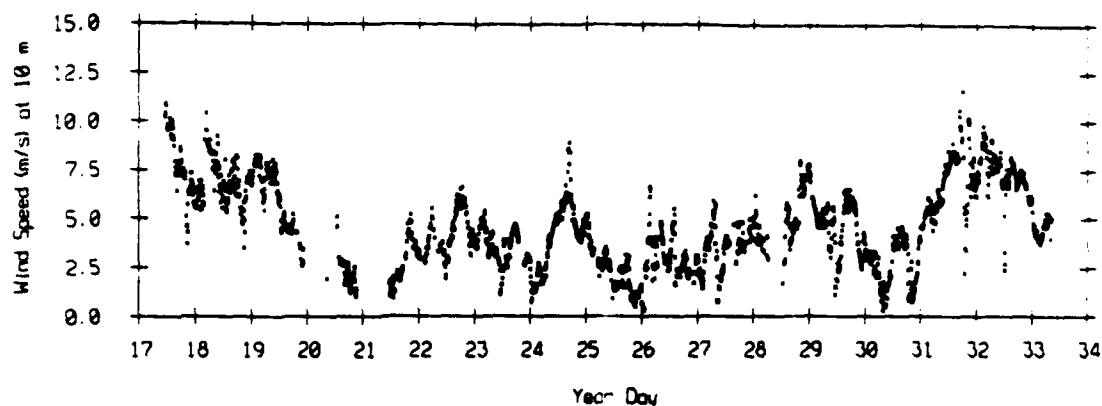
Figure 6.1: Wind Speed as a Function of Time.

developed before the wind speed provides an accurate estimate of the surface wave

height spectrum. To be fully developed requires a sustained period of constant

wind speed from the same direction. This is rarely the case in an ocean environ-

ment, so that the appropriateness of the calculated surface wave height spectrum

is always an open question. Figure 6.1 shows the wind speed as a function of time

during the FLIP experiment, and Figure 6.2, the wind direction. When measured

scattering strengths show significant deviation from the theory prediction, it can

sometimes be explained by variable wind conditions during the time preceding the

measurement.

The predictions of the theory are presented overlaid on the data in Fig-

ures 6.3 through 6.11. This presentation format is chosen to display the variation

of scattering strength with bistatic angle, given that the incident and scattered

grazing angles and all other variables are fixed. The wind speed, frequency and
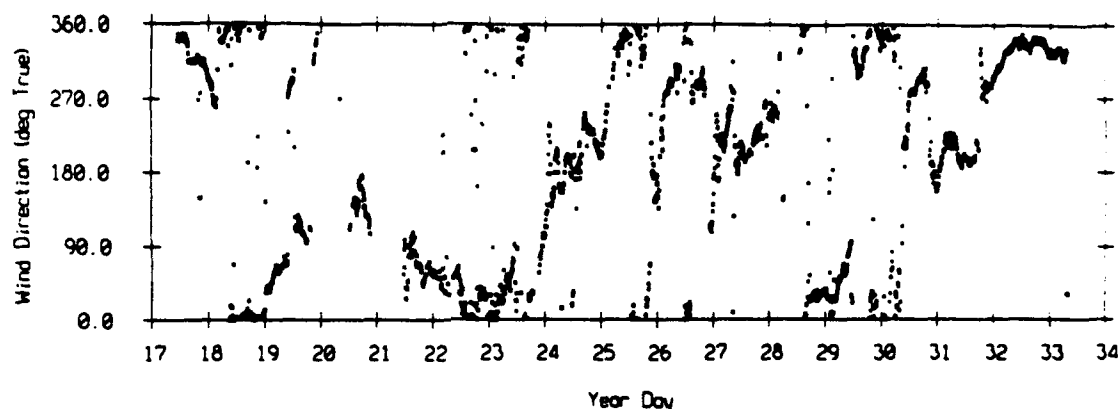
Figure 6.2: Wind Direction as a Function of Time.

incident grazing angle are fixed for each figure or run. Each panel in a figure pertains to a different scattered grazing angle, which translates to a different time after transmit during the run. Two curves for the prediction are shown. The line at a constant value is the scattering strength due to the sub-surface bubble layer. Its constant value with bistatic angle is due to the isotropic nature of scattering from a sub-surface bubble layer. The second curve is a combination of the Kirchhoff approximation and the Rayleigh-Rice approximations as detailed in Sections 6.2.1 through 6.2.3.

Although two curves are presented here, in all cases the theory's prediction for the scattering strength would be the higher curve at a particular bistatic angle. In Figure 6.3 for example, at a scattered grazing angle of 10° (the upper left panel) and bistatic angles from 0° to −25°, the Kirchhoff/Rayleigh-Rice curve is higher and would be used. At bistatic angles from −25° to −180°, the bubble layer curve

would be used. The two curves are both shown for all bistatic angles to illustrate where each mechanism is dominant.

The rate of decrease in the scattering strength prediction with bistatic angle near the $\phi = 0°$ peak increases with decreasing wind speed. The higher the wind speed, the lower and broader the peak will be around a $\phi = 0°$, which corresponds to forward scattering.

The comparisons between runs fwd-las.102 and 103 and the prediction, Figures 6.3 and 6.4, show rms deviations of 4.0 and 3.8 dB, respectively. The wind speed at the time of the measurement, 7.2 m/s, was indicative of the wind speeds on January 17th and the agreement with the theory reflects this. All of the data points fall in the region which the theory predicts to be dominated by bubble layer scattering. A few of the panels contains no data, but the predictions are included for comparison. Runs fwd-las.104 and 105, shown in Figures 6.5 and 6.6, exhibit even better agreement between the data and the predictions, with rms deviations of 2.0 and 1.1 dB respectively. The wind speeds for the two runs, 5.5 m/s and 5.8 m/s respectively, are in the lower range of wind speeds recorded on the day the measurements were made, which may be why the prediction is in general lower than the data. The data in both runs, for the most part, occur in the region which is dominated by bubble scattering. A few points at high scattered grazing angles, $\geq 55°$, are in the crossover region between bubble scattering and Kirchhoff/Rayleigh-Rice scattering. Figure 6.7 shows the comparison for run fwd-
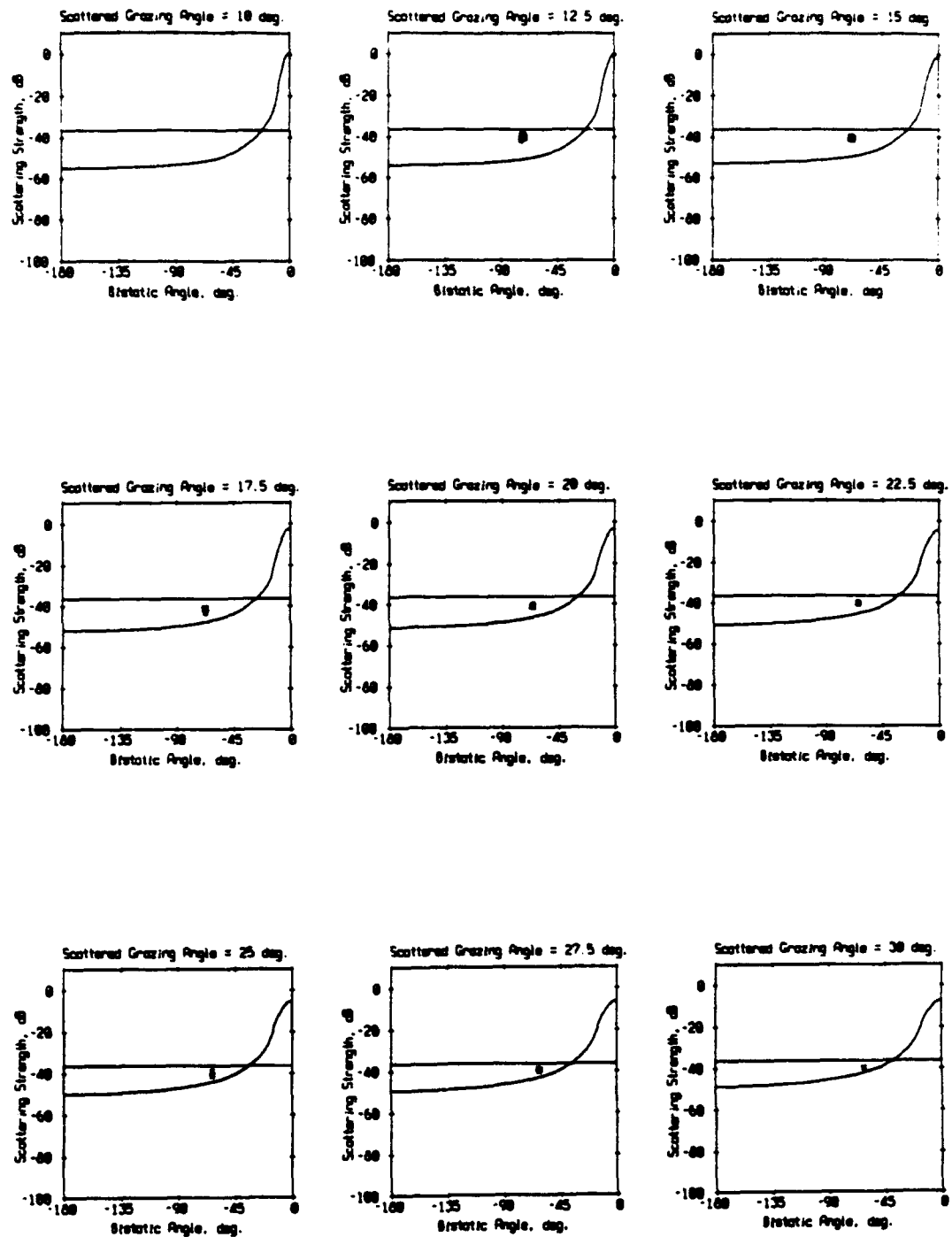
Figure 6.3: Comparison of Bistatic Surface Scattering Strengths with Theoretical Predictions for run fwd-las.102 (wind speed $= 7.2$ m/s and $\psi_{inc} = 9.5°$).
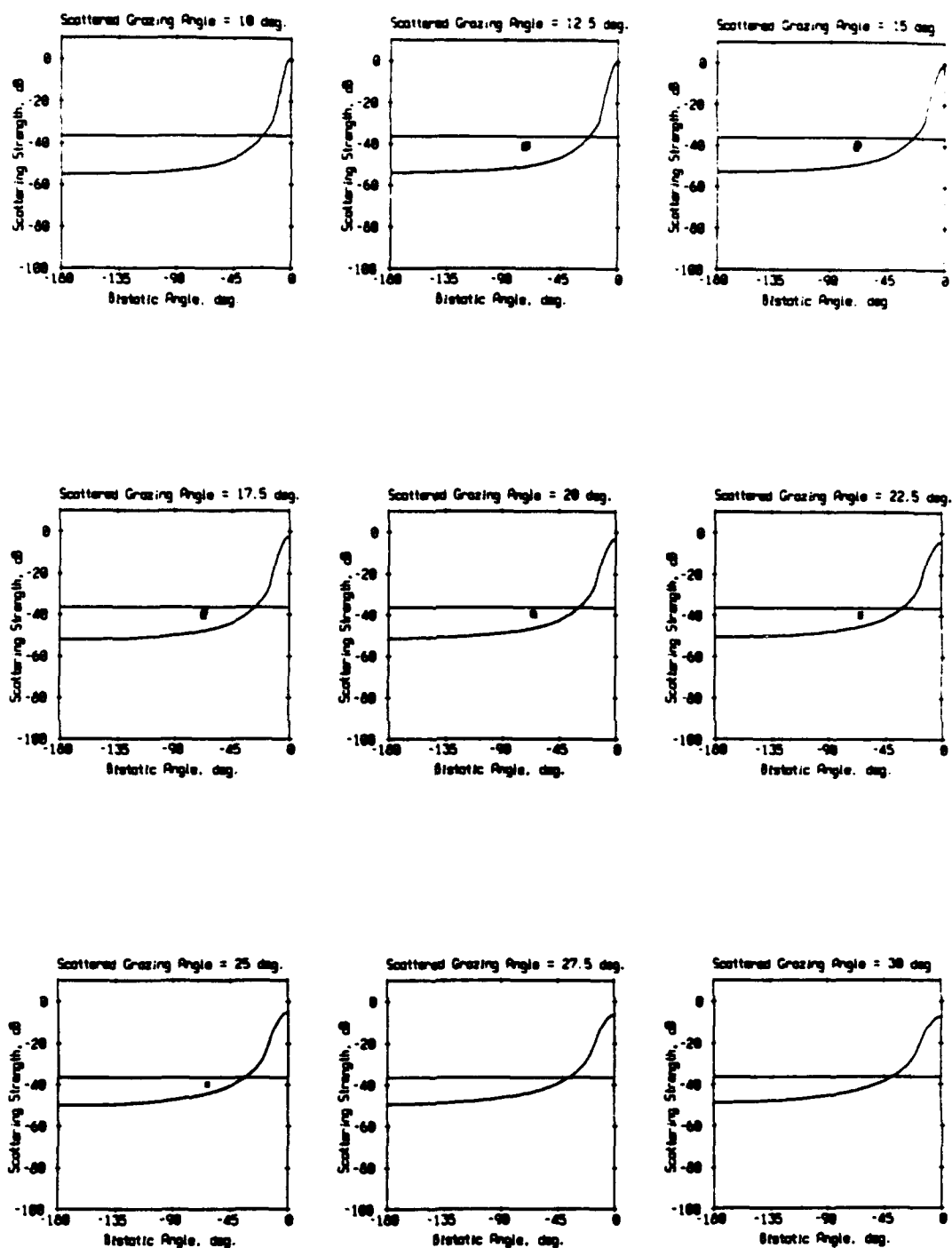
Figure 6.4: Comparison of Bistatic Surface Scattering Strengths with Theoretical Predictions for run fwd-las.103 (wind speed $= 7.2$ m/s and $\psi_{inc} = 9.5°$).
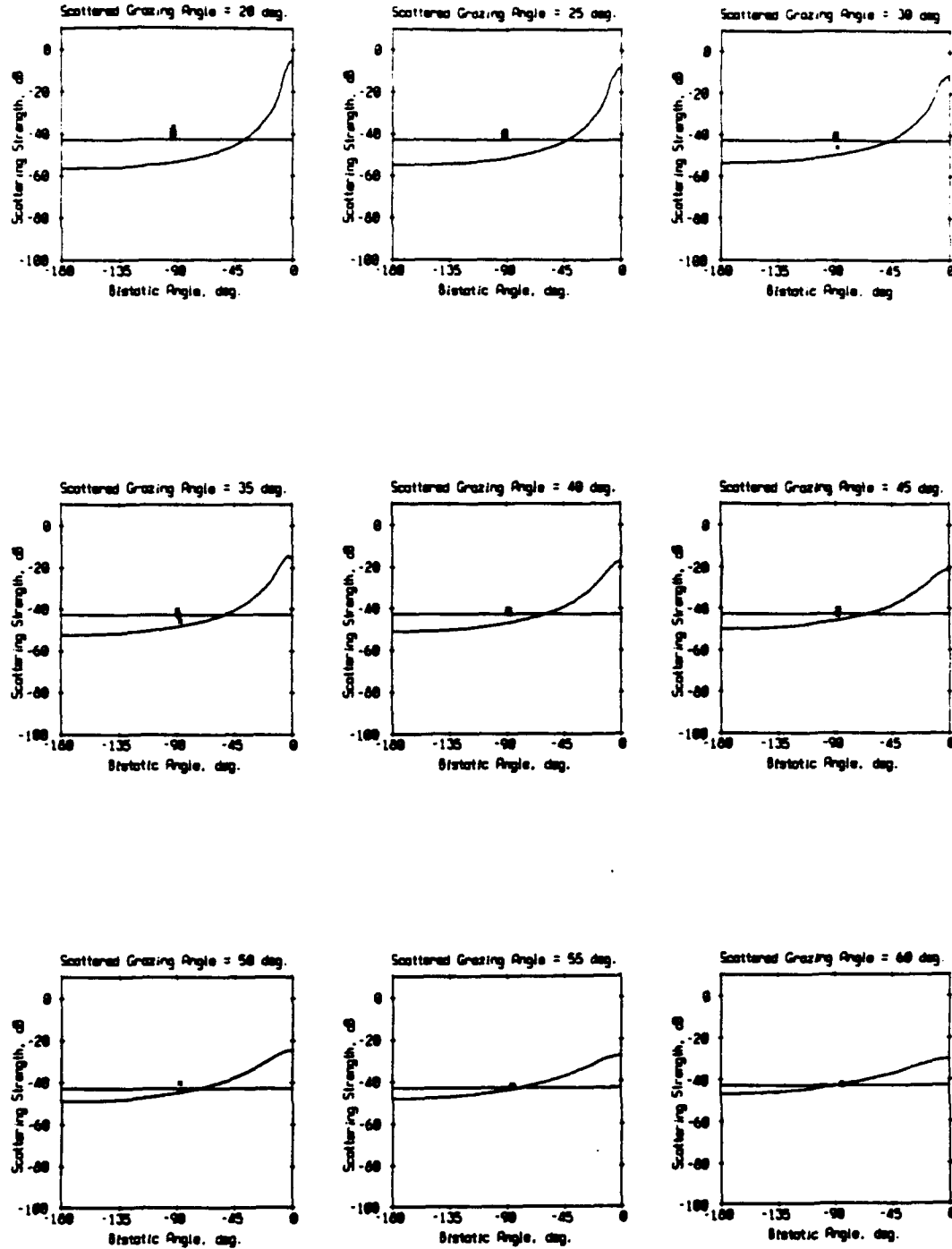
Figure 6.5: Comparison of Bistatic Surface Scattering Strengths with Theoretical Predictions for run fwd-las.104 (wind speed $= 5.5$ m/s and $\psi_{inc} = 3.3°$).
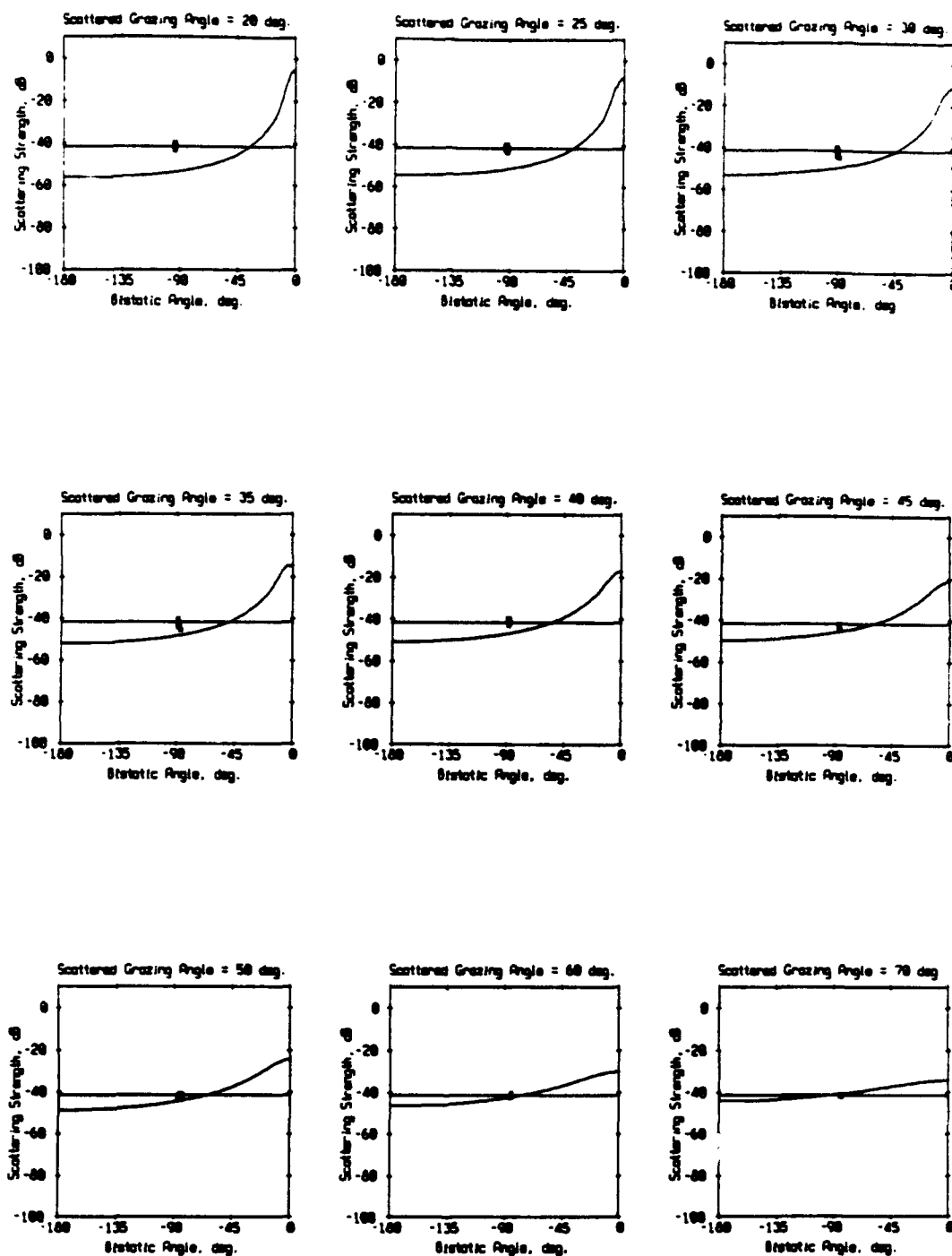
Figure 6.6: Comparison of Bistatic Surface Scattering Strengths with Theoretical Predictions for run fwd-las.105 (wind speed = 5.8 m/s and ψ_{inc} = 3.3°).

Scattered Grazing Angle = 6 deg.
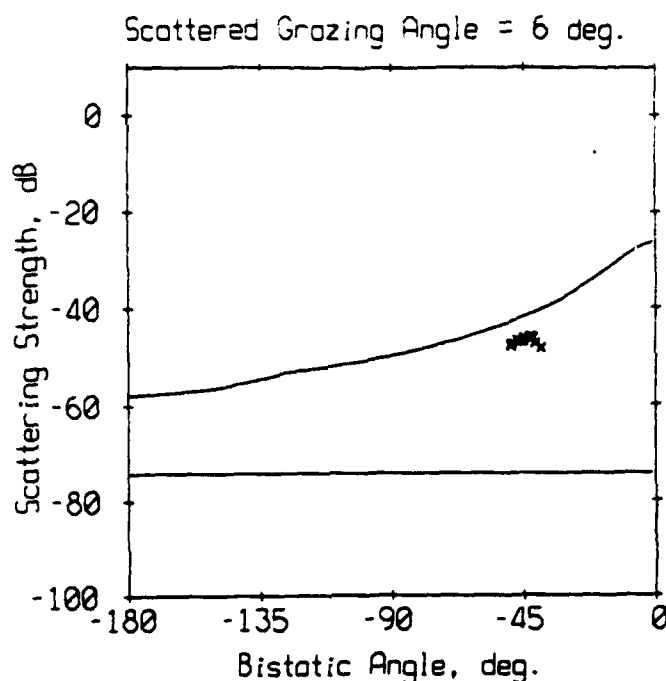
Figure 6.7: Comparison of Bistatic Surface Scattering Strengths with Theoretical Predictions for run fwd-las.108 (wind speed = 1.4 m/s and ψ_{inc} = 48.5°).

las.108, and here the data were dominated by scattering from surface itself. This is a result of the low wind speed, 1.4 m/s, and the receiver bearing of 8°. The data match the theory with an rms deviation of 5.4 dB. The wind speeds on January 21st were quite low, with 1.4 m/s being toward the middle of the range and several measurements as low a 1 m/s. The prediction is higher than the data, perhaps because the sea surface was not a fully developed 1.4 m/s wind driven surface.

The multi-frequency run, fwd-las.112, which occurred at 30 and 40 KHz, displayed some frequency dependence in the scattering strengths. The theory predicts only a slight increase in bubble layer scattering strength as the frequency is increased. At both 30 and 40 KHz the data and the prediction agreed quite well.
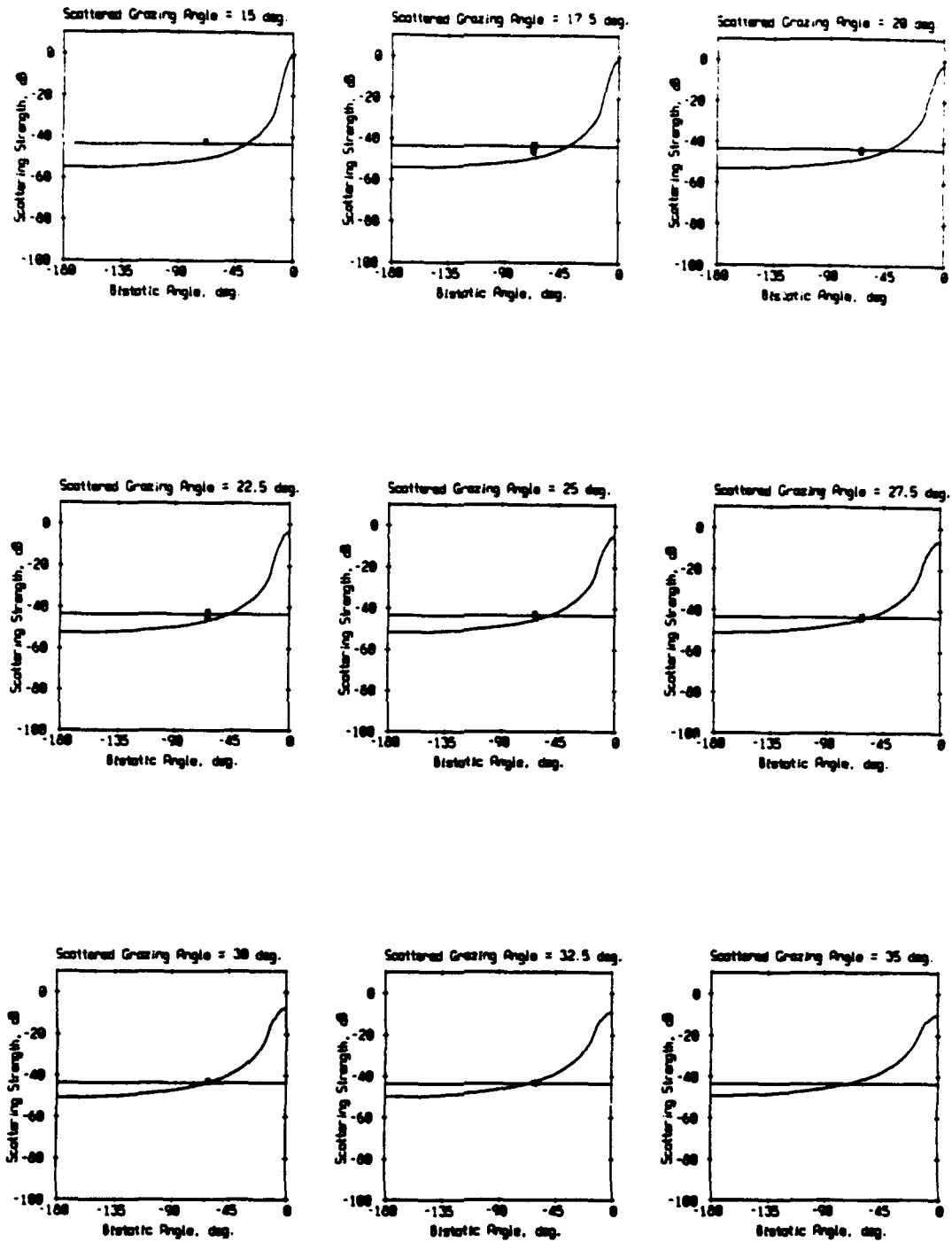
Figure 6.8: Comparison of Bistatic Surface Scattering Strengths with Theoretical Predictions for run fwd-las.112 (30 KHz) (wind speed $= 5.3$ m/s and $\psi_{inc} = 9.3°$).
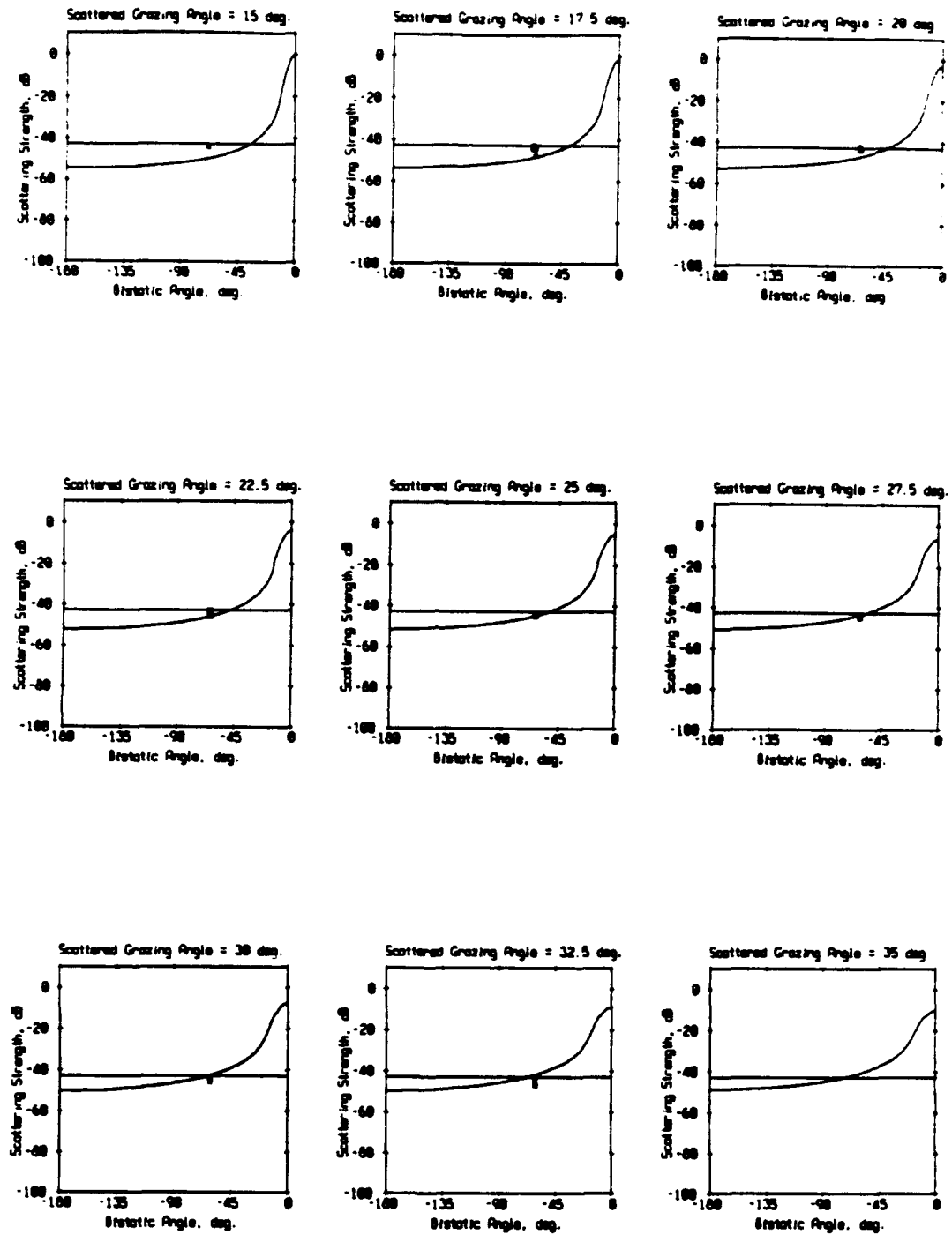
Figure 6.9: Comparison of Bistatic Surface Scattering Strengths with Theoretical Predictions for run fwd-las.112 (40 KHz) (wind speed = 5.3 m/s and ψ_{inc} = 9.3°).

Scattered Grazing Angle = 11.5 deg.
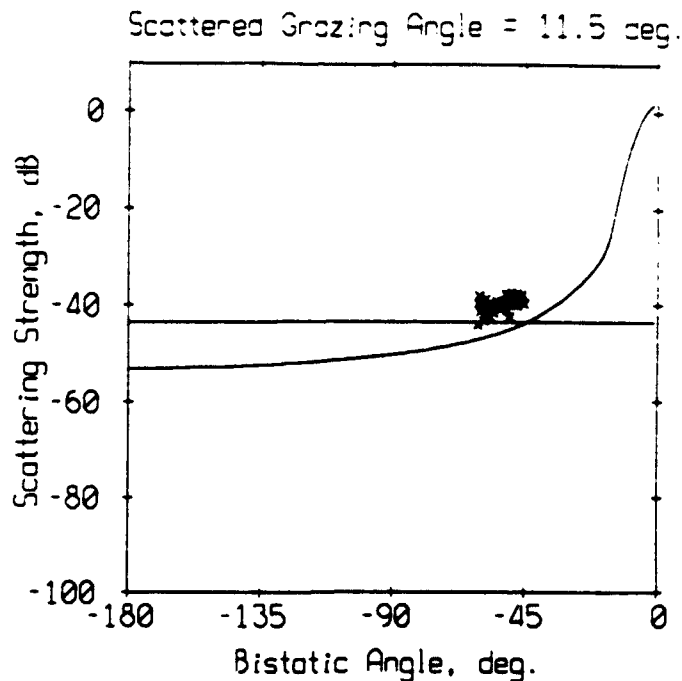
Figure 6.10: Comparison of Bistatic Surface Scattering Strengths with Theoretical Predictions for run fwd-las.116 KHz (wind speed = 5.3 m/s and ψ_{inc} = 18.0°).

The comparison for run fwd-las.116 shows good agreement, with 3.6 dB rms deviation between the data and the theory. Figure 6.10 is similar to Figure 6.7, with only one panel showing an incident grazing angle of 18° and a scattered grazing angle of 11.5°. The data are clustered in a region which the theory predicts to be dominated by bubble layer scattering, and the relatively constant value of the data for small changes in bistatic angle is consistent with the theory. Run fwd-las.117 shows good agreement between the data and the theory. Data are available for the regions dominated by bubble layer scattering, $20.0 \leq \psi_{scat} \leq 25.0$, and by surface roughness, $27.5 \leq \psi_{scat} \leq 40.0$. Both fwd-las.116 and 117 were taken within 15 minutes of each other (see Table 3.4 for exact times). The bearing angle was 30°

Table 6.1: RMS Deviations between the Model and the Data.

Run	RMS Deviation (dB)
fwd-las.102	4.0
fwd-las.103	3.8
fwd-las.104	2.0
fwd-las.105	1.1
fwd-las.108	5.4
fwd-las.112 (30KHz)	1.1
fwd-las.112 (40KHz)	1.6
fwd-las.116	3.6
fwd-las.117	2.9

for fwd-las.116 and 60° for fwd-las.117, giving a different set of grazing angles and bistatic angles. Table 6.1 summarizes the rms deviations between the theory and the data for all the runs.

6.4 Conclusions

Direct comparison of bistatic scattering strength estimates derived from FLIP data with predictions by the McDaniel theory showed good agreement over a range of geometries and wind speeds. The theory's predictions for bubble scattering appear to be valid over the ranges shown below:

- $-105° \leq \phi \leq -35°$,

- $3.3° \leq \psi_{inc} \leq 18°$,

- $6° \leq \psi_{scat} \leq 40°$,
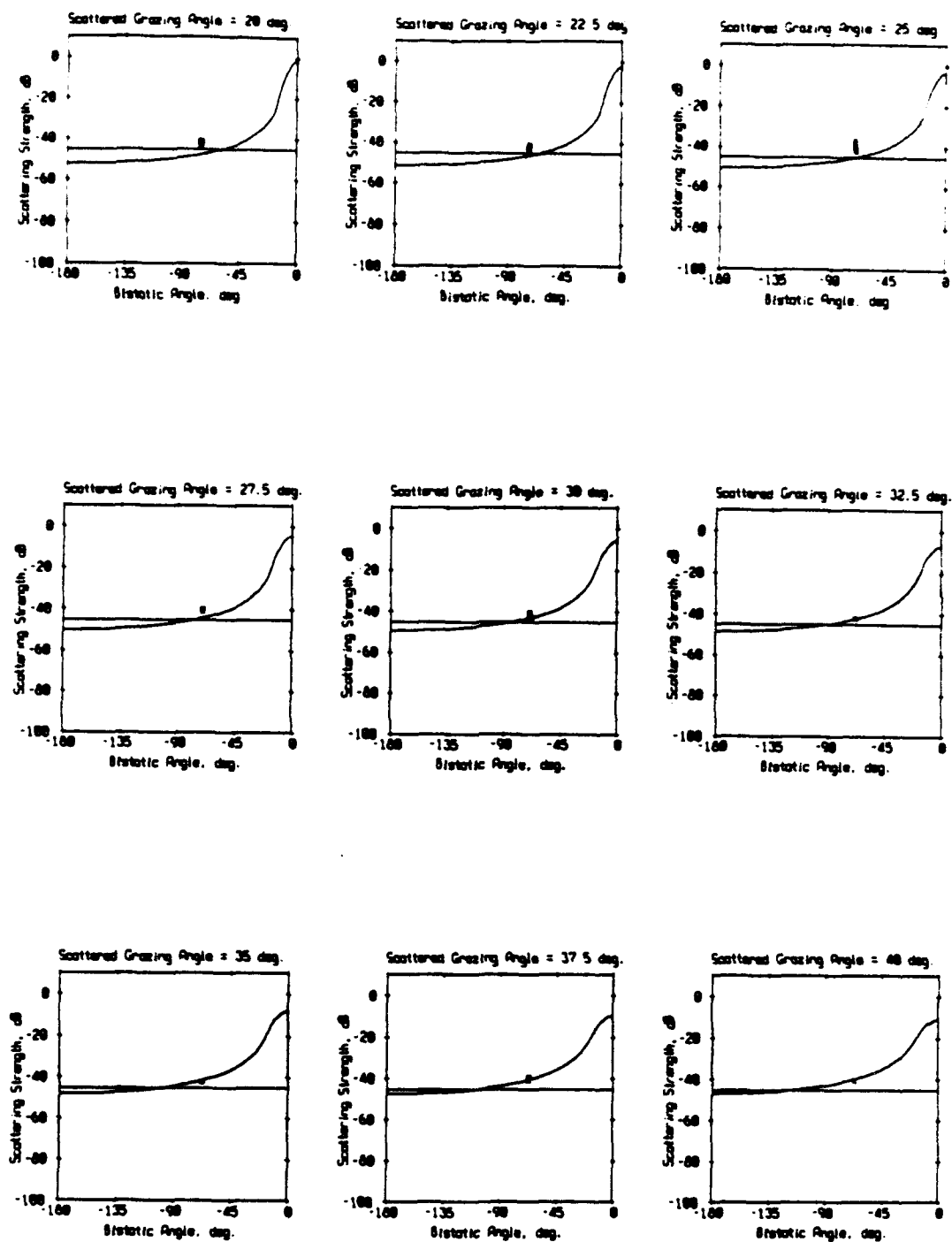
Figure 6.11: Comparison of Bistatic Surface Scattering Strengths with Theoretical Predictions for run fwd-las.117 KHz (wind speed = 4.9 m/s and ψ_{inc} = 12.5°).

- 1.4 m/s $\leq$ wind speed $\leq$ 7.2 m/s,

- $f = 30, 40$ KHz.

This is an important result because it represents the first such validation of the McDaniel model prediction.

Some of the poorer comparisons may be due to an improper wind speed used to characterize the surface conditions. The theory predicts a slight increase in bubble scattering strength with frequency over the 30 KHz to 40 KHz range. The 30 KHz and 40 KHz data display this very slight trend and match the theory well.

Chapter 7

Summary and Conclusions

7.1 Introduction

The major goal of the research presented in this thesis was to analyze the statistical characteristics of bistatic surface scattering data collected during the FLIP experiment of January 1992, and to compare bistatic scattering strength estimates to the McDaniel prediction model. The original contributions presented in this thesis are as follows.

- The ocean surface scatter data were histogrammed and their cumulative distribution function compared with a Rayleigh distribution using the probability of false alarm, P_{FA}. Theory predicts that the dominant surface scattering mechanism is the slope of surface for higher grazing angles and isotropic resonant bubble scatter at lower grazing angles and higher wind speeds. The magnitude of the complex envelope of the ocean surface scatter data was found to be Rayleigh for both mechanisms and for all but the highest wind speed (7.2 m/s). This result shows that the use of the central limit theorem to describe the statistical characteristics of bistatic surface scatter is valid over the geometries and wind speeds, except 7.2 m/s, studied here. It also shows that the

central limit theorem is valid for both scattering mechanisms, surface roughness and the bubble layer, for the geometries and all but the highest wind speed studied here.

- Mean bistatic surface scattering strength was calculated using the sonar equation and compared to a prediction by S.T. McDaniel's theory for bistatic surface scattering strengths [15]. The portion of the theory for predicting scattering strengths dominated by bubble scattering was validated by the data for a number of geometries. This is the first validation of that portion of the theory.

- A technique was developed for combining ocean surface scatter data for different grazing angles which increased the number of data points in the ensemble. With this technique, data which were the result of the same dominant scattering mechanism, the surface itself or the sub-surface bubble layer, were combined to estimate the statistical characteristics of the scattering mechanism.

A more detailed description of these contributions follows.

7.2 Statistical Characteristics of the Data

The statistical testing was comprised of tests for homogeneity, normality and for Rayleigh behavior. Homogeneity was investigated using the Kolmogorov-Smirnov two sample test, in which the statistics of the first half of an ensemble are compared with those of the second half. All usable data were found to be statistically stationary. Testing for homogeneity is a necessary first step in the data

analysis since a change in the underlying statistical characteristics during a particular run (or ensemble) would indicate a meaningful change in the environment during the run. In this case, one can no longer assume that the statistical characteristics of the entire ensemble come from the same parent distribution, rendering the ensemble invalid. If the data are validated as homogeneous, then one can treat each return in the run as an independent realization of the reverberant process.

The surface scatter time series were tested for normality using the two sample Kolmogorov-Smirnov test, in which the cumulative distribution of the data is compared to that of a Gaussian. All of the data passed the K-S test for normality. However, deviations from normality in surface scatter reverberation are of most interest in the tails of the distribution, and the limited number of the pulses (25 to 50) made such deviations unobservable. Also, the usefulness of the K-S test to identify non-normal behavior in the tails of the distribution is questionable.

In order to increase the number of samples used in the test for normality, data which were a result of the same dominant scattering mechanism were normalized and grouped together into a single ensemble. This combinational method, which is described in Section 4.3, increased the amount of data in all runs by at least a factor of five, resulting in better definition of the distribution. The longer ensembles were tested for normality by comparing the statistics of their magnitude to a Rayleigh distribution, since theory predicts that the magnitude of a complex Gaussian time series will be Rayleigh distributed. The comparison was made using

the probability of false alarm, P_{FA}, which is one minus the cumulative distribution, in order to focus on the largest excursions of the time series which define the shape of the distribution tail. The P_{FA} comparison showed some deviation from Rayleigh behavior for all runs. However, only at the highest wind speeds of 7.2 m/s were the deviations from Rayleigh behavior significant. While apparentl ufficient to fail the Kolmogorov-Smirnov test, the deviations do indicate that at higher wind speeds, the distribution tails are higher than those of a Gaussian distribution.

7.3 Bistatic Surface Scattering Strengths

The FLIP bistatic data were processed to yield estimates of bistatic surface scattering strength using a rather inelegant method of processing as detailed in Section 5.2. An isovelocity sound speed profile was used because ray tracing was unnecessary. The scattering strength estimates are shown in Figures 5.5 through 5.13 as a function of scattered grazing angle, ψ_{scat}, and bistatic angle ϕ, for each run, which in turn determines wind speed and incident grazing angle, ψ_{inc}. No satisfactory means exists to combine data for different geometrical parameters. The majority of the results are dominated by bubble scattering, as can be seen by the their very weak dependence on bistatic angle. This characteristic is due to the isotropic nature of scatter from bubbles.

7.4 Comparison of Scattering Strength Estimates with the McDaniel Prediction Model

Bistatic surface scattering strength estimates were compared with predications of a theory developed by S.T. McDaniel, which is presented in Section 6.2. The theory consists of two main parts, one modeling scattering from the surface itself and one modeling scattering from a sub-surface bubble layer. Scattering from the surface is modeled by either one or a combination of the Kirchhoff approximation and the Rayleigh-Rice approximation. Attenuation by the sub-surface bubble layer of scattering from the surface is included. Scattering from a sub-surface bubble layer is modeled as the product of the scattering cross section of a bubble resonant at the incident frequency and the depth integrated attenuation factor. The depth integrated attenuation factor accounts for four paths from the source to the scattering bubble and on to the receiver, and for the bubble density integrated over the entire water column.

The comparisons between the data and the theory showed good agreement, with a rms deviation of about 3 dB for all the data. Some of the poorer agreements may be a result of the wind speed being much higher or lower during the period prior to the run, inasmuch as the theory uses wind speed to calculate a wave height spectrum which has a strong effect on the prediction. In order for this to be an accurate and valid method, the wind speed must have been fairly constant in speed and direction for some time.

7.5 Recommendations for Future Research

Any future experiment to measure bistatic surface scattering would benefit by using a horizontal array only to receive data and recording each hydrophone rather than only the staves. This would increase the range of angles, ψ_{inc}, ψ_{scat} and ϕ, for which statistics could be generated, since the beam could be steered over a range of bearing angles instead of just looking perpendicular to the array axis as was done with the data collected in January of 1992.

From an analysis point of view, the ability to steer the receive beam would permit a single run to provide estimates of the bistatic surface scattering strength over a large range of bearing angles instead of just a few. Two or three runs at bearing angles of 15°, 45° and 75° could provide data for all bearing angles from 0° to 90°. This would permit the study of some of the more subtle angular dependences of bistatic surface scattering strength. While more computationally intensive, this would permit a more detailed analysis of bistatic surface scattering strengths as a function of geometry.

Element level data would also enhance the statistical study of the bistatic surface scatter since beam steering could be used to look at the surface in directions that may generate non-Gaussian scatter. Perhaps a clearer understanding of the transition of bistatic surface scatter from Gaussian behavior to non-Gaussian behavior would emerge. Increasing the number of pulses transmitted in a run would also increase the accuracy of the statistical analysis, but one must be wary

of non-stationarity when the duration of the runs is increased.

Appendix A

Fundamentals of Monostatic and Bistatic Active Sonar

Boundary Scatter

In order to understand the geometry of a bistatic active sonar boundary scatter, one should begin with the simpler case of a monostatic active sonar. Assuming an isovelocity, range-independent sound profile, propagation occurs in a straight line.

For a monostatic sonar, where the source and receiver are collocated, and with a relatively short transmit pulse and no boundary interaction, the ensonified volume at any particular time is a spherical shell, the radius of which is determined by the elapsed time since pulse transmission, and the thickness of which is determined by the transmit pulse duration. This implies that at a particular listen time, only volume inhomogeneities and scatterers located in this shell will contribute to the return seen at the receiver.

In the case where the pulse interacts with a boundary, such as the ocean bottom or surface, the spherical shell is cut by a plane, yielding an annular ring on the boundary which contributes to the return at particular listen time. If the received signal is dominated by the interaction with the boundary, one can ignore the contribution from the volume. An example of boundary interaction is shown in
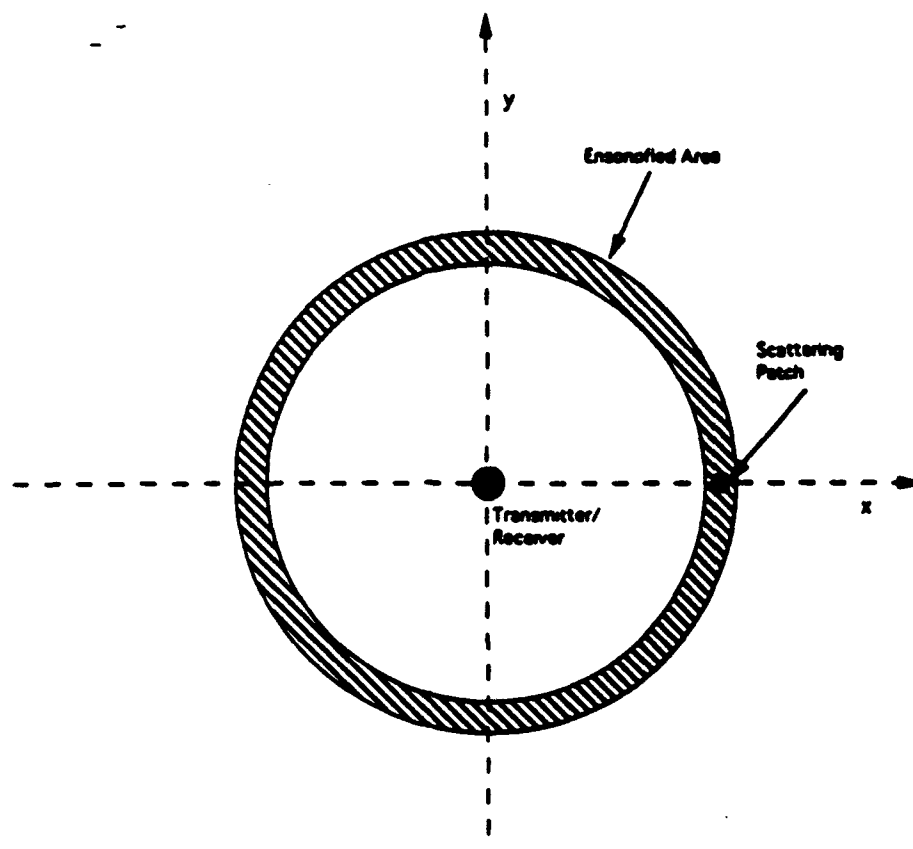
Figure A.1: Overhead View of Monostatic Geometry.

Figure A.1. We further define the scattering patch to be the part of the ensonified area whose contribution to the return is within 3 dB of the maximum return produced by any point. The directionality of the source and receiver determine what portion(s) of the ensonified area compromises the scattering patch. When both the source and the receiver are omnidirectional, the scattering patch is composed of the entire ensonified area. If the source or the receiver or both have some directionality, the scattering patch will be some smaller portion(s) of the ensonified area. Such a scattering patch is shown in Figure A.1 by the small square on the x-axis. Figure A.2 shows a side view of the monostatic geometry in order to define
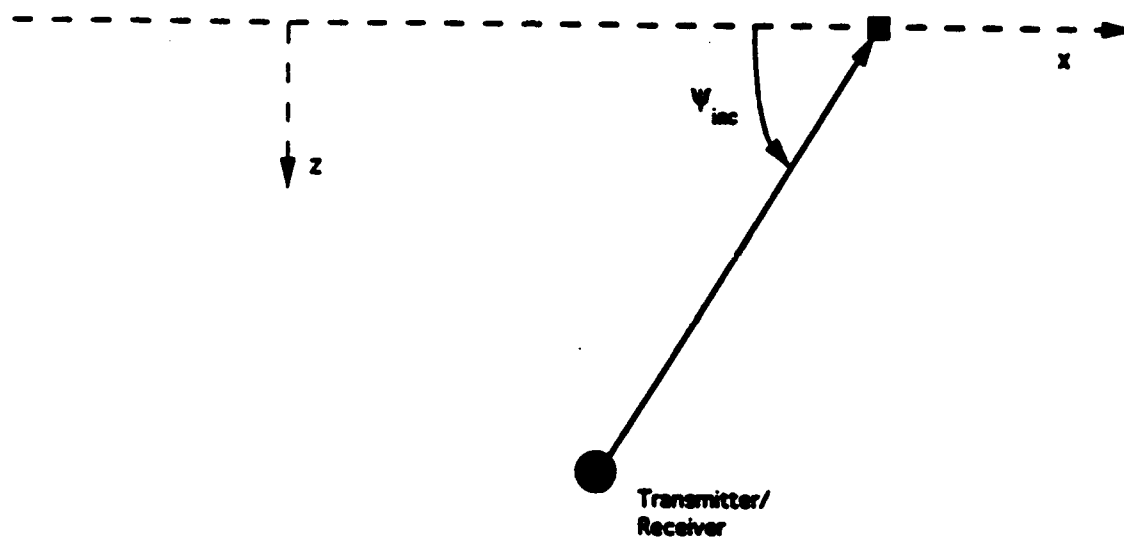
Figure A.2: Side View of Monostatic Geometry.

the incident grazing angle, ψ_{inc}.

In the case of a bistatic sonar geometry, the source and the receiver are located at two different locations. When a pulse is transmitted by the source, a delay equal to the length of time for the pulse to propagate from the source to the receiver occurs before the pulse is received at the receiver. Arrival of the pulse at the receiver via a direct path, without any boundary interactions, is called the direct blast in the vernacular of bistatic geometries [11]. After the direct blast ends, only returns from scattering due to inhomogeneities, boundaries and scatterers located in the ensonified area are received. The ensonified area is no longer a spherical shell, but is now an ellipsoidal shell.

When the ensonified volume interacts with a boundary, the resulting ensonified area is an elliptical annulus. An example of the ensonified area on a surface is shown in Figure A.3 looking down on the surface. Three geometrical parameters are needed to a describe bistatic geometry, as shown in Figures A.4 and A.5. The bistatic angle, $\phi_{bistatic}$, is defined to be zero in the forward scattered direction. The incident grazing angle, ψ_{inc}, and the scattered grazing angle, ψ_{scat}, are in general not equal, as shown in Figure A.5.
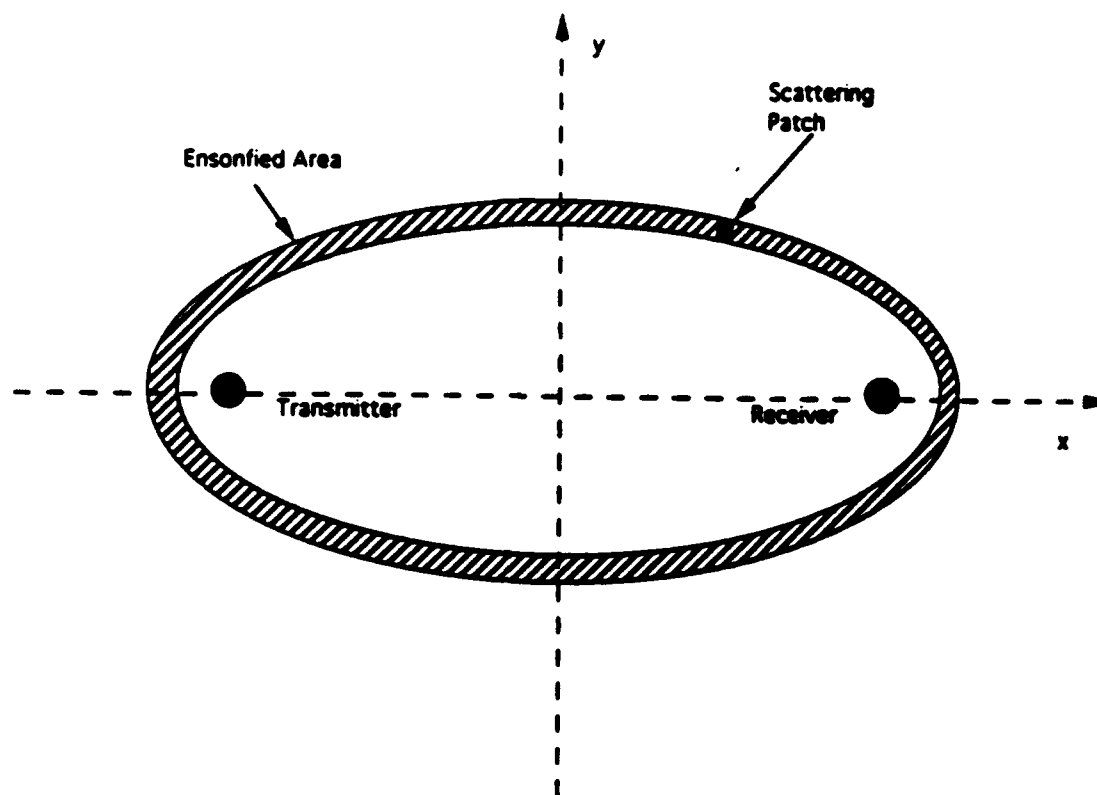
Figure A.3: Overhead View of Bistatic Geometry.
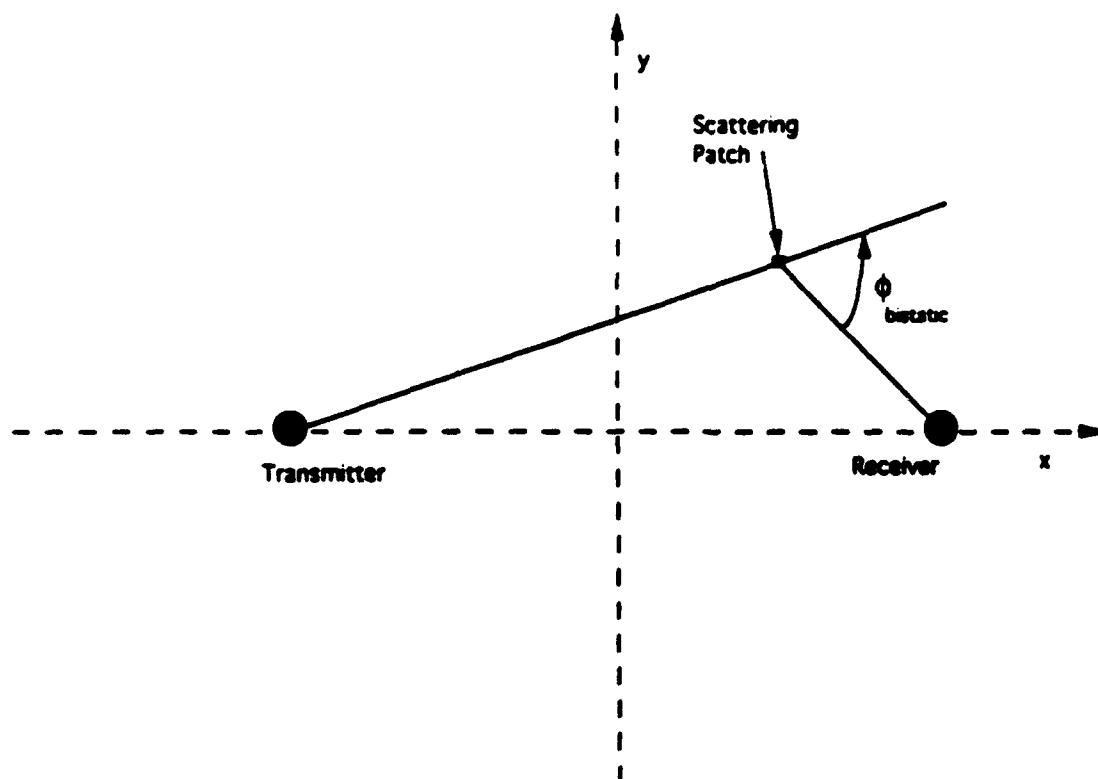
Figure A.4: Definition of Bistatic Angle from Top View.
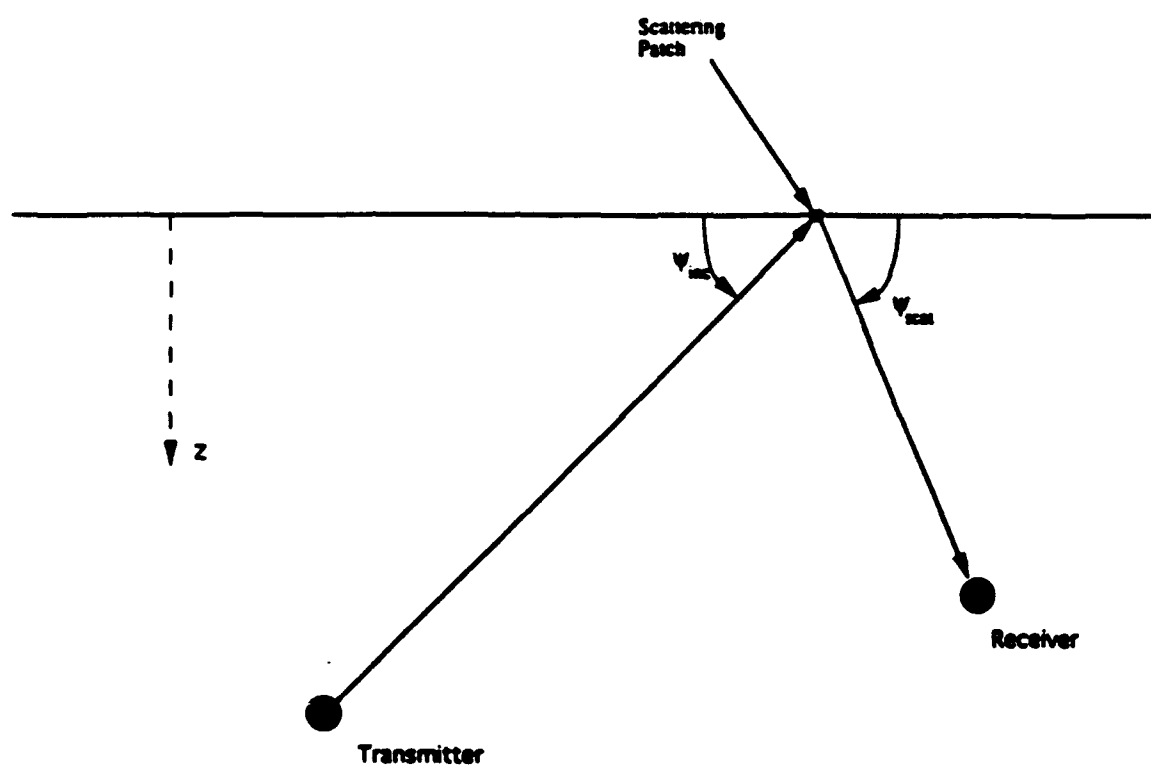
Figure A.5: Side View of Bistatic Geometry.

Appendix B

Code to Reduce Data to Scattering Strength

B.1 Usage of Code

The code included in this appendix was used to reduce the bistatic sur-face scatter data collected from the FLIP experiment an produce estimates of the bistatic surface scattering strength.

The code requires the user to input a number of values unique to the ge-ometry and operating parameters at which the data were collected. In addition, input files are required for the mean magnitude of the complex envelope and any directional beam patterns used. The user is prompted for input from the keyboard. The output consists of two files, both in ascii format, the names of which are chosen by the user. One file contains the estimate of bistatic surface scattering strength as a function of the three geometrical parameters, ψ_{inc}, ψ_{scat} and ϕ, and time. The second file contains the position of the center of the scattering patch as a function of time.

B.2 Listing of Code

This is a listing of the program used to convert the data from an estimate of the received level in dB into an estimate of the bistatic surface scattering strength.

```
1            program vers3
2 C
3 C       Program to compute the bistatic surface scattering strength for the
4 C       FLIP data.  This version allows for both transmitter and receiver
5 C       beam patterns (table driven) with arbitrary point direction, except
6 C       for roll.
7 C
8 C       Variables used in program:
9 C
10 C      Environmental Information:
11 C
12 C       c                :      sound speed (isovelocity in m/s)
13 C       attn             :      attenuation coefficient (function of freq.)
14 C                                  in dB/m.
15 C
16 C      Geometry and Pulse Information:
17 C
18 C       trlevel          :      transmitted level (dB)
19 C       duration         :      pulse length entered in msec converted
20 C                                  to sec
21 C       f                :      value to convert between seconds and msec
22 C       separation       :      horizontal distance between the source
23 C                                  and the receiver (m)
24 C
25 C      Transmit Beam Information:
26 C
27 C       tr_beam          :      flag for transmit beam ( 1 = omni, 2 = table)
28 C       file_tr          :      file containing the transmit beam pattern
29 C       beam_tr(32761)   :      transmit beam pattern stored in array
30 C       orientation_tr   :      angle of MRA for the transmitter with respect
31 C                                  to line drawn between source and
32 C                                  receiver (CW is +)
33 C       elev_fix_tr      :      angle of elevation of MRA for
34 C                                  transmitter (up is +)
35 C
36 C      Receive Beam Information:
37 C
38 C       rec_beam         :      flag for receive beam ( 1 = omni, 2 = table)
39 C       file_rec         :      file containing the receive beam pattern
40 C       beam_rec(32761)  :      receive beam pattern stored in array
41 C       orientation_rec  :      angle of MRA for the receiverer with respect
42 C                                  to line drawn between source and
43 C                                  receiver (CW is +)
44 C       elev_fix_rec     :      angle of elevation of MRA for receiver (up is +)
45 C
46 C      Envelope Information:
47 C
48 C       file_env         :      file containing the envelope
49 C       reclevel(1000)   :      envelope level of real data sampled at 1msec
50 C
51 C      Output File Information:
52 C
53 C       file_out         :      file containing the peak points for
54 C                                  each time slice
55 C       file_as          :      file containing the scattering strength and the
56 C                                  angles for each time slice
57 C
58 C      Search Information:
59 C
60 C       start            :      start time for calculation of ellipse
61 C       end              :      end time for calculation of ellipse
62 C       interval         :      interval at which calculations are
63 C                                  to be done
64 C       mesh_original    :      original mesh size input by user
65 C       mesh             :      size of step taken in search for points
66 C                                  between the two ellipses on the surface
67 C                                  in the x-direction
68 C       mesh_y           :      size of step taken in search for points
69 C                                  between the two ellipses on the surface
70 C                                  in the y-direction
```

```
71  C      dist_2_surf    :     distance from source to surface point
72  C      dist_2_rec     :     distance from surface point to receiver
73  C      dist           :     sum of dist_2_surf and dist_2_rec
74  C      time           :     time at which the calculation is being done
75  C      round_trip_outer:    total travel distance to the beginning
76  C                              of the pulse
77  C      round_trip_inner:    total travel distance to the end of the pulse
78  C
79  C      Coordinates in un-translated, un-rotated cartesian coordinates
80  C
81  C      source_x       :     x location of source
82  C      source_y       :     y location of source
83  C      source_z       :     z location of source (down is +)
84  C      receiver_x     :     x location of receiver
85  C      receiver_y     :     y location of receiver
86  C      receiver_z     :     z location of receiver (down is +)
87  C      delta_a(100000) :    horizontal distance from source to receiver
88  C      delta_b(100000) :    horizontal distance from source to ellipse pt.
89  C      delta_c(100000) :    horizontal distance from receiver to ellipse pt.
90  C      ellipse_x(100000):   ellipse x-coord.
91  C      ellipse_y(100000):   ellipse y-coord.
92  C
93  C      Coordiantes translated and rotated for source orientation
94  C
95  C      source_x_tr    :     x location of source (separation)
96  C      source_y_tr    :     y location of source (0.0)
97  C      receiver_x_tr  :     x location of receiver (0.0)
98  C      receiver_y_tr  :     y location of receiver (0.0)
99  C      delta_a(100000) :    horizontal distance from source to receiver
100 C      delta_b(100000) :    horizontal distance from source to ellipse pt.
101 C      delta_c(100000) :    horizontal distance from receiver to ellipse pt.
102 C      brng_tr(100000) :    bearing angle from source to ellipse pt.
103 C                              relative to MRA of source
104 C      elev_tr(100000) :    elevation angle from source to ellipse pt.
105 C                              relative to MRA of source
106 C      ellipse_x_tr(100000): ellipse x-coord. referenced to source
107 C      ellipse_y_tr(100000): ellipse y-coord. referenced to source
108 C      ellipse_z_tr(100000): ellipse z-coord. referenced to source
109 C
110 C      Coordiantes translated and rotated for receiver orientation
111 C
112 C      source_x_rec   :     x location of source (0.0)
113 C      source_y_rec   :     y location of source (0.0)
114 C      receiver_x_rec :     x location of receiver (-1*separation)
115 C      receiver_y_rec :     y location of receiver (0.0)
116 C      delta_a(100000) :    horizontal distance from source to receiver
117 C      delta_b(100000) :    horizontal distance from source to ellipse pt.
118 C      delta_c(100000) :    horizontal distance from receiver to ellipse pt.
119 C      brng_rec(100000):    bearing angle from receiver to ellipse pt.
120 C                              relative to MRA of receiver
121 C      elev_rec(100000):    elevation angle from receiver to ellipse pt.
122 C                              relative to MRA of receiver
123 C      ellipse_x_rec(100000): ellipse x-coord. referenced to receiver
124 C      ellipse_y_rec(100000): ellipse y-coord. referenced to receiver
125 C      ellipse_z_rec(100000): ellipse z-coord. referenced to receiver
126 C
127 C      Search for Maximum Information:
128 C
129 C      pointer        :     pointer for location in transmit beam pattern
130 C      pointer_rec    :     pointer for location in receive beam pattern
131 C      max            :     test variable used to find maximum in
132 C                              the sum of the transmission losses,
133 C                              beam patterns and attenuation loss
134 C      location       :     location of the point max in the array of points
135 C                              between the two ellipses
136 C      test(100000)   :     values corresponding to the sum of the
137 C                              transmission losses, beam patterns and
138 C                              the attenuation loss for each point
```

```
139 C
140 C         Calculation of Area Information:
141 C
142 C         area            :       area of ensonofied patch in m**2 once the
143 C                                 area converges to a values (+/- 10% of
144 C                                 area with coarser mesh size)
145 C         area_fine       :       area with coarser mesh size
146 C         area_finer      :       area with smaller mesh size
147 C         flag            :       flag used in looping to finer mesh size
148 C
149 C         Results Information:
150 C
151 C         bist_angle      :       bistatic angle (deg)
152 C         theta_naught    :       incident angle from source to ensonofied patch
153 C                                 on the surface
154 C         theta           :       scattered angle from ensonofied patch on the
155 C                                 surface to the receiver
156 C         scat_str        :       value of scattering strength
157 C
158           implicit real*8 (a-h, k, o-z)
159           dimension reclevel(1000), ellipse_x(100000), ellipse_y(100000)
160           dimension ellipse_x_rec(100000), ellipse_y_rec(100000)
161           dimension ellipse_z_rec(100000), ellipse_x_tr(100000)
162           dimension ellipse_y_tr(100000), ellipse_z_tr(100000)
163           dimension brng_tr(100000), elev_tr(100000)
164           dimension brng_rec(100000), elev_rec(100000)
165           dimension beam_tr(32761), beam_rec(32761)
166           dimension delta_a(100000), delta_b(100000), delta_c(100000)
167           dimension test(100000)
168           real*8 max, mesh, mesh_y, x, y, mesh_original
169           integer counter, start, end, interval, flag
170           real orientation_tr, elev_fix_tr
171           real orientation_rec, elev_fix_rec
172           integer tr_beam, rec_beam
173           integer pointer, pointer_rec
174           integer position_tr, position_rec
175           integer begin, length
176           character*20 file_tr, file_rec, file_env, file_out, file_ss
177 C
178 C         Pre-defined values used in program:
179 C         Sound Speed:    c (m/s)
180                           c = 1500.0
181 C         Sample Rate:    f (Hz)
182                           f = 1000.0
183 C         Conversion from radians to degrees:     rad (deg/rad)
184                           rad = 57.2958
185 C         Pi, of course: pi
186                           pi = 3.141592654
187 C
188 C         Asks for inputs for the run.
189 C
190           write(*,*) 'Enter the transmitted level in dB.'
191           read(*,*) trlevel
192 C
193           write(*,*) 'Enter the pulse duration in msec.'
194           read(*,*) duration
195           duration = duration/1000.0
196 C
197           write(*,*) 'Enter the atteuation coefficient (dB/m).'
198           read(*,*) attn
199 C
200           write(*,*) 'Enter the begin time for envelope data in msec.'
201           read(*,*) begin
202 C
203           write(*,*) 'Enter the sample time for envelope data in msec.'
204           read(*,*) length
205 C
206           write(*,*) 'Enter the start time, end time, and interval
207         1 for the run in msec.'
```

```
208          read(*,*) start, end, interval
209 C
210          write(*,*) 'Enter the mesh size for the surface search in meters.'
211          read(*,*) mesh
212          mesh_original = mesh
213 C
214          write(*,*) 'Enter the source-receiver separation.'
215          read(*,*) separation
216 C
217 C        Place the source and receiver on the x-axis symmetrical with each other
218 C
219          source_x = -1*separation/2.0
220          receiver_x = separation/2.0
221          source_y = 0.0
222          receiver_y = 0.0
223 C
224          write(*,*) 'Enter the source depth and receiver depth.'
225          read(*,*) source_z, receiver_z
226 C
227 C        write(*,400)
228   400    format ( 'Enter transmit beam pattern type:',
229        1     ' 1 = omni beam pattern           ',
230        2     ' 2 = table of beam pattern')
231 C        read(*,*) tr_beam
232 C
233 C        Hardwire for now the value of tr_beam equal to 1.
234 C
235          tr_beam = 1
236 C
237          if (tr_beam .ne. 1) then
238          write(*,*) 'Enter the name of the file which holds
239        1 the transmit beam pattern.'
240          read(*,*) file_tr
241 C
242          write(*,*) 'Enter the angle for the orientation of the transmitter
243        1 (+ is CW from a line from the source to the receiver).'
244          read(*,*)  orientation_tr
245 C
246          orientation_tr = orientation_tr/rad
247 C
248          write(*,*) 'Enter the elevation of the transmitter (+ is up).'
249          read(*,*) elev_fix_tr
250 C
251          elev_fix_tr = elev_fix_tr/rad
252 C
253          endif
254 C
255          write(*,500)
256   500    format ( 'Enter receive beam pattern type:',
257        1     ' 1 = omni beam pattern           ',
258        2     ' 2 = table of beam pattern')
259          read(*,*) rec_beam
260 C
261          if (rec_beam .ne. 1) then
262          write(*,*) 'Enter the name of the file which holds
263        1 the receive beam pattern.'
264          read(*,*) file_rec
265 C
266          write(*,*) 'Enter the angle for the orientation of the receiver
267        1 (+ is CW from a line from the receiver to the source).'
268          read(*,*)  orientation_rec
269 C
270          orientation_rec = orientation_rec/rad
271 C
272          write(*,*) 'Enter the elevation of the receiver (+ is up).'
273          read(*,*) elev_fix_rec
274 C
275          elev_fix_rec = elev_fix_rec/rad
276 C
```

```
277          endif
278
279          write(*,*) 'Enter the name of the file which holds the envelope.'
280          read(*,*) file_env
281 C
282          write(*,*) 'Enter the name of the file which will hold the output.'
283          read(*,*) file_out
284 C
285          write(*,*) 'Enter the name of the file which will hold the
286        1 scattering strength.'
287          read(*,*) file_ss
288 C
289          open (5, file = file_env)
290          open (6, file = file_out)
291          open (7, file = file_ss)
292 C
293 C        Reads in beam patterns (if necessary):
294 C
295          if (tr_beam .ne. 1) then
296          open (4, file = file_tr)
297          do 2 i=0,6551
298                 read(4,*) beam_tr(5*i+1), beam_tr(5*i+2), beam_tr(5*i+3),
299        1 beam_tr(5*i+4), beam_tr(5*i+5)
300    2     continue
301 C
302          read(4,*) beam_tr(32761)
303 C
304 C        if flag tr_beam = 1 then give an omnidirectional beam pattern
305 C
306          else
307          do 5 i=1,32761
308                 beam_tr(i) = 0.0
309    5     continue
310 C
311          orientation_tr = 0.0
312          elev_fix_tr = 0.0
313 C
314          endif
315 C
316          if (rec_beam .ne. 1) then
317          open (3, file = file_rec)
318          do 8 i=0,6551
319                 read(3,*) beam_rec(5*i+1), beam_rec(5*i+2), beam_rec(5*i+3),
320        1 beam_rec(5*i+4), beam_rec(5*i+5)
321    8     continue
322 C
323          read(3,*) beam_rec(32761)
324 C
325 C        if flag rec_beam = 1 then give an omnidirectional beam pattern
326 C
327          else
328          do 7 i=1,32761
329                 beam_rec(i) = 0.0
330    7     continue
331 C
332          orientation_rec = 0
333          elev_fix_rec = 0
334 C
335          endif
336 C
337 C        Reads in the envelope level from the data:
338 C
339          do 10 i=0,((length/5) - 1)
340            read(5,*) reclevel(5*i+1), reclevel(5*i+2), reclevel(5*i+3),
341        1            reclevel(5*i+4), reclevel(5*i+5)
342   10     continue
343 C
344          write(6,*) source_x, source_y
345          write(6,*) receiver_x, receiver_y
346 C
```

```
347            write(7,*) 'Time (sec) Bist. (deg)  Inc. (deg)  Scat. (deg)
348    1 Bist. SS (dB)'
349  C
350  C        Finds the ellipse on the surface for a particular time (time).
351  C
352            do 20 i= start, end, interval
353  C
354              counter = 0
355              area_fine = 0.0
356              area_finer = 0.0
357              mesh = mesh_original
358              flag = 0
359  C
360    30       if (flag .eq. 0) then
361  C
362  C        Set search parameters
363  C
364              time = i/f
365              round_trip_outer = i*c/f
366              round_trip_inner = (i - (duration*1000))*c/f
367              search_low = round_trip_outer*-0.51 - separation/2.0
368              search_high = round_trip_outer*0.51 + separation/2.0
369              search_y_low = round_trip_outer*-0.51
370              search_y_high = round_trip_outer*0.51
371              mesh_y = mesh
372  C
373            else
374  C
375  C        Set search parameters to around the high pt.
376  C
377              search_low = ellipse_x(location) - (separation/6.0)
378              search_high = ellipse_x(location) + (separation/6.0)
379              search_y_low = ellipse_y(location) - (separation/6.0)
380              search_y_high = ellipse_y(location) + (separation/6.0)
381              mesh_y = mesh
382  C
383            endif
384  C
385  C        Search along x for y values between the two ellipses
386  C
387              do 100 x= search_low, search_high, mesh
388                do 110 y= search_y_low, search_y_high, mesh_y
389                  dist_2_surf = dsqrt((x - source_x)**2 + (y - source_y)**2 +
390    1                        (source_z)**2)
391                  dist_2_rec = dsqrt((x - receiver_x)**2 +(y - receiver_y)**2 +
392    1                        (receiver_z)**2)
393                  dist = dist_2_surf + dist_2_rec
394                  if (dist.lt.round_trip_outer.and.dist.gt.round_trip_inner)then
395                    counter = counter + 1
396                    ellipse_x(counter) = x
397                    ellipse_y(counter) = y
398                  endif
399            if (counter .gt. 99999) goto 999
400    110         continue
401    100       continue
402  C
403  C        Calculates the bearing and elevation between the source
404  C        and the ellipse pts.
405  C
406              do 130 j=1,counter
407  C
408  C        At this point, make a change in coordinates so that the MRA of the
409  C        transmitter is pointing along the pos. z-axis and the transmitter
410  C        is located at the origin (0,0,0).
411  C
412            ellipse_x_tr(j) = ((ellipse_x(j) + separation/2.0)*
413    1      cos(orientation_tr)
414    1      - (ellipse_y(j)*sin(orientation_tr)))
415    1      *cos(elev_fix_tr) + (source_z)*sin(elev_fix_tr)
```

```
416 C
417            ellipse_y_tr(j) = (ellipse_x(j) + separation/2.0)*sin(orientation_tr)
418        1    + (ellipse_y(j)*cos(orientation_tr))
419 C
420            ellipse_z_tr(j) = ((ellipse_x(j) + separation/2.0)*
421        1    cos(orientation_tr)
422        1    - (ellipse_y(j)*sin(orientation_tr)))
423        1    *sin(elev_fix_tr) - (source_z)*cos(elev_fix_tr)
424 C
425 C      Make changes to the delta's to relfect the coordinate change
426 C
427            source_x_tr = 0.0
428            source_y_tr = 0.0
429 C
430            receiver_x_tr = separation
431            receiver_y_tr = 0.0
432 C
433                delta_a(j) = (source_x_tr - receiver_x_tr)**2
434                delta_a(j) = delta_a(j) + (source_y_tr - receiver_y_tr)**2
435                delta_a(j) = dsqrt(delta_a(j))
436                delta_b(j) = (source_x_tr - ellipse_x_tr(j))**2
437                delta_b(j) = delta_b(j) + (source_y_tr - ellipse_y_tr(j))**2
438                delta_b(j) = dsqrt(delta_b(j))
439                delta_c(j) = (receiver_x_tr - ellipse_x_tr(j))**2
440                delta_c(j) = delta_c(j) + (receiver_y_tr - ellipse_y_tr(j))**2
441                delta_c(j) = dsqrt(delta_c(j))
442 C
443                brng_tr(j) = (delta_c(j))**2 - ((delta_a(j))**2 + (delta_b(j))**2)
444                brng_tr(j) = brng_tr(j)/(-2.0*delta_a(j)*delta_b(j))
445                brng_tr(j) = acos(brng_tr(j))*rad
446 C
447                if(ellipse_y_tr(j) .gt. 0.0) then
448                   brng_tr(j) = -1*brng_tr(j)
449                endif
450 C
451                brng_tr(j) = ifix(brng_tr(j))
452 C
453                elev_tr(j) = datan2(source_z,delta_b(j))*rad
454                elev_tr(j) = ifix(elev_tr(j))
455                elev_tr(j) = -1*elev_tr(j)
456 C
457 C      At this point, make a change in coordinates so that the MRA of the
458 C      received array is pointing along the neg. x-axis and the array is
459 C      located at the origin (0,0,0)
460 C
461            ellipse_x_rec(j) = ((ellipse_x(j) - separation/2.0)*
462        1    cos(orientation_rec)
463        1    - (ellipse_y(j)*sin(orientation_rec)))
464        1    *cos(elev_fix_rec) - (receiver_z)*sin(elev_fix_rec)
465 C
466            ellipse_y_rec(j) = (ellipse_x(j) - separation/2.0)*sin(orientation_rec)
467        1    + (ellipse_y(j)*cos(orientation_rec))
468 C
469            ellipse_z_rec(j) = -1*((ellipse_x(j) - separation/2.0)*
470        1    cos(orientation_rec)
471        1    - (ellipse_y(j)*sin(orientation_rec)))
472        1    *sin(elev_fix_rec) - (receiver_z)*cos(elev_fix_rec)
473 C
474 C      Make changes to the delta's to reflect the coordinate change
475 C
476            source_x_rec = -1*separation
477            source_y_rec = 0.0
478 C
479            receiver_x_rec = 0.0
480            receiver_y_rec = 0.0
481 C
482
483                delta_a(j) = (source_x_rec - receiver_x_rec)**2
```

```
484                    delta_a(j) = delta_a(j) + (source_y_rec - receiver_y_rec)**2
485                    delta_a(j) = dsqrt(delta_a(j))
486                    delta_b(j) = (source_x_rec - ellipse_x_rec(j))**2
487                    delta_b(j) = delta_b(j) + (source_y_rec - ellipse_y_rec(j))**2
488                    delta_b(j) = dsqrt(delta_b(j))
489                    delta_c(j) = (receiver_x_rec - ellipse_x_rec(j))**2
490                    delta_c(j) = delta_c(j) + (receiver_y_rec - ellipse_y_rec(j))**2
491                    delta_c(j) = dsqrt(delta_c(j))
492 C
493                    brng_rec(j) = (delta_b(j))**2 - ((delta_a(j))**2 + (delta_c(j))**2)
494                    brng_rec(j) = brng_rec(j)/(-2.0*delta_a(j)*delta_c(j))
495                    brng_rec(j) = acos(brng_rec(j))*rad
496 C
497                    if(ellipse_y_rec(j) .lt. 0.0) then
498                      brng_rec(j) = -1*brng_rec(j)
499                    endif
500 C
501                    brng_rec(j) = ifix(brng_rec(j))
502 C
503                    elev_rec(j) = datan2(ellipse_z_rec(j),delta_c(j))*rad
504                    elev_rec(j) = ifix(elev_rec(j))
505                    elev_rec(j) = -1*elev_rec(j)
506 C
507   130      continue
508 C
509 C        Reset max each time through the loop.
510 C
511            max = -1000.0
512 C
513 C        Search through the points on the ellipse for the lowest loss ( the
514 C        sum of the transmission losses and the beam gains).
515 C
516            do 135 j=1,counter
517 C
518                if(brng_tr(j).gt.90 .or. brng_tr(j).lt.-90
519       1 .or. brng_rec(j).gt.90 .or. brng_rec(j).lt.-90) then
520                    test(j) = -1000.0
521                    go to 135
522                endif
523 C
524                pointer = (brng_tr(j)+90)*181
525                pointer = pointer + elev_tr(j) + 91
526 C
527                pointer_rec = (brng_rec(j)+90)*181
528                pointer_rec = pointer_rec + elev_rec(j) +91
529 C
530                test(j) = beam_tr(pointer)
531                test(j) = test(j) + beam_rec(pointer_rec)
532                test(j) = test(j) - 10*dlog10(delta_b(j)**2 + (source_z)**2)
533                test(j) = test(j) - 10*dlog10(delta_c(j)**2 + (receiver_z)**2)
534                test(j) = test(j) - attn*dsqrt(delta_b(j)**2 + (source_z)**2)
535                test(j) = test(j) - attn*dsqrt(delta_c(j)**2 + (receiver_z)**2)
536 C
537                if (test(j).gt.max) then
538                    location = j
539                    max = test(j)
540                    bearing_hit = brng_tr(j)
541                    elevation_hit = elev_tr(j)
542                    position_tr = pointer
543                    position_rec = pointer_rec
544                endif
545 C
546   135      continue
547 C
548 C        Check to see if flag is zero, if so, set equal to 1, calculate
549 C        the area and drop the mesh size.  If flag is nonzero, calculate
550 C        the area and compare with coarser mesh size area.
551 C
```

```
552            if (flag .eq. 0) then
553                flag = 1
554   C
555   C       Count all points on the surface that are within 3 dB of
556   C       max and calculate the area.
557   C
558                do 180 j = 1, counter
559                    if ((max - 3.0) .lt. test(j)) then
560                        area_fine = area_fine + (mesh)**2
561                    endif
562   180          continue
563   C
564                mesh = mesh/2.0
565                counter = 0
566                goto 30
567   C
568            else
569   C
570   C       Count all points on the surface that are within 3 dB of
571   C       max and calculate the area.
572   C
573                do 200 j = 1, counter
574                    if ((max - 3.0) .lt. test(j)) then
575                        area_finer = area_finer + (mesh)**2
576                    endif
577   200          continue
578   C
579   C       After the area has been calculated, compare with the area calculated
580   C       with the prior mesh size (pass if within +/- 10%).  This means that
581   C       the first acceptable area can be at mesh_original/2.0.  If the areas
582   C       are not within the given tolerance, drop the mesh size by a factor of
583   C       two and do it again.
584   C
585            if (area_finer*1.25.gt.area_fine.and.area_finer*0.8.lt.area_fine)then
586                area = area_finer
587                goto 220
588            else
589                area_fine = area_finer
590                area_finer = 0.0
591                mesh = mesh/2.0
592                counter = 0
593                goto 30
594            endif
595   C
596            endif
597   C
598   C       Calculate the bistatic surface scattering strength and write it.
599   C
600   220    scat_str = reclevel(i-begin) -test(location) -trlevel -10*dlog10(area)
601   C
602   C       Calculate all the angles and write them out.
603   C
604            delta_a(location) = (source_x - receiver_x)**2
605            delta_a(location) = delta_a(location) + (source_y - receiver_y)**2
606            delta_a(location) = dsqrt(delta_a(location))
607            delta_b(location) = (source_x - ellipse_x(location))**2
608            delta_b(location) = delta_b(location) +
609       1 (source_y - ellipse_y(location))**2
610            delta_b(location) = dsqrt(delta_b(location))
611            delta_c(location) = (receiver_x - ellipse_x(location))**2
612            delta_c(location) = delta_c(location) +
613       1 (receiver_y - ellipse_y(location))**2
614            delta_c(location) = dsqrt(delta_c(location))
615   C
616            bist_angle = (delta_a(location))**2
617            bist_angle = bist_angle - ((delta_b(location))**2
618       1              + (delta_c(location))**2)
619            bist_angle = bist_angle/(-2.0*delta_b(location)*delta_c(location))
620            bist_angle = acos(bist_angle)*rad
```

```
621            bist_angle = 180.0 - dabs(bist_angle)
622 C
623            theta_naught = datan2(source_z,delta_b(location))*rad
624 C
625            theta = datan2(receiver_z,delta_c(location))*rad
626 C
627            write(7,260) time, bist_angle, theta_naught, theta, scat_str
628   260      format(f6.3,4x,1f6.1,6x,1f6.1,7x,1f6.1,7x,f6.1)
629 C
630            write(6,*) ellipse_x(location), ellipse_y(location), time
631 C
632            goto 20
633 C
634   999      write(7,*) 'At stop. Counter = ', counter
635 C
636    20      continue
637 C
638            stop
639            end
```

References

[1] J. G. Zornig, "Bistatic Surface Scattering Strength Measured at Short Wavelengths," Journal of the Acoustical Society of America, Vol. 63, pp. 758-767 (1978).

[2] W. A. Kinney and J. G. Zornig, "The Azimuthal Dependence of Bistatic Surface Scattering: A Comparison Between Theory and Experiment," Journal of the Acoustical Society of America, Vol. 77, pp. 1403-1408 (1985).

[3] R. L. Culver and S. T. McDaniel, "Bistatic Ocean Surface Reverberation Simulation," IEEE Proc. ICASSP 91, pp. 1453-1456, Toronto, Canada, (1991).

[4] R. J. Urick and R. M. Hoover, "Backscattering of Sound from the Sea Surface: Its Measurement, Causes and Application to the Prediction of Reverberation Levels," Journal of the Acoustical Society of America, Vol. 28, pp. 1038-1042 (1956).

[5] G. R. Garrison, S. R. Murphy and D. S. Potter, "Measurements of the Backscattering of Underwater Sound from the Sea Surface," Journal of the Acoustical Society of America, Vol. 32, pp. 104-111 (1960).

[6] R. P. Chapman and J. H. Harris, "Surface Backscattering Strengths Measure with Explosive Sound Sources," Journal of the Acoustical Society of America, Vol. 34, pp. 1592-1597 (1962).

[7] T. D. Plemmons, J. A. Shooter and D. Middleton, "Underwater Acoustic Scattering from Lake Surfaces. I. Theory, Experiment, and Validation of the Data," Journal of the Acoustical Society of America, Vol. 52, pp. 1488-1502 (1972).

[8] M. E. Frazer, "Some Statistical Properties of Lake Surface Reverberation," Journal of the Acoustical Society of America, Vol. 64, pp. 858-868 (1978).

[9] S. Siegel, Nonparametric Statistics for the Behavioral Sciences (McGraw-Hill Book Company, Inc., New York, 1956).

[10] W. S. Burdic, Underwater Acoustic System Analysis (Prentice Hall, Englewood Cliffs, 1991).

[11] H. Cox, "Fundamentals of Bistatic Active Sonar," in Underwater Acoustic Data Processing, edited by Y. T. Chan (Kluwer Academic Publishers, Boston, 1989), pp. 3-24.

[12] S. T. McDaniel and A. D. Gorman, "An Examination of the Composite-Roughness Scattering Model," Journal of the Acoustical Society of America, Vol. 73, pp. 1476-1486 (1983).

[13] S. T. McDaniel, "Diffractive corrections to the high-frequency Kirchhoff Approximation," Journal of the Acoustical Society of America, Vol. 79, pp. 952-957 (1986).

[14] S. T. McDaniel, "Acoustical Estimates of Subsurface Bubble Densities in the Open Ocean and Coastal Waters," in Sea Surface Sound: Natural Mechanisms of Surface Generated Noise in the Ocean. edited by B. R. Kerman (Kluwer Academic Publishers, Boston, 1988), pp. 225-236.

[15] S. T. McDaniel, "Models for Predicting Bistatic Surface Scattering Strength," ARL-PSU TM 90-88, 30 March 1990.

[16] P. H. Dahl, Personal Correspondence to Dr. Lee Culver, February 1992.

[17] R. L. Culver, Personal Correspondence to Dr. Peter Dahl. December 1991.

[18] P. H. Dahl, Personal Correspondence to Dr. Lee Culver, October 1991.

[19] F. H. Fisher and F. N. Spiess, "Flip-Floating Instrument Platform." Journal of the Acoustical Society of America, Vol. 35, pp. 1633-1644 (1963).

[20] H. Boehme, N. P. Chotiros, L. D. Rolleigh, S. P. Pitt, A. L. Garcia, T. G. Goldsberry, and R. A. Lamb, "Acoustic Backscattering at low grazing angles from the ocean bottom. Part II. Statistical characteristics of bottom backscatter at a shallow water site," Journal of the Acoustical Society of America, Vol. 77, pp. 975-982 (1985).

[21] M. A. Donelan, J. Hamilton, and W. W. Hui, "Directional Spectra of Wind Generated Waves," Phil, Trans. Royal Society London, A315, pp. 509-562 (1985).

[22] W. J. Pierson, "The Theory and Applications of Ocean Wave Measuring Systems at and Below the Sea Surface, On the Land, From Aircraft and From Space raft," NASA Contract. Re.p. CR-2646, NASA, Washington, DC, (1986).

[23] W. J. Pierson and R. A. Stacy, "The Elevation, Slope, and Curvature Spectrum of a Wind Roughened Sea Surface," NASA Contract. Rep. CR-2247, NASA, Washington, DC, (1973).